UNIVERSITY OF CAPE TOWN
IYUNIVESITHI YASEKAPA • UNIVERSITEIT VAN KAAPSTAD

Development and Preliminary Numerical Investigations of a Dislocation Density-Based, Finite-Strain, Rate-Dependent Elastoplasticity Constitutive Model

by

Author:
Emma Garschagen

Supervisors:
B.H. Alheit
E.B. Ismail

Dissertation presented in partial fulfillment of the Degree of
Master of Science in the Department of Mechanical Engineering
University of Cape Town

August 2024

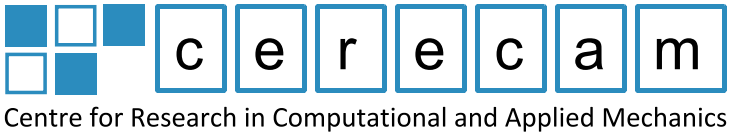

Declaration

I, Emma Garschagen, know the meaning of plagiarism and declare that all the work in the document, save for that which is properly acknowledged, is my own. This dissertation has been submitted to the Turnitin module and I confirm that my supervisor has seen my report and any concerns revealed by such have been resolved with my supervisor.

Signature: Signed by candidate Date: 31 August 2024

Abstract

Finite-strain elastoplasticity constitutive models suitable for process-scale simulation are typically developed from empirical observations of phenomena of interest. Such models make use of internal state variables that do not directly represent the associated evolution of the material microstructure, such as accumulated plastic strain. As a result, these models cannot directly provide microstructural information that may be of interest. In an attempt to bridge this gap, a mechanistically-motivated, multiaxial, finite-strain, rate-dependent elastoplasticity constitutive model in which average dislocation density is used as an internal state variable is developed in this work.

The relationship between dislocation-based phenomena and work hardening in face-centred cubic metals is well-researched, and the popular Kocks-Mecking model for average dislocation density evolution has been successfully implemented in small-strain elastoplasticity constitutive models. However, in contrast to other dislocation-based rate-dependent elastoplasticity models, the model presented in this work is formulated in a multiaxial, finite-strain framework that is suitable for the macro-scale simulation of wrought metal production processes. Work hardening as a result of large deformation is modelled as a function of average dislocation density, which is described by the Kocks-Mecking and finite-strain Hariharan-Barlat models.

The behaviour of the model is elucidated after a material point-level numerical implementation and computational experiments with several test cases, such as plane strain compression, uniaxial compression, and cyclical loading. The model is fit to 5XXX series aluminium mechanical test data sourced from the literature, and it is shown that, from preliminary investigations, the work hardening behaviour and associated dislocation density evolution under the given loading conditions concurs with general trends seen in literature.

Acknowledgements

First and foremost, I would like to express my deepest gratitude to my supervisors, Ben Alheit and Ernesto Ismail. Ben, your patience, company, and generosity with your time have been exceptional. Ernesto, your kindness, understanding, and equal generosity have kept this project afloat when I was most sure that it would sink. That I have had such supportive supervisors that are willing to go the extra mile is beyond belief.

I would also like to extend my thanks to our industrial partner, Hulamin, for funding this project in part. Their support, along with the generosity of the Reino Stegen scholarship, made this work possible.

To my colleagues at CERECAM, in particular Jono Duggan and Vincent Punabantu, I will always think back on our laughter in the kitchen and the significant contribution we made to the financial well-being of the local pizza joint with great fondness. Your company has been invaluable, and it made this journey a delight.

I am also deeply indebted to the friends that became remarkably efficient editors — Jessica Garschagen, Tara Boulle, Nita Pallett, Simon Daubner, Ciara McNamara, Vincent Punabantu, Amy Gribble, and Maxwell Vos — who each contributed their technical skill, attention, and humour to this dissertation.

To my parents, who listened with great patience and enthusiasm to topics well outside their interests, and provided an unwavering foundation throughout this journey. My gratitude to you is immeasurable.

A heartfelt thank you to my friends who provided passionate words of encouragement and cheered me on while listening to the weekly debrief over beers.

Finally, my most sincere and profound thanks go to Nita Pallett. Your support at every step of this journey has been nothing short of extraordinary.

Thank you all.

Table of Contents

List of Figures

List of Tables

A Glossary of Conventions and Notations

Conventions

Domains	lightface script, e.g. $\mathcal{B}$
Scalars	lightface italic, e.g. a, ρ
Vectors	boldface lowercase, e.g. $\boldsymbol{u}, \boldsymbol{x}$ including the exception of $\boldsymbol{X}$
Second-order tensors	boldface uppercase letters, e.g. $\boldsymbol{E}, \boldsymbol{F}$, excluding the vector $\boldsymbol{X}$
Fourth-order tensors	blackboard letters, e.g., $\mathbb{C}$
Material quantities	uppercase, e.g. $\boldsymbol{X}$
Spatial quantities	lowercase, e.g. $\boldsymbol{x}$
Constitutive response function	hat notation, e.g. $\hat{\Phi}(\varsigma)$ maps ς to field variable Φ

i^{th} component of a vector	lightface lowercase, e.g. u_i
ij^{th} component of a second-order tensor	lightface uppercase, e.g. E_{ij}
$ijkl^{th}$ component of a fourth-order tensor	blackboard letters, e.g. $\mathbb{C}_{ijkl}$

Braces $\{\bullet\}$	denote a set
Square parentheses $[\bullet]$	denote a coefficient, e.g. $f[a]$ denotes f multiplied by a
Rounded parentheses $(\bullet)$	denote arguments of a function, e.g. $f(a)$ denotes that f is a function of a

Notations

Mathematical Notation

$\boldsymbol{e}_1,\ \boldsymbol{e}_2,\ \boldsymbol{e}_3$	the orthonormal basis vectors
$\boldsymbol{e}_1^*,\ \boldsymbol{e}_2^*,\ \boldsymbol{e}_3^*$	the orthonormal basis vectors after undergoing a transformation, indicated by a superscript asterix

$\otimes$	the dyadic product operator
$\odot$	the dot product operator
$\mathbb{P}$	isochoric operator tensor
$\mathrm{skw}\,(\bullet)$, $\mathrm{sym}\,(\bullet)$	the skew and symmetric parts of a tensor, respectively

Kinematics

$\boldsymbol{X}$, $\boldsymbol{x}$	material and spatial points, respectively
$\mathcal{B}$, $\mathcal{B}_t$	material and spatial domains, respectively
$\mathcal{P}$, $\mathcal{P}_t$	material and spatial regions, respectively
ϕ	motion of a domain
$\mathrm{Grad}\,(\bullet)$, $\mathrm{grad}\,(\bullet)$	material and spatial gradient operators, respectively
$\mathrm{Div}\,(\bullet)$, $\mathrm{div}\,(\bullet)$	material and spatial divergence operators, respectively
$\boldsymbol{F}$	deformation gradient
$\boldsymbol{F}_p$, $\boldsymbol{F}_e$	plastic and elastic deformation gradients, respectively
$\boldsymbol{C}$, $\boldsymbol{B}$	right and left Cauchy-Green tensors, respectively
$\boldsymbol{H}$	displacement gradient
$\boldsymbol{E}$	Green-Lagrange strain
$\boldsymbol{\epsilon}$	infinitesimal strain
J	volumetric Jacobian
$\boldsymbol{u}$	displacement vector
$\dot{\boldsymbol{u}}$	velocity vector
$\ddot{\boldsymbol{u}}$	acceleration vector
$\boldsymbol{L}$	velocity gradient tensor
$\boldsymbol{L}_p$, $\boldsymbol{L}_e$	plastic and elastic velocity gradient tensors, respectively
$\boldsymbol{D}$	rate of deformation tensor
$\boldsymbol{D}_p$, $\boldsymbol{D}_e$	plastic and elastic rate of deformation tensors, respectively
$\|\bullet\|$	the Frobenius norm
$\|\bullet\|$	the absolute value

Stress Quantities

$\boldsymbol{\sigma}$	Cauchy stress
$\boldsymbol{\tau}$	Kirchhoff stress
$\boldsymbol{P}$	first Piola-Kirchhoff stress
$\boldsymbol{S}$	second Piola-Kirchhoff stress
$\boldsymbol{M}$	Mandel stress

Thermodynamics

$\mathcal{U}$	total internal energy
$\mathcal{K}$	total kinetic energy
$\mathcal{Q}$	total heat flux
$\mathcal{W}$	total external power
$\mathcal{F}$	total free energy
$\mathcal{S}$	total entropy
$\mathcal{T}$	total temperature
$\mathcal{J}$	total entropy flux
$U_{\text{int}},\ u_{\text{int}}$	internal energy per unit material and spatial volume, respectively
$N,\ \eta$	specific entropy per unit material and spatial volume, respectively
$\mathbf{Q}_{\text{R}},\ \mathbf{q}$	heat flux per unit material and spatial area, respectively
$\Theta,\ \vartheta$	material and spatial temperature fields, respectively
R, r	material and spatial heat supply, respectively
ρ_R, ρ_m	material and spatial heat supply, respectively
$\boldsymbol{j}$	entropy flux
j	entropy supply
$\Psi_R,\ \Psi$	material and spatial Helmholtz free energy symbols, respectively
r	heat supply
$\mathcal{D}$	dissipation

Constitutive Modelling

$\bar{\boldsymbol{A}}$	isochoric component of tensor $\boldsymbol{A}$
$\tilde{\boldsymbol{A}}$	volumetric component of tensor $\boldsymbol{A}$
$\boldsymbol{A}_e$	elastic component of tensor $\boldsymbol{A}$
$\boldsymbol{A}_p$	plastic component of tensor $\boldsymbol{A}$
$\mathbb{C}_e,\ \mathbb{c}_e$	the material and spatial elasticity tensors, respectively
$\mathbb{c}_{e\tau}$	a special tensor defined in Equation (C.15)
$\dot{\lambda}$	rate of plastic deformation
$\boldsymbol{N}$	effective plastic direction
$\boldsymbol{T}$	effective plastic direction in the spatial domain
τ_y	equivalent rate-independent yield stress
λ_L, μ	the Lamé parameters

Dislocation Density-Based Constitutive Modelling

τ_f	flow stress
T	absolute temperature in Kelvin
ρ	dislocation density
μ	shear modulus
Θ	rate of work hardening
M	Taylor factor
α	activation constant
b	magnitude of the Burgers vector
L	mean free path
k_1	material parameter related to dislocation storage (Kocks-Mecking model)
$\varphi,\ k$	material parameters related to dislocation storage (Hariharan-Barlat model)
k_2	material parameter related to dislocation annihilation

Chapter 1

Introduction

The finite-strain deformation of metallic materials is central to several manufacturing processes, such as the hot-rolling and sheet-forming processes that yield autobody components, beverage cans, and aluminium foil. The simulation of these large-deformation processes requires an elastoplasticity constitutive model. For such a model to be industrially relevant, the model should capture finite-strain, rate-dependent deformation and reflect the relationship between material behaviour and measurable, physical quantities.

This dissertation concerns the preliminary material point-level numerical implementation of a finite-strain, rate-dependent, elastoplasticity constitutive model that is informed by the predicted evolution of the average dislocation density in a face-centred cubic metal. Specifically, the thermodynamically-consistent extension of popular dislocation density evolution equations used in uniaxial, infinitesimal-strain settings to a multiaxial, finite-strain setting is demonstrated. This work is introduced in this chapter in two parts: first, the use of finite-strain theory is motivated, and, second, the use of dislocation density in plasticity models is introduced. An explanation of the structure of this dissertation follows in the subsequent section.

The purpose of the project presented in this dissertation can be formulated into the following research question:

Can traditional dislocation density-based models that were formulated for face-centred cubic metals in the infinitesimal-strain setting be extended to finite strains in a thermodynamically-consistent manner?

1.1 Finite-Strain Elastoplasticity Theory

Classical elastoplasticity theory based on the infinitesimal-strain approximation is often used for structural design where the onset of large plastic deformations is not considered. The infinitesimal-strain plasticity theory is predicated on the assumption that the total strain is given by the sum of its elastic and plastic components; this linear description of elastoplasticity, while simpler to implement numerically, does not describe the nonlinear

finite-strain regime well. Briefly, in finite-strain plasticity theory, the additive decomposition of strain is replaced by the multiplicative decomposition of the total deformation into elastic and plastic parts [1]. The nonlinearity of the finite-strain elastoplasticity theory better captures the material response at finite strains, and is therefore a more appropriate framework in which to set a constitutive model intended to capture mechanical behaviour during processing operations where large strains are present. A thorough mathematical description of this theory is reserved for Chapter 5.

Necessary to both small-strain and large-strain constitutive models that capture inelasticity are quantities that describe the mechanical history of the material. Plastic deformation is an irreversible process; therefore, the set of state variables must be expanded from temperature and deformation to include internal variables to provide a complete thermodynamic description of the process [2]. Several internal state variables may be used to predict the material response to attain a certain degree of accuracy, and the evolution of these internal state hardening variables may be described by phenomenological or microstructural mechanism-based models, which are reviewed in [3], [4]. In the typical case, accumulated plastic strain is used as the single internal state variable to describe work hardening behaviour. Accumulated plastic strain is introduced in Chapter 5, but it is sufficient to note that this concept lacks physical interpretability. Greater physical interpretability is provided by microstructural mechanism-based models which are informed by microstructure-property relations. While a plethora of internal state variables related to deformation mechanisms may be used to predict material response, it is necessary to contract the microstructural information to those mechanisms that dominate hardening processes for the model to remain computationally affordable and parsimonious. In this work, the set of internal state variables is restricted to one variable that describes the average dislocation density. The work presented in this dissertation was partially funded by Hulamin, a manufacturer of rolled aluminium products in South Africa. As aluminium is a face-centred cubic (FCC) metal, the models are developed for the FCC case. A review of dislocation theory fundamentals and work hardening in FCC metals is provided in Chapter 3.

1.2 Dislocation Density as an Internal State Variable

It has long been accepted that the evolution of dislocation density contributes to hardening behaviour [5]; therefore, it is fitting to describe the state of a material undergoing plastic deformation by its average dislocation density. Dislocation density-based constitutive models vary in complexity. Multi-parameter models [6]–[13] integrate phenomena occuring at different scales into a single plasticity model, often at great computational expense, while single-parameter models typically rely only on the evolution of dislocation

density to describe plastic behaviour [14], [15]. The Kocks-Mecking model [15]–[20] is a single-parameter model that provides an evolution equation for the average dislocation density as a function of the rate of plastic strain, which allows average dislocation density to be used as a scalar internal state variable within an internal state variable theory. The Kocks-Mecking model is common in infinitesimal-strain, elastoplasticity implementations [21]–[23]. Since Kocks', Mecking's and Estrin's original work between 1966 and 1992 [15]–[20], the model has been subjected to several adaptations to account for various mechanisms that drive work hardening behaviour [21], [22], [24]–[27]. Among the most recent adaptions is the extension of the model to the description of dislocation density evolution in the finite-strain regime [27], [28]. In this work, the single-parameter Kocks-Mecking model, due to its popularity, and the finite-strain Hariharan-Barlat model [27] are used to describe the evolution of average dislocation density. The Hariharan-Barlat model has been developed to extend the description of average dislocation density evolution into the non-linear, finite-strain regime, and is, therefore, an appropriate choice for this work. An evolution equation for the internal state hardening variable in the proposed dislocation density-based elastoplasticity model is extracted from each of these models.

1.3 Structure of the Dissertation

This dissertation comprises nine chapters. The mathematical notation and conventions used in this work and a broad overview of fundamental continuum mechanics quantities are presented in Chapter 2. Thereafter, a short overview of key dislocation and work hardening theory concepts is provided in Chapter 3, which provides the theoretical basis for an examination of the Kocks-Mecking and Hariharan-Barlat evolution equations in Chapter 4. An introduction to constitutive modelling and a typical initial value problem for finite-strain, rate-dependent elastoplasticity is presented in Chapter 5.

Following these preparatory chapters, a constitutive model for finite-strain, rate-dependent elastoplasticity based on the evolution of dislocation density is presented in Chapter 6. The temporal discretization and material-point-level implementation of the constitutive model is included in Chapter 6, and the material point-level numerical implementation is verified in Chapter 7. Parameter determination for the dislocation density evolution equations is demonstrated in Chapter 8, and the effect of parameter variation on the material response is briefly examined. The results obtained from quasi-static loading simulations using the parameters determined at the beginning of the chapter follow. Results from three separate analyses are presented across Chapters 7 and 8; therefore, in the interest of coherence, the traditional standalone discussion chapter is omitted in this dissertation in favour of a discussion section within each chapter. A brief conclusion and recommendations for future works concludes this dissertation in Chapter 9.

Chapter 2

Continuum Mechanics Preliminaries

This chapter concerns the necessary fundamental tensor algebra and continuum mechanics preliminaries that are required throughout this work. The notation for tensors, algebraic operations, and tensor calculus is introduced in Section 2.1, and should be read in conjunction with the glossary of conventions and notations included in the preamble of this dissertation.

Following the establishment of notation and conventions, several fundamental kinematic and kinetic quantities are introduced in Section 2.2, Section 2.3 and Section 2.5, respectively. In an introductory text to continuum mechanics, a discussion on the balance laws would naturally follow on from Section 2.3; as these laws are not called upon in this work, this discussion is omitted, but it may be found in [29]–[33]. The thermodynamic concepts essential to the construction of a finite-strain elastoplasticity model are presented in Section 2.4.

2.1 Mathematical Notation and Conventions

Essential tensor algebraic operations and tensor calculus notation are presented in this section.

2.1.1 Notation for Tensors and Algebraic Operations

Vectors are denoted with a boldface, lowercase letter, e.g. $\boldsymbol{a}$, second-order tensors are denoted by a boldface, uppercase letter, e.g. $\boldsymbol{A}$, and fourth-order tensors are denoted by an blackboard bold, uppercase letter, e.g. $\mathbb{A}$. An exception to this rule is the boldface, uppercase $\boldsymbol{X}$ which is a vector denoting the position of a point in the material domain. Diagonal second-order tensors may be abbreviated in the form

$$\boldsymbol{A} = \operatorname{diag}\left[a \quad b \quad c\right]. \tag{2.1}$$

The Einstein summation convention is used to imply summation over a set of repeated indices. For example,

$$a_i b_i \quad \text{implies} \quad \sum_{i=1}^{n} a_i b_i = a_1 b_1 + a_2 b_2 + \cdots + a_n b_n \tag{2.2}$$

Orthonormal basis vectors are denoted by $\boldsymbol{e}_i$. Components of vectors with respect to the basis are given in a lightface script as follows:

$$a_i \boldsymbol{e}_i. \tag{2.3}$$

The basis vectors are used to create a basis for higher order tensors by means of the tensor product operator, $\otimes$. The standard tensor product is defined through the relation

$$[\boldsymbol{a} \otimes \boldsymbol{b}]\, \boldsymbol{c} = \boldsymbol{a}\, [\boldsymbol{b} \cdot \boldsymbol{c}]\,, \tag{2.4}$$

where $\cdot$ is the dot product operator. The tensor dot product operator $\odot$ is defined as such:

$$\boldsymbol{A} \odot \boldsymbol{B} = [A_{ij} \boldsymbol{e}_i \otimes \boldsymbol{e}_j] \odot [B_{kl} \boldsymbol{e}_k \otimes \boldsymbol{e}_l] = A_{ik} B_{lj} \boldsymbol{e}_i \otimes \boldsymbol{e}_j \otimes \boldsymbol{e}_k \otimes \boldsymbol{e}_l. \tag{2.5}$$

The symmetric part of a tensor is denoted by $\operatorname{sym}(\bullet)$, which indicates

$$\operatorname{sym}(\boldsymbol{A}) = \frac{1}{2} \left[\boldsymbol{A} + \boldsymbol{A}^T \right]. \tag{2.6}$$

Similarly, the skew part of a tensor is denoted by $\operatorname{skw}(\bullet)$, which indicates

$$\operatorname{skw}(\boldsymbol{A}) = \frac{1}{2} \left[\boldsymbol{A} - \boldsymbol{A}^T \right]. \tag{2.7}$$

Special Tensors

The components of the second-order identity tensor $\boldsymbol{I}$ are equivalent to the Kronecker delta:

$$\delta_{ij} := \begin{cases} 1, & \text{if } i = j, \\ 0, & \text{if } i \neq j. \end{cases} \tag{2.8}$$

The isochoric operator tensor is defined as

$$\mathbb{P} = \boldsymbol{I} \odot \boldsymbol{I} - \frac{1}{3} \boldsymbol{I} \otimes \boldsymbol{I}, \tag{2.9}$$

such that its application to a tensor, $\boldsymbol{A}$, results in the isochoric part of $\boldsymbol{A}$:

$$\mathbb{P}\boldsymbol{A} = \boldsymbol{A} - \frac{1}{3}\boldsymbol{I}\,\mathrm{tr}\,(\boldsymbol{A})\,. \tag{2.10}$$

2.1.2 Tensor Calculus

Partial derivatives of a scalar field φ, vector $\boldsymbol{a}$, or tensor $\boldsymbol{A}$ with respect to a vector $\boldsymbol{b}$, or tensor $\boldsymbol{B}$ are defined as follows

$$\frac{\partial \varphi}{\partial \boldsymbol{b}} := \frac{\partial \varphi}{\partial b_i}\boldsymbol{e}_i, \qquad \frac{\partial \boldsymbol{a}}{\partial \boldsymbol{b}} := \frac{\partial a_i}{\partial b_j}\boldsymbol{e}_i \otimes \boldsymbol{e}_j$$
$$\frac{\partial \varphi}{\partial \boldsymbol{B}} := \frac{\partial \varphi}{\partial B_{ij}}\boldsymbol{e}_i \otimes \boldsymbol{e}_j, \qquad \frac{\partial \boldsymbol{A}}{\partial \boldsymbol{B}} := \frac{\partial A_{ij}}{\partial B_{kl}}\boldsymbol{e}_i \otimes \boldsymbol{e}_j \otimes \boldsymbol{e}_k \otimes \boldsymbol{e}_l$$

The gradient of scalar and vector fields with respect to the material domain is given by

$$\mathrm{Grad}\,(\varphi) := \frac{\partial \varphi}{\partial \boldsymbol{X}} = \frac{\partial \varphi}{\partial X_j}\boldsymbol{e}_j, \quad \mathrm{Grad}\,(\boldsymbol{a}) := \frac{\partial \boldsymbol{a}}{\partial \boldsymbol{X}} = \frac{\partial a_i}{\partial X_j}\boldsymbol{e}_i \otimes \boldsymbol{e}_j,$$

and the gradient with respect to the spatial domain is given by

$$\mathrm{grad}\,(\varphi) := \frac{\partial \varphi}{\partial \boldsymbol{x}} = \frac{\partial \varphi}{\partial x_j}\boldsymbol{e}_j, \quad \mathrm{grad}\,(\boldsymbol{a}) := \frac{\partial \boldsymbol{a}}{\partial \boldsymbol{x}} = \frac{\partial a_i}{\partial x_j}\boldsymbol{e}_i \otimes \boldsymbol{e}_j,$$

accordingly. The divergence of vector and tensor fields with respect to the material domain is given by

$$\mathrm{Div}\,(\boldsymbol{a}) := \frac{\partial \boldsymbol{a}}{\partial \boldsymbol{X}} = \frac{\partial a_i}{\partial X_i}, \quad \mathrm{Div}\,(\boldsymbol{A}) := \frac{\partial \boldsymbol{A}}{\partial \boldsymbol{X}} = \frac{\partial A_{ij}}{\partial X_j}\boldsymbol{e}_i,$$

and the divergence with respect to the spatial domain is given by

$$\mathrm{div}\,(\boldsymbol{a}) := \frac{\partial \boldsymbol{a}}{\partial \boldsymbol{x}} = \frac{\partial a_i}{\partial x_i}, \quad \mathrm{div}\,(\boldsymbol{A}) := \frac{\partial \boldsymbol{A}}{\partial \boldsymbol{x}} = \frac{\partial A_{ij}}{\partial x_j}\boldsymbol{e}_i.$$

The derivatives of the inverse of tensors result in

$$\frac{\partial \boldsymbol{A}^{-1}}{\partial \boldsymbol{A}} = -\boldsymbol{A}^{-1} \odot \boldsymbol{A}^{-1} \quad \text{and} \quad \frac{\partial \boldsymbol{A}^{-T}}{\partial \boldsymbol{A}} = -\boldsymbol{A}^{-T} \odot \boldsymbol{A}^{-T}. \tag{2.11}$$

2.2 Kinematics

Kinematics describe the motion and possible deformations a body may undertake without reference to the forces that cause the motion. A brief overview of the fundamental principles as they are presented in [29]–[33] follows.

2.2.1 Motion

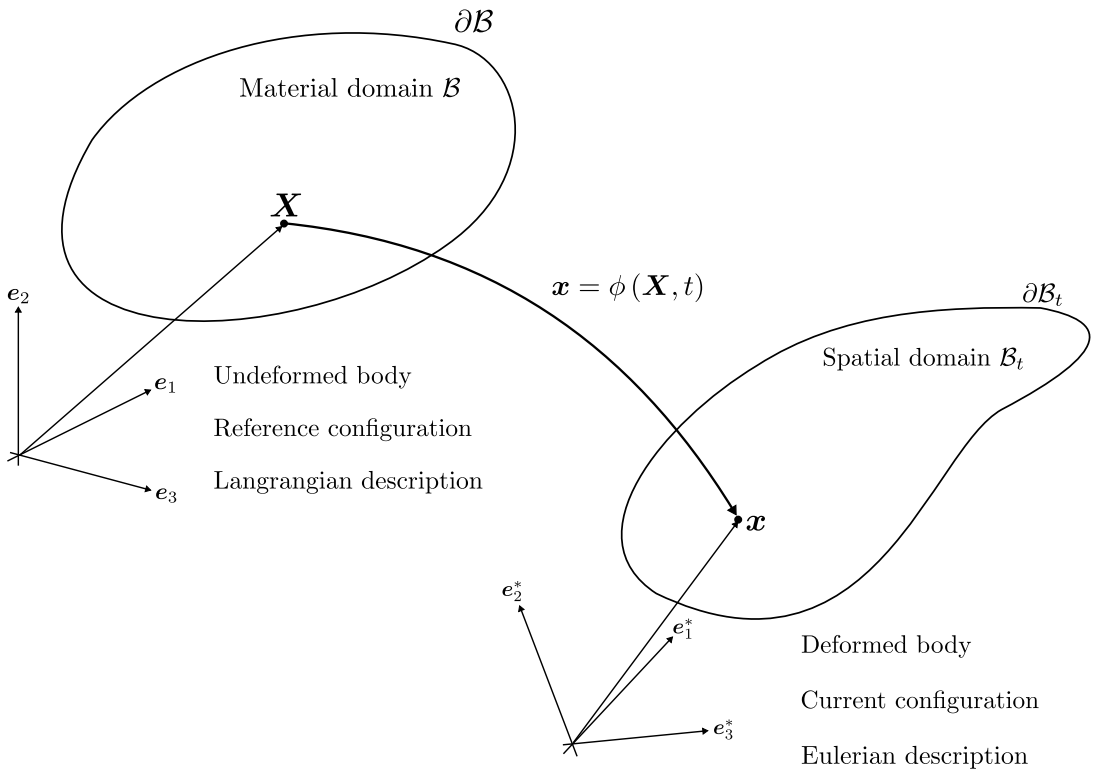

Figure 2.1: A material and a spatial domain.

Consider the arbitrary material and spatial domains in Figure 2.1, indicated by $\mathcal{B}$ and $\mathcal{B}_t$, respectively. $\mathcal{B}$ is enclosed by the boundary $\partial\mathcal{B}$, and $\mathcal{B}_t$ is enclosed by the boundary $\partial\mathcal{B}_t$. During the deformation of the domain, each material point $\boldsymbol{X} \in \mathcal{B}$ undergoes a motion to a point $\boldsymbol{x} \in \mathcal{B}_t$. The map ϕ describes the motion of the domain at each time t as a one-to-one mapping,

$$\boldsymbol{x} = \phi(\boldsymbol{X}, t). \tag{2.12}$$

Each point $\boldsymbol{X} \in \mathcal{B}$ is uniquely mapped to some point $\boldsymbol{x} \in \mathcal{B}_t$; therefore, the map is invertible,

$$\boldsymbol{X} = \phi^{-1}(\boldsymbol{x}, t). \tag{2.13}$$

The displacement of a material point originally located at $\boldsymbol{X}$ at time t is

$$\boldsymbol{u}(\boldsymbol{X}, t) := \boldsymbol{x} - \boldsymbol{X}. \tag{2.14}$$

A relation between line elements in the material domain and line elements in the spatial domain can be determined to be,

$$\mathrm{d}x_i = \frac{\partial \phi_i}{\partial X_j} \mathrm{d}X_j. \tag{2.15}$$

The deformation gradient is thus defined as

$$\boldsymbol{F}(\boldsymbol{X},t) := \frac{\partial \phi(\boldsymbol{X},t)}{\partial \boldsymbol{X}}, \tag{2.16}$$

so that

$$\mathrm{d}x_i = F_{ij}\mathrm{d}X_j. \tag{2.17}$$

Since the map $\phi(\boldsymbol{X},t)$ is invertible, the determinant of $\boldsymbol{F}$ is

$$\det(\boldsymbol{F}) = \det\left(\frac{\partial \phi}{\partial \boldsymbol{X}}\right) \neq 0, \tag{2.18}$$

and its inverse $\boldsymbol{F}^{-1}$ exists. An alternative expression for the deformation gradient can be found from Equations (2.14) and (2.16):

$$\boldsymbol{F} = \operatorname{Grad}(\boldsymbol{X}+\boldsymbol{u}) = \boldsymbol{I} + \operatorname{Grad}(\boldsymbol{u}). \tag{2.19}$$

The deformation gradient further lends itself to a useful identity that relates the gradient operators,

$$\operatorname{Grad}(\bullet) = \frac{\partial \bullet}{\partial \boldsymbol{X}} = \frac{\partial \bullet}{\partial \boldsymbol{x}}\frac{\partial \boldsymbol{x}}{\partial \boldsymbol{X}} = \operatorname{grad}(\bullet)\boldsymbol{F}. \tag{2.20}$$

2.2.2 Deformation

Consider the relation between a line element in the material domain and its counterpart in the spatial domain,

$$\begin{aligned} \mathrm{d}\boldsymbol{x}\cdot\mathrm{d}\boldsymbol{x} = \|\mathrm{d}\boldsymbol{x}\|^2 &= \boldsymbol{F}\mathrm{d}\boldsymbol{X}\cdot\boldsymbol{F}\mathrm{d}\boldsymbol{X}, \\ &= \mathrm{d}\boldsymbol{X}^T\boldsymbol{F}^T\boldsymbol{F}\mathrm{d}\boldsymbol{X}. \end{aligned} \tag{2.21}$$

From this relation, it is convenient to define the right Cauchy-Green tensor as

$$\boldsymbol{C} := \boldsymbol{F}^T\boldsymbol{F}, \tag{2.22}$$

so that

$$\|\mathrm{d}\boldsymbol{x}\|^2 = \mathrm{d}\boldsymbol{X}\cdot\boldsymbol{C}\mathrm{d}\boldsymbol{X}. \tag{2.23}$$

To relate a line in the spatial domain to its counterpart in the material domain, it is similarly convenient to define the left Cauchy-Green tensor as

$$\boldsymbol{B} := \boldsymbol{F}\boldsymbol{F}^T \tag{2.24}$$

so that

$$\|\mathrm{d}\boldsymbol{X}\|^2 = \mathrm{d}\boldsymbol{x}\cdot\boldsymbol{B}^{-1}\mathrm{d}\boldsymbol{x}. \tag{2.25}$$

Both the right and left Cauchy-Green deformation tensors are symmetric. The change in length of a line element over a motion can therefore be expressed as

$$\begin{aligned}\frac{1}{2}\left[\|\mathrm{d}\boldsymbol{x}\|^2 - \|\mathrm{d}\boldsymbol{X}\|^2\right] &= \frac{1}{2}\left[\mathrm{d}\boldsymbol{X}^T\boldsymbol{C}\mathrm{d}\boldsymbol{X} - \mathrm{d}\boldsymbol{X}^T\mathrm{d}\boldsymbol{X}\right], \\ &= \mathrm{d}\boldsymbol{X}\cdot\frac{1}{2}[\boldsymbol{C}-\boldsymbol{I}]\mathrm{d}\boldsymbol{X},\end{aligned} \tag{2.26}$$

from which a useful tensorial representation of finite strain, the Green-Lagrange strain, is defined as

$$\boldsymbol{E} := \frac{1}{2}\left[\boldsymbol{C}-\boldsymbol{I}\right] = \frac{1}{2}\left[\boldsymbol{F}^T\boldsymbol{F}-\boldsymbol{I}\right]. \tag{2.27}$$

The Green-Lagrange strain is necessarily symmetric. An alternative form of the Green-Lagrange strain is obtained from the definition of the deformation gradient given by Equation (2.19),

$$\begin{aligned}\boldsymbol{E} &= \frac{1}{2}\left[(\boldsymbol{I} + \operatorname{Grad}(\boldsymbol{u}))^T(\boldsymbol{I} + \operatorname{Grad}(\boldsymbol{u})) - \boldsymbol{I}\right] \\ &= \frac{1}{2}\left[\operatorname{Grad}(\boldsymbol{u})^T\operatorname{Grad}(\boldsymbol{u}) + \operatorname{Grad}(\boldsymbol{u}) + \operatorname{Grad}(\boldsymbol{u})^T\right].\end{aligned} \tag{2.28}$$

If the norm

$$\|\operatorname{Grad}(\boldsymbol{u})\| \ll 1, \tag{2.29}$$

or, equivalently, if $\boldsymbol{F}$ is sufficiently close to $\boldsymbol{I}$, and therefore

$$\|\operatorname{Grad}(\boldsymbol{u})^T\operatorname{Grad}(\boldsymbol{u})\| \ll \|\operatorname{Grad}(\boldsymbol{u})\|, \tag{2.30}$$

the infinitesimal strain tensor may be used:

$$\boldsymbol{E} \approx \boldsymbol{\varepsilon} := \frac{1}{2}\left[\operatorname{Grad}(\boldsymbol{u}) + \operatorname{Grad}(\boldsymbol{u})^T\right]. \tag{2.31}$$

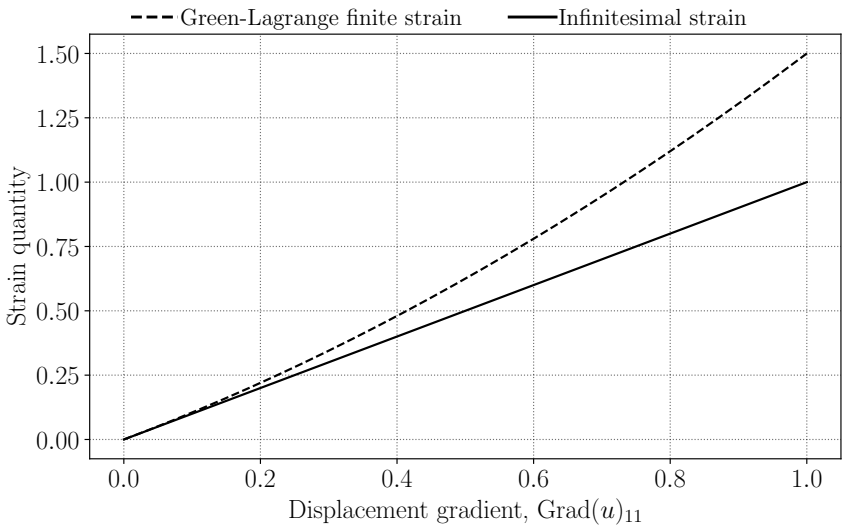

Figure 2.2: Divergence of Green-Lagrange strain from infinitesimal strain for the motion $x = [1 + a[t]]X$, from which the displacement gradient, $\mathrm{Grad}\,(\boldsymbol{u})_{11}$ is computed. E_{11} and ε_{11} are plotted across the displacement gradient. As the deformation increases, the difference between the finite-strain and infinitesimal-strain measures increases.

The assumption of infinitesimally-small displacement gradients leads to a linear description for strain, but the limitation of this convenience is demonstrated in Figure 2.2. Below a displacement gradient of around 0.1, there appears to be little difference between the two strain measures. Beyond this point, however, the quadratic growth of the finite-strain tensor rapidly outpaces its linear infinitesimal counterpart. Evidently, a small-strain approximation is not appropriate for the description of finite deformations.

The relevance of this observation is apparent from Chapter 4 onwards, where the implementation of the Kocks-Mecking model is reviewed. Implementations of the Kocks-Mecking model in finite-strain contexts that are constructed in an infinitesimal-strain setting introduce the error demonstrated in Figure 2.2.

2.2.3 Volume Change

The change in volume of a spatial infinitesimal volume element, $\mathrm{d}v$, with respect to the change in volume of a material infinitesimal volume element, $\mathrm{d}V$, may be given by [29], [30]

$$\det(\boldsymbol{F}) = \frac{\mathrm{d}v}{\mathrm{d}V}. \tag{2.32}$$

From this relation, the volumetric Jacobian J is defined as

$$J := \det(\boldsymbol{F}) \tag{2.33}$$

so that

$$\mathrm{d}v = J\mathrm{d}V. \tag{2.34}$$

As no motion may lead to an infinitesimal volume within a body to be zero or negative, it is required that

$$J > 0. \tag{2.35}$$

2.2.4 Rate Quantities

Material and Spatial Time Derivatives

Generally, for any given quantity ξ, the material-time derivative is written as

$$\dot{\xi}(\boldsymbol{X}, t) = \frac{\partial \xi(\boldsymbol{X}, t)}{\partial t}, \tag{2.36}$$

and the spatial-time derivative is written as

$$\xi'(\boldsymbol{x}, t) = \frac{\partial \xi(\boldsymbol{x}, t)}{\partial t}. \tag{2.37}$$

Velocity is a useful quantity obtained by differentiating the displacement $\boldsymbol{u}$ with respect to time:

$$\dot{\boldsymbol{u}}(\boldsymbol{X}, t) = \frac{\partial \boldsymbol{u}(\boldsymbol{X}, t)}{\partial t}. \tag{2.38}$$

Rate of Deformation

Consider the rate of deformation gradient given by

$$\dot{\boldsymbol{F}} = \frac{\partial}{\partial t}(\boldsymbol{I} + \operatorname{Grad}(\boldsymbol{u})) = \operatorname{Grad}(\dot{\boldsymbol{u}}). \tag{2.39}$$

The velocity gradient is defined as

$$\boldsymbol{L} := \operatorname{grad}(\dot{\boldsymbol{u}}). \tag{2.40}$$

The identity in Equation (2.20) may be used to reformulate Equation (2.39) to give

$$\dot{\boldsymbol{F}} = \operatorname{grad}(\dot{\boldsymbol{u}})\,\boldsymbol{F} \tag{2.41}$$

so that

$$\boldsymbol{L} = \dot{\boldsymbol{F}}\boldsymbol{F}^{-1}. \tag{2.42}$$

The velocity gradient can be decomposed into deformation and spin components,

$$\boldsymbol{L} = \boldsymbol{D} + \boldsymbol{W}, \tag{2.43}$$

where the rate of deformation tensor $\boldsymbol{D}$ is the symmetric part of $\boldsymbol{L}$, and the spin tensor, $\boldsymbol{W}$, is the skew part:

$$\boldsymbol{D} := \frac{1}{2}\left[\boldsymbol{L} + \boldsymbol{L}^T\right], \quad \boldsymbol{W} := \frac{1}{2}\left[\boldsymbol{L} - \boldsymbol{L}^T\right]. \tag{2.44}$$

It is now convenient to formulate the rate of the Green-Lagrange strain:

$$\dot{\boldsymbol{E}} = \frac{1}{2}\left[\dot{\boldsymbol{F}}^T\boldsymbol{F} + \boldsymbol{F}^T\dot{\boldsymbol{F}}\right]. \tag{2.45}$$

$$\tag{2.46}$$

Using Equations (2.40), (2.43), and (2.45) the rate of the Green-Lagrange strain can be conveniently expressed in the form

$$\dot{\boldsymbol{E}} = \boldsymbol{F}^T\boldsymbol{D}\boldsymbol{F}. \tag{2.47}$$

2.3 Stress

Stress is a description of the state of the internal forces within a body. A stress tensor operates on a unit normal vector to give a traction vector.

2.3.1 The Cauchy Stress

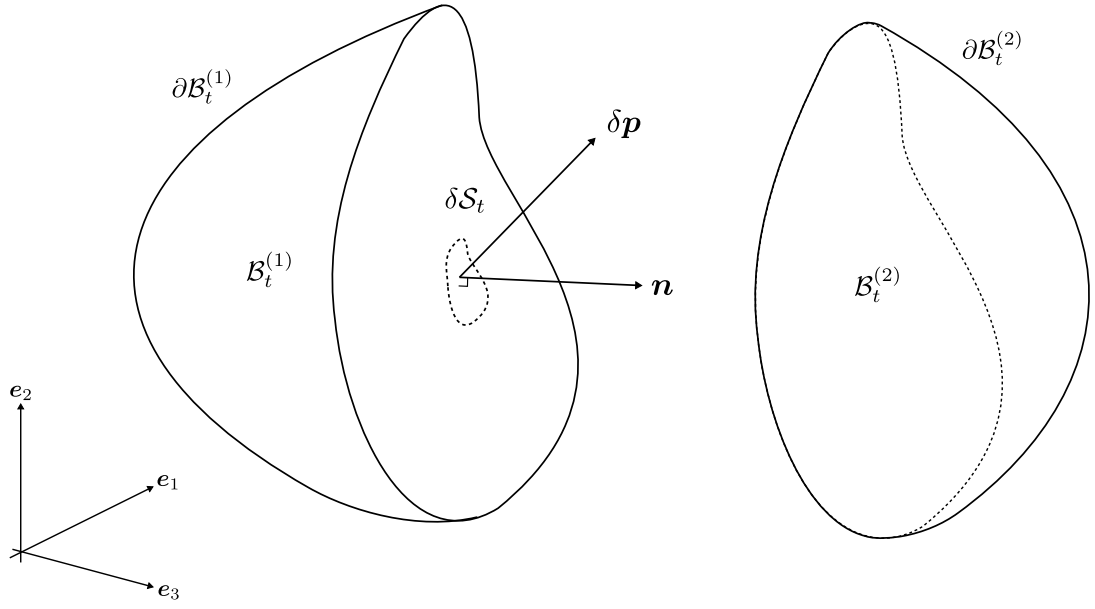

Figure 2.3: A cross-section of spatial region $\mathcal{B}_t$ is performed such that an infinitesimally small area of the internal surface, $\delta\mathcal{S}_t$, on $\mathcal{B}_t^{(1)}$ is revealed. The effect of the removed body, $\mathcal{B}_t^{(2)}$, on $\mathcal{B}_t^{(1)}$ is represented by the force $\delta\boldsymbol{p}$.

Consider once again an arbitrary region $\mathcal{B}_t$ in the spatial domain bounded by the surface $\partial\mathcal{B}_t$ as in Figure 2.3. A cross-section of $\mathcal{B}_t$ is performed such that an infinitesimally small area of the internal surface, $\delta\mathcal{S}_t$, is revealed. The effect of the removed body is represented on the surface $\delta\mathcal{S}_t$ by the force $\delta\boldsymbol{p}$, and an outward unit vector $\boldsymbol{n}$ indicates the direction normal to the internal surface. The current surface traction, $\boldsymbol{t}$, is defined as the force acting per unit of infinitesimal area exerted upon $\mathcal{B}_t^{(1)}$ by the removed surface on $\mathcal{B}_t^{(2)}$,

$$\boldsymbol{t}(\boldsymbol{x}, t, \boldsymbol{n}) := \lim_{\delta\mathcal{S}_t \to 0} \frac{\delta\boldsymbol{p}}{\delta\mathcal{S}_t}. \tag{2.48}$$

The magnitude and orientation of the traction depends on the orientation of the surface. Cauchy's stress theorem states that a normal vector $\boldsymbol{n}$ is related to a current traction $\boldsymbol{t}$ by a second-order spatial tensor field, $\boldsymbol{\sigma}$, termed the Cauchy stress,

$$\boldsymbol{t}(\boldsymbol{x}, t, \boldsymbol{n}) = \boldsymbol{\sigma}(\boldsymbol{x}, t)\,\boldsymbol{n}. \tag{2.49}$$

The Cauchy stress is symmetric within a Cartesian coordinate system. A consequence of Cauchy's theorem, Cauchy's lemma, is that for all unit vectors $\boldsymbol{n}$,

$$\boldsymbol{t}(\boldsymbol{x}, t, \boldsymbol{n}) = -\boldsymbol{t}(\boldsymbol{x}, t, -\boldsymbol{n}). \tag{2.50}$$

2.3.2 The First Piola-Kirchhoff Stress

A stress quantity suitable for the expression force and moment balances in the material domain is of great use. Let $\boldsymbol{T}$ be the traction over some infinitesimal area $\delta\mathcal{S}$ in the material domain,

$$\boldsymbol{T}(\boldsymbol{X}, t, \boldsymbol{N}) := \lim_{\delta\mathcal{S} \to 0} \frac{\delta\boldsymbol{p}}{\delta\mathcal{S}}, \tag{2.51}$$

where $\delta\boldsymbol{p}$ is the same force used to define the current traction in Section 2.3.1. The material and spatial tractions over their respective area elements are related by

$$\boldsymbol{T}(\boldsymbol{X}, t, \boldsymbol{N})\mathrm{d}A = \boldsymbol{t}(\boldsymbol{x}, t, \boldsymbol{n})\mathrm{d}a. \tag{2.52}$$

The Cauchy stress relates $\boldsymbol{t}$ and $\boldsymbol{n}$ in the spatial domain, and so a second-order tensor that provides the same utility for $\boldsymbol{T}$ and $\boldsymbol{N}$ in the material domain is necessary. Consider the contact force on a surface $\partial\mathcal{P}_t \in \mathcal{B}_t$:

$$\int_{\partial\mathcal{P}_t} \boldsymbol{\sigma}\boldsymbol{n}\mathrm{d}a \tag{2.53}$$

The material area elements, $\mathrm{d}a$, are transformed to the material domain using Nanson's relation, which relates infinitesimal areas in the spatial domain to their counterparts in

the material domain. Thus, the force over the reference surface, $\partial\mathcal{P}$, is

$$\int_{\partial\mathcal{P}} J\boldsymbol{\sigma}\boldsymbol{F}^{-T}\boldsymbol{N}\mathrm{d}A. \tag{2.54}$$

One defines the first Piola-Kirchhoff stress as

$$\boldsymbol{P} := J\boldsymbol{\sigma}\boldsymbol{F}^{-T}, \tag{2.55}$$

so that the contact force may be represented in the spatial and material domains as such:

$$\int_{\partial\mathcal{P}_t} \boldsymbol{\sigma}\boldsymbol{n}\mathrm{d}a = \int_{\partial\mathcal{P}} \boldsymbol{P}\boldsymbol{N}\mathrm{d}A. \tag{2.56}$$

The first Piola-Kirchhoff stress is measured per unit area in the material domain, and it is generally not symmetric.

2.4 Thermodynamics

While existing dislocation density-based constitutive models may be able to superficially match some experimental results, extreme deformation and deformation at elevated temperatures, as experienced in many forming operations, require careful treatment of thermodynamic effects. Although this work does not consider a thermally-linked problem, the need for thermodynamic consistency is evident. This requirement places some restrictions on the model. This restriction is imposed via the Coleman-Noll procedure [2] in Chapter 5, which requires some knowledge of fundamental thermodynamics concepts. The essential concepts are briefly explained in this section.

A body is constrained by two thermodynamic laws, namely

i) the balance of energy,

ii) and the imbalance of entropy.

These laws are briefly described in Appendix A along with the concept of Helmholtz free energy. In this section, only the most relevant concepts are introduced, namely the reduced dissipation inequality and work conjugacy. A more detailed discussion on thermodynamics can be found in [29]–[31].

Reduced Dissipation Inequality

A portion of the power expended on a region is dissipated – that is, the internal power is not entirely converted into changes in kinetic energy or free energy. Therefore, for

isothermal problems the dissipation inequality is denoted

$$\mathcal{D}(\mathcal{B}_t) := \dot{u}_{\text{int}} - \rho_m \dot{\Psi} = \boldsymbol{\sigma} : \boldsymbol{D} - \rho_m \dot{\Psi} \geq 0, \tag{2.57}$$

where

(i) $\mathcal{D}(\mathcal{B}_t)$ represents the dissipation by unit volume in the spatial region $\mathcal{B}_t$,

(ii) $\dot{u}_{int}$ is the specific internal work per spatial unit volume,

(iii) ρ_m is the specific mass density, and

(iv) Ψ is the Helmholtz free energy.

Equation (2.57) is the local form of the Clausius-Duhem inequality. Where it is not appropriate to assume that temperature field $\vartheta(\boldsymbol{x}, t)$ is constant, the local energy balance given by

$$\rho_m \dot{u}_{\text{int}} = \boldsymbol{\sigma} : \boldsymbol{D} - \text{ div}(\mathbf{q}) + r, \tag{2.58}$$

and local entropy imbalance given by Equation (A.19) combine to yield the spatial local free-energy imbalance,

$$\rho_m \left[\dot{\Psi} + \eta\dot{\vartheta}\right] - \boldsymbol{\sigma} : \boldsymbol{D} + \frac{1}{\vartheta}\boldsymbol{q} \cdot \text{ grad}(\vartheta) \leq 0. \tag{2.59}$$

The corresponding dissipation inequality is

$$\mathcal{D}(\mathcal{B}_t) := \boldsymbol{\sigma} : \boldsymbol{D} - \rho_m \left[\dot{\Psi} + \eta\dot{\vartheta}\right] - \frac{1}{\vartheta}\boldsymbol{q} \cdot \text{ grad}(\vartheta) \geq 0 \tag{2.60}$$

The local free-energy imbalance can be expressed referentially, noting that the material domain and density are independent of time, and that

$$\mathbf{Q}_{\text{R}} = J\boldsymbol{F}^{-1}\boldsymbol{q}, \tag{2.61}$$

$$\mathcal{D}(\mathcal{B}) = J\mathcal{D}(\mathcal{B}_t), \tag{2.62}$$

$$\Psi = \rho_R \Psi = U_{\text{int}} - \Theta N. \tag{2.63}$$

Thus, the reduced dissipation inequality is expressed for material domain as such:

$$\mathcal{D}(\mathcal{B}) := \boldsymbol{S} : \dot{\boldsymbol{E}} - \dot{\Psi} - N\dot{\Theta} - \frac{1}{\Theta}\mathbf{Q}_{\text{R}} \cdot \text{ Grad}(\Theta) \geq 0. \tag{2.64}$$

Equations (2.60) and (2.64) may be further reduced for mechanical theories where thermal influences are considered negligible:

$$\mathcal{D}(\mathcal{B}_t) := \boldsymbol{\sigma} : \boldsymbol{D} - \dot{\Psi} \geq 0 \tag{2.65}$$

$$\mathcal{D}(\mathcal{B}) := \boldsymbol{S} : \dot{\boldsymbol{E}} - \dot{\Psi} \geq 0. \tag{2.66}$$

In the material expression for the reduced dissipation inequality, an alternative stress quantity, the second Piola-Kirchhoff stress $\boldsymbol{S}$, is used. The use of this quantity is motivated by an explanation of work conjugacy in the following section, Section 2.4.1, and the stress quantity is derived in the section thereafter, Section 2.5.2.

2.4.1 Work Conjugacy

If the product of a stress and strain rate measure is used to define the internal power expended per unit volume, the stress and strain rate pairing is known as a work-conjugate pair [29]–[31]. In the local energy balance in Equation (2.58), the internal power per unit spatial volume is given by the work-conjugate pair

$$\boldsymbol{\sigma} : \boldsymbol{D}. \tag{2.67}$$

Here, the Cauchy stress, $\boldsymbol{\sigma}$, is the stress quantity that is work-conjugate to the rate of deformation tensor, $\boldsymbol{D}$. Alternative measures of stress power may be used to capture the internal power under isothermal conditions in a material region, which is seen by the work-conjugate pair

$$\boldsymbol{S} : \dot{\boldsymbol{E}} \tag{2.68}$$

in the material expression for the reduced dissipation inequality in Equation (2.64). The work-conjugate pairing of stress and strain measures motivates the definition of alternative measures of stress, which are introduced in the following section.

2.5 Alternative Stress Quantities

In this section, the concept of work conjugacy (Section 2.4.1) is used to motivate for the definition of two useful stress quantities.

2.5.1 The Kirchhoff Stress

The Kirchhoff stress tensor provides an alternative spatial stress tensor that scales the Cauchy stress by the volumetric Jacobian,

$$\boldsymbol{\tau} := J\boldsymbol{\sigma}. \tag{2.69}$$

This stress tensor is useful because it is work-conjugate to the rate of deformation tensor, $\boldsymbol{D}$.

2.5.2 The Second Piola-Kirchhoff Stress

The second Piola-Kirchhoff stress is defined so that the energy imbalance introduced in Appendix Section A.2 may be expressed materially. Consider the work-conjugate pairing $\boldsymbol{\tau} : \boldsymbol{D}$. Using the definition of the rate of the Green-Lagrange strain in Equation (2.47), the internal power may be expressed as

$$\boldsymbol{\tau} : \boldsymbol{D} = \left[\boldsymbol{F}^{-1}\boldsymbol{\tau}\boldsymbol{F}^{-T}\right] : \dot{\boldsymbol{E}}. \tag{2.70}$$

Therefore, it is convenient to define the stress quantity that is conjugate to the rate of the Green-Lagrange strain to be

$$\boldsymbol{S} := \boldsymbol{F}^{-1}\boldsymbol{\tau}\boldsymbol{F}^{-T}, \tag{2.71}$$

which is known as the second Piola-Kirchhoff stress. The specific internal work expended upon a material region $\dot{U}_{\text{int}}$ may be given by

$$\dot{U}_{\text{int}} = \frac{1}{2}\boldsymbol{S} : \dot{\boldsymbol{C}} = \boldsymbol{S} : \dot{\boldsymbol{E}}, \tag{2.72}$$

where the second Piola-Kirchhoff stress is work-conjugate to the strain rate, $\dot{\boldsymbol{E}}$. Using Equations (2.55) and (2.69), the second Piola-Kirchhoff stress may be related to the Cauchy stress via the Piola transformation [33]:

$$\boldsymbol{S} = J\boldsymbol{F}^{-1}\boldsymbol{\sigma}\boldsymbol{F}^{-T} = \boldsymbol{F}^{-1}\boldsymbol{P} = \boldsymbol{S}^{T}. \tag{2.73}$$

2.6 Summary of Key Equations

The key equations presented in this chapter are summarised in what follows.

Kinematics

Motion

Motion: $$\boldsymbol{x} = \phi\left(\boldsymbol{X}, t\right) = \boldsymbol{X} + \boldsymbol{u}\left(\boldsymbol{X}, t\right) \tag{2.74}$$

Deformation

Deformation gradient: $$\boldsymbol{F} = \frac{\partial \phi}{\partial \boldsymbol{X}} \tag{2.75}$$

Right Cauchy-Green tensor: $$\boldsymbol{C} = \boldsymbol{F}^{T}\boldsymbol{F} \tag{2.76}$$

Left Cauchy-Green tensor: $$\boldsymbol{B} = \boldsymbol{F}\boldsymbol{F}^T \tag{2.77}$$

Green-Lagrange strain: $$\boldsymbol{E} = \frac{1}{2}\left[\boldsymbol{C} - \boldsymbol{I}\right] \tag{2.78}$$

Jacobian: $$J = \frac{\mathrm{d}v}{\mathrm{d}V} = \det\left(\boldsymbol{F}\right) = \sqrt{\det\left(\boldsymbol{C}\right)} = \sqrt{\det\left(\boldsymbol{B}\right)} \tag{2.79}$$

Rate Quantities

Spatial velocity: $$\dot{\boldsymbol{u}}\left(\boldsymbol{x}, t\right) = \frac{\partial \phi\left(\boldsymbol{X}, t\right)}{\partial t} \tag{2.80}$$

Velocity gradient: $$\boldsymbol{L} = \frac{\partial \dot{\boldsymbol{u}}\left(\boldsymbol{x}, t\right)}{\partial \boldsymbol{X}} \frac{\partial \boldsymbol{X}}{\partial \boldsymbol{x}} = \dot{\boldsymbol{F}}\boldsymbol{F}^{-1} \tag{2.81}$$

Rate of deformation: $$\boldsymbol{D} = \frac{1}{2}\left[\boldsymbol{L} + \boldsymbol{L}^T\right] \tag{2.82}$$

Rate of strain: $$\dot{\boldsymbol{E}} = \boldsymbol{F}^T\boldsymbol{D}\boldsymbol{F} \tag{2.83}$$

Spin: $$\boldsymbol{W} = \frac{1}{2}\left[\boldsymbol{L} - \boldsymbol{L}^T\right] \tag{2.84}$$

Stress Quantities

Traction: $$\boldsymbol{t} = \boldsymbol{\sigma}\boldsymbol{n} \tag{2.85}$$

Cauchy stress: $$\boldsymbol{\sigma} = \frac{1}{J}\boldsymbol{\tau} \qquad = \frac{1}{J}\boldsymbol{F}\boldsymbol{S}\boldsymbol{F}^T \qquad = \frac{1}{J}\boldsymbol{P}\boldsymbol{F}^T \tag{2.86}$$

Kirchhoff stress: $$\boldsymbol{\tau} = J\boldsymbol{\sigma} \qquad = \boldsymbol{F}\boldsymbol{S}\boldsymbol{F}^T \qquad = \boldsymbol{P}\boldsymbol{F}^T \tag{2.87}$$

First Piola-Kirchhoff stress: $$\boldsymbol{P} = J\boldsymbol{\sigma}\boldsymbol{F}^{-T} \qquad = \boldsymbol{\tau}\boldsymbol{F}^{-T} \qquad = \boldsymbol{F}\boldsymbol{S} \tag{2.88}$$

Second Piola-Kirchhoff stress: $$\boldsymbol{S} = J\boldsymbol{F}^{-1}\boldsymbol{\sigma}\boldsymbol{F}^{-T} \qquad = \boldsymbol{F}^{-1}\boldsymbol{\tau}\boldsymbol{F}^{-T} \qquad = \boldsymbol{F}^{-1}\boldsymbol{P} \tag{2.89}$$

Thermodynamics

Work conjugacy: $$\boldsymbol{\tau} : \boldsymbol{D} = \boldsymbol{S} : \dot{\boldsymbol{E}} \tag{2.90}$$

Reduced dissipation inequality: $$\mathcal{D}\left(\mathcal{B}\right) = \boldsymbol{S} : \dot{\boldsymbol{E}} - \dot{\Psi} \geq 0 \tag{2.91}$$

Chapter 3

Review of Work Hardening Phenomena in Face-Centred Cubic Metals

Work hardening, often called strain hardening, is broadly used to refer to an increase in plastic flow stress as a result of plastic deformation. Manufacturing processes that result in an increased resistance to plastic deformation, like cold-rolling, drawing, or shot-peening, may be modelled using work hardening theories. The development of a unified theory of work hardening behaviour has been a prominent goal of the material science community for several decades, with many of its members lamenting the problem's difficulty with Cottrell's ubiquitous quote "it was the first problem to be attempted by dislocation theory and may be the last to be solved." [15] An elementary understanding of some dislocation theory concepts and work hardening theories is necessary to understand the mechanisms that describe dislocation density evolution which are referenced in the discussion of the Kocks-Mecking and Hariharan-Barlat dislocation density evolution equations in Chapter 4. In the interest of brevity, only the essential terms referenced later on in this work are presented in this chapter, and a more thorough introduction to dislocation and work hardening theory is provided by [15], [34], [35].

This chapter begins with an introduction to selected dislocation theory concepts in Section 3.1, which is followed by a brief introduction to relevant work hardening phenomena in Section 3.2. A summary in Section 3.3 concludes the chapter.

3.1 Dislocation Theory Preliminaries

In this section, three fundamental concepts are explained briefly to provide a background to the work hardening theories that follow in Section 3.2: dislocation motion (Section 3.1.1), thermal activation (Section 3.1.2), and flow stress as it relates to dislocation density (Section 3.1.3). These concepts are explained in more detail in [15], [34], [35]. A unit cell of a face-centred cubic (FCC) crystal structure is shown in Figure 3.1. This is one of the

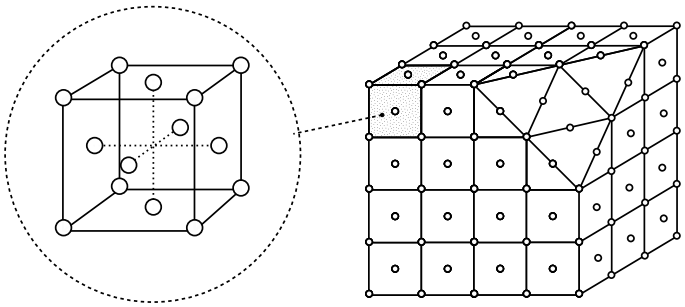

Figure 3.1: A unit cell of face-centred cubic crystalline structure is highlighted to illustrate the position of the constituent atoms. There are constituent atoms on each vertex of the cell and in the centre of each face of the cell. [34]

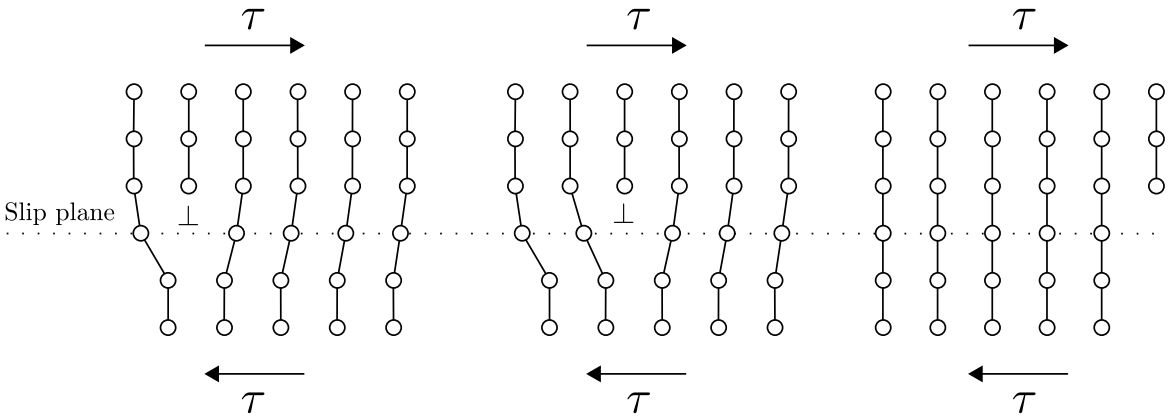

Figure 3.2: A one-dimensional defect, indicated by ⊥, moves through a crystal lattice along a slip plane.

simplest crystalline structures, and it forms the underlying structure of many commonly-used metals and their alloys, such as aluminium, copper, and nickel. Only FCC crystalline solids are considered in this dissertation. Although many of the dislocation motions and interactions described in the sections that follow are analogous to dislocation behaviours in other crystalline structures, most other structures are more complex and therefore demonstrate additional complex dislocation behaviours and properties [34], [35].

3.1.1 Dislocation Motion

Dislocation motion as it pertains to plastic deformation is explained in this section following a brief and elementary description of a dislocation. A comprehensive explanation is found in [34], [35].

The Dislocation

A dislocation is a one-dimensional defect in a crystal structure that causes a mismatch between the number and spacing of atoms in adjacent planes. In Figure 3.2, the planes above the slip plane are gliding to the right as a result of a shear stress τ, and the planes below the slip plane are gliding in the opposite direction as a result of an equal and opposite shear stress. At the slip plane, a dislocation that is indicated by $\perp$ results in a mismatch in the number of atoms on either side of the slip plane. This results in distortion in the lattice, which induces stress in the lattice. A dislocation is described by a Burgers vector that represents the magnitude and direction of the defect in the crystal lattice. The Burgers vector is used to classify dislocations into edge or screw dislocations according to the angle of the dislocation line relative to its Burgers vector.

Slip

Of the several mechanisms which effect plastic deformation, slip is the most evident [35]. Slip is observed as dislocation motion in the direction parallel to the dislocation's Burgers vector and within the plane that contains its line. Plastic deformation by dislocation glide is initiated when the resolved shear stress[1] in the most favourable slip direction on the most favourable slip plane[2] is greater than the slip, or glide, resistance [35]. Dislocation on the secondary slip planes that are unable to travel are termed immobile dislocations or forest dislocations, and the work hardening induced by forest dislocations is termed latent hardening.

The magnitude of the applied stress at which plastic flow initiates is known as the yield stress. To maintain plastic flow, dislocations are required to overcome artefacts that impede dislocation motion, which are known as glide obstacles. The average distance that a dislocation travels before its motion is impeded by a glide obstacle is known as the mean free path.

There are several other types of dislocation motions that are detailed in [34], [35].

3.1.2 Thermal Activation

To maintain plastic flow, dislocations are required to overcome glide obstacles, and the manner in which they are overcome depends on the amount of free energy available in the crystal lattice. The formation of a dislocation requires some amount of free energy proportional to the unit length of the dislocation line, and therefore the free energy of the entire crystal structure is related to the number, distribution, and shape of the dislocations within its lattices. Consequently, dislocation motion and the forces that

[1] The component of shear stress acting along the slip direction on the slip plane with normal to the slip direction.

[2] For an explanation of slip systems, see [35] pp. 6-20

impede dislocation motion result in changes in the free energy of the system. When the energy stored in the crystal is such that the thermal vibration of atoms alone cannot provide the energy required to overcome a glide obstacle, an external stress is required to overcome the glide obstacle via mechanical work. The resulting motion effected by the external stress is known as *athermally* activated dislocation motion. However, if the energy required to surmount the obstacle is only slightly greater than that provided by external stress, the energy shortfall can be provided by thermal vibration, resulting in a motion that is *thermally* activated.

Thermal activation is a statistical phenomenon that is affected by several factors that are well explained in [35]. Given that thermal activation affects dislocation motion, and thus the rate of plastic strain, it is possible to derive a probabilistic relationship between the plastic strain rate, the free energy required to overcome the obstacle ΔG, and the absolute temperature, T. Assuming that the probability of surmounting ΔG can be described by the Boltzmann distribution, the plastic strain rate caused by thermally activated dislocation motion can be given by

$$\dot{\varepsilon}_p = \dot{\varepsilon}_p^* \exp\left(\frac{-\Delta G}{k_B T}\right), \tag{3.1}$$

where k_B is Boltzmann's constant and $\dot{\varepsilon}_p^*$ is a material-specific constant.

3.1.3 Flow Stress Related to Dislocation Density

It is proposed in the Taylor model [5] that a dislocation's movement is arrested after travelling some average distance L and the average dislocation density reaches ρ. The flow stress required to continue dislocation movement is given by

$$\tau_f = \alpha \mu b \sqrt{\rho}, \tag{3.2}$$

where μ is the shear modulus, b is the magnitude of the Burgers vector, and ρ is the dislocation density. The parameter α is related to thermal activation. This equation is scaled by the Taylor factor, M, to describe a polycrystal. Taylor's equation (3.2) provides an average interaction strength between dislocations in a fairly simple form; this form does not take into account the arrangement of dislocations.

3.2 Work Hardening Phenomena

A plethora of work hardening theories [4], [36], [37] have been developed since Taylor proposed his model [5] in 1934, and it has been widely accepted since the 1950's that the rate of hardening is governed by two separate phenomena: an athermal hardening rate,

and dynamic recovery that is a temperature- and strain-rate-dependent decrease in the hardening rate [15]. Work hardening has been discussed in terms of four stages [38], [39] that are characterised by the dominant mechanism observed during working hardening.

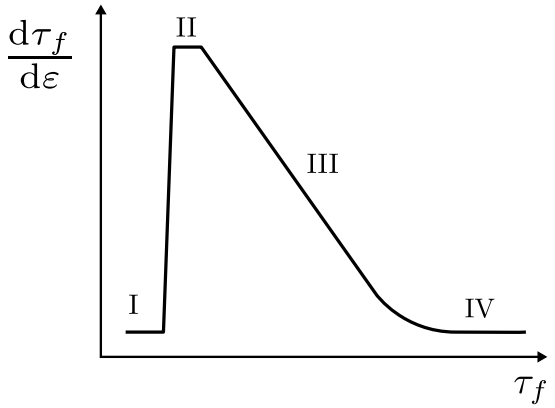

Figure 3.3: Four stages are evident when the hardening rate, which is calculated as a change in flow stress over change in strain, is examined against flow stress. Stage I and Stage II are classified by their near-constant linear hardening rates, Stage III is delineated by a linearly decreasing hardening rate, and Stage IV is marked by a nonlinear transition to near-constant hardening. [39]

Rollett et al. [39] delineate the work hardening stages with reference to the rate of hardening in a diagram like that shown in Figure 3.3. Although work hardening stages are not characterised solely by the hardening rate, diagrams like Figure 3.3 provide a means of identifying the stages present without the need to observe the microstructural phenomena throughout loading.

This work is centred around aluminium alloys in the finite strain regime, and so this section will discuss only the work hardening stages relevant to the work hardening behaviour expected from aluminium alloys. Aluminium has a very high stacking-fault energy[3] when compared to most FCC materials [13], which results in Stage III being the dominating stage due to its sensitivity to stacking-fault energy [39]–[41]. As Stage III limits Stage I and II to the extent that these stages are nearly unobservable, a review of these two stages is left to the appendices. A more comprehensive description of all four stages of work hardening can be found in [35], [39].

3.2.1 Stage III

Stage III is associated with a decreasing work hardening rate, termed *dynamic recovery*. Dynamic recovery should not be confused with static recovery; static recovery is driven by time-dependent kinetics and thermal activation and, as such, does not require external loading [42]. Dynamic recovery is only weakly time-dependent, and it is significantly dependent on temperature, the rate of deformation, and material characteristics. It is supposed that these dependencies are due to a dependence on stacking-fault energy [40],

[3]For an explanation of stacking-fault energy, see [34] pp. 10-11 and [35] pp. 30

[41]. While both forms of recovery lead to a decrease in the rate of work hardening, Kocks et al.[15] note that, despite difficulty in distinguishing time-dependent recovery from dynamic recovery from steady-state analysis, experimental observations demonstrate that straining a material at room temperature results in significantly more softening than in an identical material left to statically recover at the same temperature.

The breakdown of the principle of similitude[4], which forms a part of the forest [43], [44] and mesh [36], [45] theories[5], has been used to characterise the transition from Stage II to Stage III. Mecking and Kocks [18] depart from the study of dislocation arrangements and propose a theory based on mechanical tests to characterise Stage III. Athough the theory matches experimental data well in Stage III and IV, it is limited to the stages after Stage II.

3.2.2 Stage IV

Stage IV is characterised by *finite strain*, at which point the stress-strain curve illustrates a low hardening rate that tends to an asymptote in similar fashion to stage II for low strains [15]. Following Gil Sevillano's [46] work on finite strain in polycrystals in 1981, several theories [47]–[53] were proposed in an attempt to explain the microstructural mechanism behind finite strain.

3.3 Summary

In this chapter, several dislocation theory terms are defined, and the relevant stages of work hardening are briefly introduced. Dislocations are defined as one-dimensional line defects that can travel across a crystalline solid, and their motion leads to plastic strain. The rate of plastic strain can partially be determined by the probability of dislocations surmounting obstacles in their path through thermal activation. The flow stress required to continue dislocation movement is determined by Taylor's equation (3.2). Work hardening occurs at different rates over the course of loading, and these differing rates are described by stages. The third and fourth stage, dynamic recovery and finite strain, respectively, are of most relevance to this work. Dynamic recovery is significantly dependent on temperature, the rate of deformation, and material characteristics, while a comprehensive description of the finite-strain work hardening stage has not yet been agreed upon in the literature.

[4]See Appendix B.1
[5]See Appendix B.2

Chapter 4

Review of Selected Dislocation Density Evolution Equations

The descriptions of relevant work hardening phenomena outlined in Chapter 3 provide several requirements for a mechanistic model developed for the purpose of capturing dynamic recovery and finite strain behaviour in FCC metals. Although several mechanistic models that capture temperature-, strain-rate-, and material-dependence have been developed [6]–[13], the Kocks-Mecking model provides a simple constitutive equation for the evolution of the average dislocation density that captures the aforementioned dependencies.

A review of the uses of and adaptations to the Kocks-Mecking model is presented in this chapter. The foundation of the Kocks-Mecking model is presented in Section 4.1, followed by an examination of the model's extension to the finite strain regime in Section 4.3, and the equation's shortcomings are addressed in Section 4.4. The chapter is concluded with a summary in Section 4.5.

4.1 The Kocks-Mecking Model

The Kocks-Mecking model [15] is based on the observation that, when furnished with the average dislocation density, ρ, the Taylor equation (3.2) holds for FCC metals in most cases. It is supposed that the storage of forest dislocations is the dominant mechanism driving strain hardening, which results in isotropic hardening behaviour. The evolution of the density of forest dislocations is cast as two simultaneous, competing processes of dislocation storage and annihilation, which is given with respect to plastic strain by

$$\frac{\mathrm{d}\rho}{\mathrm{d}\varepsilon_p} = \frac{\mathrm{d}\rho}{\mathrm{d}\varepsilon_p}^{+} - \frac{\mathrm{d}\rho}{\mathrm{d}\varepsilon_p}^{-}, \tag{4.1}$$

where the first term pertains to dislocation storage, and the second term to dislocation annihilation. A summary of the parameters that follow in this section and their significance is provided in Table 4.1. Kocks and Mecking [15] present the dislocation density evolution in the form

$$\frac{\mathrm{d}\rho}{\mathrm{d}\varepsilon_p} = M\left[\frac{1}{bL} - k_2\rho\right], \tag{4.2}$$

where M is the Taylor factor, b is the magnitude of the Burgers vector, and L is the mean free path. L is assumed to be inversely proportional to $\sqrt{\rho}$, and therefore the model can also be expressed as

$$\frac{\mathrm{d}\rho}{\mathrm{d}\varepsilon_p} = M\left[k_1\sqrt{\rho} - k_2\rho\right], \tag{4.3}$$

where k_1 is a dislocation storage coefficient and k_2 is a dislocation annihilation coefficient. The determination of the k_1 and k_2 parameters is well-documented in [15]. Briefly, the storage coefficient can be formulated in terms of the ratio of the shear modulus at the current temperature to the shear modulus at 0 K, an activation constant, and the magnitude of the Burgers vector. The dislocation annihilation coefficient can be formulated by a more complex relationship between the aforementioned shear moduli, material parameters, and the probability of thermal activation, which is related to the plastic strain rate. k_2 is typically defined using a simplified relationship that provides an empirical relation between dynamic recovery, temperature, and strain rate through the equation

$$k_2 = k_{2o}\left[\frac{\dot{\varepsilon}_p}{\dot{\varepsilon}_{p0}}\right]^{-1/n}, \quad \text{where} \quad n = \frac{k_B T}{A}. \tag{4.4}$$

Here, k_{2o} is a constant, T is the temperature in Kelvin, k_B is the Boltzmann constant, and A is a material-specific constant related to relative stacking fault energy [15]. This formulation has been used successfully at small strains under the assumption that $\dot{\varepsilon}_p$, $\dot{\varepsilon}_{p0}$, and n are constant at a fixed strain rate and temperature [23], [27], [53], [54].

Table 4.1: Parameters and their significance in Equations (4.1)-(4.4)

μ	The shear modulus.
μ_0	The shear modulus at 0 K.
α	The thermal activation constant from the Taylor equation (3.2).
M	The Taylor factor.
b	The Burgers vector.
k_B	The Boltzmann constant.
T	The absolute temperature.
A	A material-specific constant related to relative stacking fault energy.
$\dot{\varepsilon}_{p0}$	A constant reference plastic strain rate $\approx 10^7 s^{-1}$ for FCC crystals.
k_1	A material parameter related to dislocation storage.
$k_2,\ k_{2o}$	A material parameters related to dislocation annihilation.

4.2 Application of the Kocks-Mecking Model

The Kocks-Mecking model is employed in several works [54]–[57] in which it is approximated that the magnitude of the rate of plastic deformation, $\dot{\varepsilon}_p$, remains constant and equivalent to the total strain rate throughout loading, and, therefore, that k_2 is constant in the power-law formulation (4.4).

Using the Taylor equation (3.2) scaled by M for a polycrystal for τ_f, the strain hardening rate, Θ, predicted by the Kocks-Mecking model is computed from

$$\Theta = \frac{\partial \tau_f}{\partial \varepsilon_p} = \frac{\partial \tau_f}{\partial \rho}\frac{\partial \rho}{\partial \varepsilon_p} \tag{4.5}$$

$$= \theta_0 - \beta_0 \tau_f, \tag{4.6}$$

where $\theta_0 = \alpha\mu b M^2 k_1/2$ and $\beta_0 = M k_2/2$. The Kocks-Mecking model thus yields a linear relationship between stress and the strain hardening rate. This model shows good agreement with experimental data at small strains [15], [22], [23], [54].

4.3 The Hariharan-Barlat Model

It is determined in Section 4.2 that the Kocks-Mecking dislocation density evolution equation assumes a linear relationship between stress and the strain hardening rate. This is contrary to hardening behaviour in the finite strain regime observed in experimental

data [19], [27], [58]. In an effort to capture nonlinear strain hardening at finite strains, Barlat et al.[28] introduced a second state variable, F. F is defined as a function of the mean free path, L,

$$F = \frac{1}{bL} = F_s + [F_y - F_s] \exp\left(\frac{\lambda_1 \varepsilon_p}{M}\right), \tag{4.7}$$

where F_y and F_s are the initial and saturated values of F, respectively, and λ_1 is a material parameter that controls the saturation rate. Hariharan et al. [27] modified this approach by reducing the model back down to a single state variable through formulating F in terms of dislocation density. Based on the assumption that $\sqrt{\rho}$ may be used as a characteristic length parameter, F may be expressed as

$$F = k\left[1 - \exp\left(-\psi\sqrt{\rho}\right)\right], \tag{4.8}$$

where k and ψ are material parameters. The modified Kocks-Mecking dislocation density evolution equation for finite strain can thus be formulated as

$$\frac{\mathrm{d}\rho}{\mathrm{d}\varepsilon_p} = M\left[k\left[1 - \exp\left(-\psi\sqrt{\rho}\right)\right] - k_2\rho\right] \tag{4.9}$$

from which the strain hardening rate is given by

$$\Theta = \frac{\partial \tau_f}{\partial \varepsilon_p} = \frac{\partial \tau_f}{\partial \rho}\frac{\partial \rho}{\partial \varepsilon_p} \tag{4.10}$$

$$= \frac{Mk\gamma_0^2}{2\tau_f}\left[1 - \exp\left(-\psi\frac{\tau_f}{\gamma_0}\right)\right] - \frac{Mk_2\tau_f}{2} \tag{4.11}$$

where $\gamma_0 = M\alpha\mu b$. This modification to the Kocks-Mecking equation successfully captures the nonlinearity observed at finite strains [27].

4.4 Limitations of the Kocks-Mecking and Hariharan-Barlat Models

Both the Kocks-Mecking and Hariharan-Barlat dislocation density evolution equations have been developed from monotonic uniaxial loading data; therefore, neither equation is explicitly formulated to capture dislocation density evolution in cyclical or multiaxial loading cases. Moreover, neither equation makes explicit provision for other microstructural features, such as precipitates. This section briefly details two of the most prominent shortcomings of these dislocation density evolution equations, namely the omission of precipitation hardening in Section 4.4.1, and the Bauschinger effect in Section 4.4.2.

4.4.1 Precipitation Hardening

Precipitation hardening increases the yield strength of a material by including precipitates in the microstructure of the material that hinder dislocation motion. The Kocks-Mecking dislocation density evolution equation has been extended in several works [24], [26], [58], [59] to reflect the presence of precipitates by accounting for the storage of Orowan loops around these obstacles. Generally, this is achieved in one of two fashions. In the simplest fashion, a new term that is inversely proportional to the particle spacing in the glide plane, l, is introduced, resulting in

$$\frac{\mathrm{d}\rho}{\mathrm{d}\varepsilon_p} = M\left[k_1\sqrt{\rho} + \frac{1}{bl} - k_2\rho\right], \tag{4.12}$$

where l is dependent on the precipitate size and volume fraction [59], [60]. In a more complex fashion, the formulation of k_2 may be extended to include the effect of precipitate size and volume fraction on the dynamic recovery rate, resulting in the formulation like that posited by [24]

$$k_2 = k_{2o}\exp\left(-\frac{\varphi}{l\sqrt{\rho}}\right) + k_2^p\left[1 - \exp\left(-\frac{\varphi}{l\sqrt{\rho}}\right)\right], \tag{4.13}$$

where the k_{2o}-term is associated with annihilation process that concerns only two dislocations, the k_2^p-term is associated with the annihilation processes that concern dislocation pairs and a dislocation loop stored around non-shearable precipitates, and φ is an efficiency factor for loop storage [24], [58]. These modifications to the Kocks-Mecking model address strain hardening under monotonic loading, and do not consider the effect of precipitates in reversed loading.

4.4.2 The Bauschinger Effect

The effect of precipitates on work hardening behaviour is notable during reversed loading. During monotonic loading, the work hardening rate is affected by stress contributions from precipitates, solutes, and the forest dislocation density; however, upon reversing the loading path, only precipitates contribute to the work hardening rate [22]. The Bauschinger effect describes the decreasing yield stress in one direction as a result of prior plastic deformation in the opposite direction, and it is addressed in a continuum mechanics framework by a phenomenological kinematic hardening rule in a tensorial framework capable of capturing multiaxial hardening. Mechanistically-motivated kinematic hardening rules posed in a metallurgical framework, however, are generally limited to a scalar formulation [22], [25]. While these microstructurally-based rules provide more insight into microstructural phenomena, they are not suitable for multiaxial loading cases without some adjustment. Bouaziz et al. [61] bridge the gap between microstructural and

continuum mechanics approaches through the combination of a scalar stress that describes isotropic hardening, and a tensorial stress that accounts for kinematic hardening.

4.5 Summary

The Kocks-Mecking model for the evolution of average dislocation density has been used successfully to model dynamic recovery at small strains [15], and it has been extended to account for nonlinear work hardening rates in the finite strain regime by Hariharan and Barlat [27]. Typically, the plastic strain rate is approximated as constant throughout loading, and, therefore, the dislocation annihilation parameter in both equations, k_2, may be treated as a constant value. Neither the Kocks-Mecking nor Hariharan-Barlat model captures the effect of precipitate-induced hardening or the Bauschinger effect.

Chapter 5

Relevant Constitutive Frameworks

The fundamental principles of continuum thermomechanics alone do not provide a sufficient set of equations to describe the behaviour of a body. The behaviour of a body is dictated by both the laws of thermodynamics and the material of which the body is composed; therefore, an additional constitutive law is required to create well-posed problems. Broadly, a constitutive equation maps the values of one or more other fields, ζ_n, to a field variable, Φ,

$$\Phi\left(\boldsymbol{X}, t\right) = \hat{\Phi}(\zeta_n\left(\boldsymbol{X}, t\right), \boldsymbol{X}). \tag{5.1}$$

The hat notation denotes $\hat{\Phi}$ as a constitutive response function that maps the fields ζ_n to the field variable Φ. This is succinctly represented henceforth as

$$\Phi = \hat{\Phi}(\zeta), \tag{5.2}$$

which is not intended to imply an independence from position.

In this chapter, the elastoplasticity constitutive framework upon which this work is built is introduced. The hyperelasticity model that governs elastic behaviour is presented at the beginning of the chapter, followed by an overview of an isothermal, finite-strain elastoplasticity constitutive model.

5.1 Neo-Hookean Hyperelasticity

An isotropic, compressible Neo-Hookean model [62] is used to describe elastic behaviour in this work. For simplicity, the hyperelastic constitutive equations introduced in this section are formulated as though only elastic strain occurs, which implies that the kinematic quantities used in this section correspond to purely elastic deformation. In Section 5.2, the decomposition of kinematic quantities into elastic and plastic parts is introduced in the context of an elastoplasticity constitutive model; in an elastoplastic framework, only the elastic parts apply to hyperelastic constitutive equations.

Briefly, hyperelastic constitutive laws [33]:

(i) define strain energy Ψ entirely in terms of the right Cauchy-Green tensor $\boldsymbol{C}$, a frame-indifferent quantity [30], [32], [63],

$$\Psi = \hat{\Psi}(\boldsymbol{C}), \tag{5.3}$$

(ii) do not depend upon the state of all points in the domain, and thus describe only local action,

(iii) consider only the current state of a particle, and are independent of the loading history,

(iv) and only describe material behaviour in which there is no dissipation, such that

$$0 = \mathcal{D}(\mathcal{P}) = \boldsymbol{S} : \dot{\boldsymbol{E}} - \dot{\Psi} = \left[\boldsymbol{S} - \frac{\partial \Psi}{\partial \boldsymbol{E}}\right] : \dot{\boldsymbol{E}}. \tag{5.4}$$

Thus, according to the Coleman-Noll procedure [2], the second Piola-Kirchhoff stress must be equal to the derivative of the strain energy function,

$$\boldsymbol{S} = 2\frac{\partial \hat{\Psi}(\boldsymbol{C})}{\partial \boldsymbol{C}} \Rightarrow \hat{\boldsymbol{S}}(\boldsymbol{C}), \tag{5.5}$$

to ensure thermodynamic admissibility. This will be discussed in more detail in Section 5.2.4.

A Neo-Hookean material may be described by the strain energy function

$$\hat{\Psi}(I_1, I_3) = \frac{1}{4}\Big[2\mu\left[I_1 - 3 - \ln(I_3)\right] + \lambda_L\left[I_3 - 1 - \ln(I_3)\right]\Big], \tag{5.6}$$

where λ_L and μ are the Lamé constants, and I_1 and I_3 are the first and third invariants of the left Cauchy-Green tensor $\boldsymbol{B}$ or the right Cauchy-Green tensor $\boldsymbol{C}$ [62] .

5.1.1 The Second Piola-Kirchhoff Stress

A hyperelastic strain energy function may be postulated in terms of the isotropic invariants of $\boldsymbol{C}$ [33], where

$$I_1 = \operatorname{tr}(\boldsymbol{C}), \quad I_2 = \frac{1}{2}\Big[\operatorname{tr}(\boldsymbol{C})^2 - \operatorname{tr}\left(\boldsymbol{C}^2\right)\Big], \quad I_3 = \det(\boldsymbol{C}) = J^2. \tag{5.7}$$

This allows the second Piola-Kirchhoff stress to be expressed in terms of the isotropic invariants of $\boldsymbol{C}$ as follows

$$\boldsymbol{S} = 2\sum_{i=1}^{3} \frac{\partial \Psi}{\partial I_i} \frac{\partial I_i}{\partial \boldsymbol{C}}, \tag{5.8}$$

where

$$\frac{\partial I_1}{\partial \boldsymbol{C}} = \boldsymbol{I}, \quad \frac{\partial I_2}{\partial \boldsymbol{C}} = 2\boldsymbol{C}, \quad \frac{\partial I_3}{\partial \boldsymbol{C}} = J^2 \boldsymbol{C}^{-1}. \tag{5.9}$$

Thus, the second Piola-Kirchhoff stress for the Neo-Hookean model in Equation (5.6) is given by

$$\boldsymbol{S} = \mu \boldsymbol{I} + \frac{1}{2}\Big[\lambda_L \det(\boldsymbol{C}) - [\lambda_L + 2\mu]\Big]\boldsymbol{C}^{-1}. \tag{5.10}$$

5.1.2 The Kirchhoff Stress

The Kirchhoff stress is given by

$$\boldsymbol{\tau} = \boldsymbol{F}\boldsymbol{S}\boldsymbol{F}^T = 2\frac{\partial \Psi}{\partial \boldsymbol{B}}\boldsymbol{B} = 2\sum_{i=1}^{3} \frac{\partial \Psi}{\partial I_i}\boldsymbol{A}_i, \tag{5.11}$$

where

$$\boldsymbol{A}_i = \boldsymbol{F}\frac{\partial I_i}{\partial \boldsymbol{C}}\boldsymbol{F}^T. \tag{5.12}$$

and

$$\boldsymbol{A}_1 = \boldsymbol{B}, \quad \boldsymbol{A}_2 = 2\boldsymbol{B}^2, \quad \boldsymbol{A}_3 = \det(\boldsymbol{B})\,\boldsymbol{I}, \tag{5.13}$$

which yields

$$\boldsymbol{\tau} = \mu \boldsymbol{B} + \frac{1}{2}\left[\lambda_L I_3(\boldsymbol{B}) - [\lambda_L + 2\mu]\right]\boldsymbol{I} \tag{5.14}$$

for the Neo-Hookean model in Equation (5.6). The isochoric part of Kirchhoff stress is

$$\bar{\boldsymbol{\tau}} = \boldsymbol{\tau} - \frac{1}{3}\boldsymbol{I}\,\mathrm{tr}(\boldsymbol{\tau}). \tag{5.15}$$

5.2 Isothermal Finite-Strain Elastoplasticity

In this section, the continuum mechanics framework for isothermal, finite-strain elastoplasticity is presented. This explanation is brief, and draws from more thorough explanations in [29], [30], [32].

5.2.1 Kinematics

It is supposed that the distortion experienced by a crystal lattice can be decomposed into elastic and plastic parts [29]. In finite-strain plasticity theory, this decomposition is reflected as a multiplicative split of the deformation gradient, known as the Lee decomposition [1]:

$$\boldsymbol{F} = \boldsymbol{F}_e \boldsymbol{F}_p. \tag{5.16}$$

Here, $\bullet_p$ denotes the plastic part and $\bullet_e$ denotes the elastic part. Plastic distortion is understood to be local deformation due to the movement of dislocations [34], [35], which is discussed in Chapter 3; this flow is assumed to be isochoric, and therefore

$$J_p := \det\left(\boldsymbol{F}_p\right) = 1. \tag{5.17}$$

The elastic and plastic components of the standard kinematic quantities are defined as follows:
the right Cauchy-Green tensor,

$$\boldsymbol{C} := \boldsymbol{F}^T \boldsymbol{F}, \quad \boldsymbol{C}_e := \boldsymbol{F}_e^T \boldsymbol{F}_e, \quad \boldsymbol{C}_p := \boldsymbol{F}_p^T \boldsymbol{F}_p, \tag{5.18}$$

the Green-Lagrange strain,

$$\boldsymbol{E} := \frac{1}{2}\left[\boldsymbol{C} - \boldsymbol{I}\right], \quad \boldsymbol{E}_e := \frac{1}{2}\left[\boldsymbol{C}_e - \boldsymbol{I}\right], \quad \boldsymbol{E}_p := \frac{1}{2}\left[\boldsymbol{C}_p - \boldsymbol{I}\right], \tag{5.19}$$

and consequently the Green-Lagrange strain rate,

$$\dot{\boldsymbol{E}} := \frac{1}{2}\left[\dot{\boldsymbol{F}}^T \boldsymbol{F} + \boldsymbol{F}^T \dot{\boldsymbol{F}}\right], \quad \dot{\boldsymbol{E}}_e := \frac{1}{2}\left[\dot{\boldsymbol{F}}_e^T \boldsymbol{F}_e + \boldsymbol{F}_e^T \dot{\boldsymbol{F}}_e\right], \quad \dot{\boldsymbol{E}}_p := \frac{1}{2}\left[\dot{\boldsymbol{F}}_p^T \boldsymbol{F}_p + \boldsymbol{F}_p^T \dot{\boldsymbol{F}}_p\right]. \tag{5.20}$$

The velocity gradient

$$\boldsymbol{L} := \operatorname{grad}\left(\dot{\phi}\right) = \dot{\boldsymbol{F}} \boldsymbol{F}^{-1} \tag{5.21}$$

is related to elastic and plastic deformation by the Lee decomposition

$$\boldsymbol{L} = \left[\dot{\boldsymbol{F}}_e \boldsymbol{F}_p + \boldsymbol{F}_e \dot{\boldsymbol{F}}_p\right]\left[\boldsymbol{F}_p^{-1} \boldsymbol{F}_e^{-1}\right], \tag{5.22}$$

$$= \dot{\boldsymbol{F}}_e \boldsymbol{F}_e^{-1} + \boldsymbol{F}_e \left[\dot{\boldsymbol{F}}_p \boldsymbol{F}_p^{-1}\right] \boldsymbol{F}_e^{-1}. \tag{5.23}$$

and is thus similarly decomposed into elastic and plastic distortion-rate tensors

$$\boldsymbol{L}_e = \dot{\boldsymbol{F}}_e \boldsymbol{F}_e^{-1}, \tag{5.24}$$

and

$$\boldsymbol{L}_p = \dot{\boldsymbol{F}}_p \boldsymbol{F}_p^{-1}. \tag{5.25}$$

From Equations (5.23) and (5.24), one arrives at the following decomposition for the velocity gradient:

$$\boldsymbol{L} = \boldsymbol{L}_e + \boldsymbol{F}_e \boldsymbol{L}_p \boldsymbol{F}_e^{-1}. \tag{5.26}$$

The rate of the plastic deformation gradient, also know as the plastic evolution,

$$\dot{\boldsymbol{F}}_p = \boldsymbol{L}_p \boldsymbol{F}_p, \tag{5.27}$$

is governed by a constitutive equation for the plastic velocity gradient,

$$\boldsymbol{L}_p = \hat{\boldsymbol{L}}_p \left(\boldsymbol{F}, \dot{\boldsymbol{F}}, \boldsymbol{F}_p, \boldsymbol{\xi}, \dots \right), \tag{5.28}$$

where $\boldsymbol{\xi}$ represents one or more internal variables. The rate of deformation tensor is defined to be

$$\boldsymbol{D} := \operatorname{sym}(\boldsymbol{L}) = \boldsymbol{F}^{-T} \dot{\boldsymbol{E}} \boldsymbol{F}^{-1}, \tag{5.29}$$

and the rate of elastic and plastic deformations are defined as

$$\boldsymbol{D}_e := \operatorname{sym}(\boldsymbol{L}_e) = \boldsymbol{F}_e^{-T} \dot{\boldsymbol{E}}_e \boldsymbol{F}_e^{-1} \tag{5.30}$$

and

$$\boldsymbol{D}_p := \operatorname{sym}(\boldsymbol{L}_p) = \boldsymbol{F}_p^{-T} \dot{\boldsymbol{E}}_p \boldsymbol{F}_p^{-1}, \tag{5.31}$$

accordingly. As it is assumed that plastic deformation is isochoric, the plastic velocity gradient and hence the rate of plastic deformation are deviatoric; that is

$$\operatorname{tr}(\boldsymbol{L}_p) = 0, \tag{5.32}$$

and

$$\operatorname{tr}(\boldsymbol{D}_p) = 0. \tag{5.33}$$

It is further assumed that plastic spin vanishes,

$$\boldsymbol{W}_p := \operatorname{skw}(\boldsymbol{L}_p) = \boldsymbol{0}, \tag{5.34}$$

and this assumption of plastic irrotationality results in

$$\boldsymbol{D}_p = \boldsymbol{L}_p. \tag{5.35}$$

Equations (5.19) and (5.30) are used to derive a more useful expression of the strain rate:

$$\dot{\boldsymbol{E}} = \boldsymbol{F}^T \boldsymbol{D}_e \boldsymbol{F} + \operatorname{sym}\left(\boldsymbol{C} \boldsymbol{F}_p^{-1} \dot{\boldsymbol{F}}_p \right). \tag{5.36}$$

5.2.2 The Elastic Second Piola-Kirchhoff Stress

Consider the elastic stress power, following from Section 2.4.1:

$$\boldsymbol{\tau} : \boldsymbol{D}_e = \boldsymbol{\tau} : \boldsymbol{L}_e. \tag{5.37}$$

It is convenient to express the elastic stress power in terms of the elastic strain rate, which necessitates a stress quantity that is work-conjugate to $\dot{\boldsymbol{E}}_e$,

$$\begin{aligned} \boldsymbol{\tau} : \boldsymbol{L}_e &= \boldsymbol{\tau} : \dot{\boldsymbol{F}}_e \boldsymbol{F}_e^{-1}, && (5.38)\\ &= \boldsymbol{F}_e^{-1}\boldsymbol{\tau}\boldsymbol{F}_e^{-T} : \boldsymbol{F}_e^T \dot{\boldsymbol{F}}_e, && (5.39)\\ &= \boldsymbol{S}_e : \dot{\boldsymbol{E}}_e. && (5.40) \end{aligned}$$

Thus, the elastic second Piola-Kirchhoff stress is defined to be

$$\boldsymbol{S}_e := \boldsymbol{F}_e^{-1}\boldsymbol{\tau}\boldsymbol{F}_e^{-T} = \boldsymbol{F}_p \boldsymbol{S} \boldsymbol{F}_p^T. \tag{5.41}$$

5.2.3 The Mandel Stress

Consider the reduced dissipation inequality in Equation (2.66) in Section 2.4 in terms of the second Piola-Kirchhoff stress,

$$\mathcal{D} = \boldsymbol{S} : \dot{\boldsymbol{E}} - \dot{\Psi} \geq 0. \tag{5.42}$$

The reduced dissipation inequality is rearranged so as to be expressed in more convenient terms by inserting the strain rate expression in Equation (5.36)

$$\begin{aligned} \mathcal{D} &= \boldsymbol{S} : \left[\boldsymbol{F}^T \boldsymbol{D}_e \boldsymbol{F} + \operatorname{sym}\left(\boldsymbol{C}\boldsymbol{F}_p^{-1}\dot{\boldsymbol{F}}_p \right) \right] - \dot{\Psi}, && (5.43)\\ &= \boldsymbol{\tau} : \boldsymbol{D}_e + \boldsymbol{S} : \boldsymbol{F}^T\boldsymbol{F}\boldsymbol{F}_p^{-1}\dot{\boldsymbol{F}}_p - \dot{\Psi}, && (5.44)\\ &= \boldsymbol{S}_e : \dot{\boldsymbol{E}}_e + \boldsymbol{F}_e^T\boldsymbol{\tau}\boldsymbol{F}_e^{-T} : \boldsymbol{L}_p - \dot{\Psi}. && (5.45) \end{aligned}$$

Here, it is useful to define a new tensor,

$$\boldsymbol{M}_e := \boldsymbol{F}_e^T \boldsymbol{\tau} \boldsymbol{F}_e^{-T}. \tag{5.46}$$

which is known as the Mandel stress. Thus, the following form of the reduced dissipation inequality results:

$$\mathcal{D} = \boldsymbol{S}_e : \dot{\boldsymbol{E}}_e + \boldsymbol{M}_e : \boldsymbol{D}_p - \dot{\Psi} \geq 0. \tag{5.47}$$

5.2.4 The Reduced Dissipation Inequality

For a general separable constitutive theory, the Helmholtz free energy is postulated as a state function of the elastic Green-Lagrange strain [29], [64]. The time derivative of Helmholtz free energy is computed via the chain rule:

$$\dot{\Psi} = \frac{\partial \hat{\Psi}(\boldsymbol{E}_e)}{\partial \boldsymbol{E}_e} : \dot{\boldsymbol{E}}_e. \tag{5.48}$$

By combining Equation (5.47) with Equation (5.48), the dissipation inequality (5.47) can be rewritten

$$\mathcal{D} = \left[\boldsymbol{S}_e - \frac{\partial \hat{\Psi}(\boldsymbol{E}_e)}{\partial \boldsymbol{E}_e} \right] : \dot{\boldsymbol{E}}_e + \boldsymbol{M}_e : \boldsymbol{D}_p \geq 0. \tag{5.49}$$

For Equation (5.49) to hold for all mechanical processes, that is, for all values of $\dot{\boldsymbol{E}}_e$ and its gradients, the cofactor of $\dot{\boldsymbol{E}}_e$ must be equal to zero, and the second term must be non-negative. Since $\boldsymbol{D}_p$ is deviatoric, $\boldsymbol{M}_e : \boldsymbol{D}_p = \bar{\boldsymbol{M}}_e : \boldsymbol{D}_p$ [29]. Therefore, according to the Coleman-Noll procedure [2], to ensure that every constitutive process satisfies the free-energy imbalance, the following conditions are necessary:

(i) The elastic second Piola-Kirchhoff stress is determined by the free energy through the relation

$$\boldsymbol{S}_e = \frac{\partial \hat{\Psi}(\boldsymbol{E}_e)}{\partial \boldsymbol{E}_e}, \tag{5.50}$$

(ii) and the deviatoric Mandel stress satisfies the reduced dissipation inequality,

$$0 \leq \bar{\boldsymbol{M}}_e : \boldsymbol{D}_p. \tag{5.51}$$

5.2.5 The Principle of Maximum Plastic Dissipation

It is typically assumed that field variables evolve such that dissipation is maximised [29]. For dissipation to be maximised, the deviatoric Mandel stress must be in same direction as the plastic rate of deformation, that is:

$$\frac{\bar{\boldsymbol{M}}_e}{\|\bar{\boldsymbol{M}}_e\|} = \frac{\boldsymbol{D}_p}{\|\boldsymbol{D}_p\|}. \tag{5.52}$$

Therefore, it is useful to define the tensor

$$\boldsymbol{N} := \frac{\boldsymbol{D}_p}{\|\boldsymbol{D}_p\|}. \tag{5.53}$$

so that $\boldsymbol{D}_p$ may be written in terms of a scalar and a tensorial part:

$$\boldsymbol{D}_p = \dot{\lambda}\boldsymbol{N}. \tag{5.54}$$

5.2.6 Rate-Dependent Flow of an Isotropic Elastoplastic Material

A complete description of rate-dependent, finite-strain elastoplastic flow of an isotropic material requires several essential equations. The constitutive rule is given by the plastic velocity gradient

$$\hat{\boldsymbol{L}}_p\left(\boldsymbol{F}, \boldsymbol{F}_p, \boldsymbol{\xi}\right) = \dot{\lambda}\boldsymbol{N}. \tag{5.55}$$

Since

$$\frac{\bar{\boldsymbol{M}}_e}{\|\bar{\boldsymbol{M}}_e\|} = \boldsymbol{N}, \tag{5.56}$$

$$\frac{\boldsymbol{F}_e^T\bar{\boldsymbol{\tau}}\boldsymbol{F}_e^{-T}}{\|\boldsymbol{F}_e^T\bar{\boldsymbol{\tau}}\boldsymbol{F}_e^{-T}\|} = \boldsymbol{N}, \tag{5.57}$$

the direction of plastic flow is found from

$$\boldsymbol{N} = \boldsymbol{F}_e^T\frac{\bar{\boldsymbol{\tau}}}{\|\bar{\boldsymbol{\tau}}\|}\boldsymbol{F}_e^{-T}, \tag{5.58}$$

which motivates the definition of

$$\boldsymbol{T} := \frac{\bar{\boldsymbol{\tau}}}{\|\bar{\boldsymbol{\tau}}\|}. \tag{5.59}$$

The rate of plastic deformation is described by the power-law rate-sensitivity function

$$\dot{\lambda} = \frac{1}{\eta}\left[\frac{\tau_y}{\hat{\tau}_f(\boldsymbol{\xi})}\right]^{1/m}, \tag{5.60}$$

where η and m are material parameters, τ_y is the equivalent scalar stress computed from

$$\tau_y = \sqrt{\frac{3}{2}}\|\bar{\boldsymbol{\tau}}\|, \tag{5.61}$$

and the flow stress τ_f is a function of the internal state variables that describe hardening, $\boldsymbol{\xi}$. The evolution of the internal state variables is described by a hardening rule,

$$\dot{\boldsymbol{\xi}} = \hat{\dot{\boldsymbol{\xi}}}\left(\boldsymbol{F}, \boldsymbol{F}_p, \boldsymbol{\xi}\right). \tag{5.62}$$

Thus, with the selection of an appropriate hardening variable, a flow stress equation, and a strain energy function from which $\boldsymbol{\tau}$ is derived, an initial value problem may be posed. Typically, accumulated plastic strain is employed as a hardening variable, and, therefore, will be used in the initial value problem that follows [29].

The Initial Value Problem

Using accumulated plastic strain as the internal state variable, $\boldsymbol{\xi} \Rightarrow e_p$, and given a defined loading path $\boldsymbol{F}(t)$ at a material point, the finite-strain, elastoplastic initial value problem is posed as follows:

Find the plastic deformation gradient, $\boldsymbol{F}_p$, and the accumulated plastic strain, e_p, defined on the domain $t = [t_0, t_1]$ such that the following equations are satisfied

$$\dot{\boldsymbol{F}}_p = \boldsymbol{L}_p \boldsymbol{F}_p, \tag{5.63}$$

$$\dot{e}_p = \dot{\lambda} \tag{5.64}$$

given

$$\boldsymbol{F}_p\,(t_0) = \boldsymbol{F}_{p\,0}, \tag{5.65}$$

$$e_p\,(t_0) = e_{p\,0}, \tag{5.66}$$

where

$$\boldsymbol{L}_p = \dot{\lambda} \boldsymbol{N}, \tag{5.67}$$

$$\dot{\lambda} = \frac{1}{\eta} \left[\frac{\tau_y}{\hat{\tau}_f(\boldsymbol{e}_p)} \right]^{1/m} \tag{5.68}$$

$$\boldsymbol{N} = \boldsymbol{F}_e^{-T} \boldsymbol{T} \boldsymbol{F}_e^{T}, \tag{5.69}$$

$$\boldsymbol{T} = \frac{\bar{\boldsymbol{\tau}}}{\|\bar{\boldsymbol{\tau}}\|}, \tag{5.70}$$

$$\boldsymbol{F}_e = \boldsymbol{F} \boldsymbol{F}_p^{-1}, \tag{5.71}$$

$$\tau_y = \sqrt{\frac{3}{2}} \|\bar{\boldsymbol{\tau}}\|, \tag{5.72}$$

and

$$\bar{\boldsymbol{\tau}} = \boldsymbol{\tau} - \frac{1}{3} \boldsymbol{I}\, \mathrm{tr}\,(\boldsymbol{\tau})\,. \tag{5.73}$$

5.3 Summary of Key Equations

The key equations presented in this chapter are summarised in what follows.

Hyperelasticity

Elastic Kirchhoff stress: $$\boldsymbol{\tau} = \mu \boldsymbol{B} + \frac{1}{2}\left[\lambda_L I_3\left(\boldsymbol{B}\right) - \left[\lambda_L + 2\mu\right]\right]\boldsymbol{I} \tag{5.74}$$

Elastic second Piola-Kirchhoff stress: $$\boldsymbol{S}_{=}\mu \boldsymbol{I} + \frac{1}{2}\left[\lambda_L \det\left(\boldsymbol{C}\right) - \left[\lambda_L + 2\mu\right]\right]\boldsymbol{C}_e^{-1} \tag{5.75}$$

Finite strain elastoplasticity

Kinematics:

Lee decomposition: $$\boldsymbol{F} = \boldsymbol{F}_e \boldsymbol{F}_p \tag{5.76}$$

Elastic right Cauchy-Green tensor: $$\boldsymbol{C}_e = \boldsymbol{F}_e^T \boldsymbol{F}_e \tag{5.77}$$

Right Cauchy-Green tensor: $$\boldsymbol{C} = \boldsymbol{F}_p^T \boldsymbol{C}_e \boldsymbol{F}_p \tag{5.78}$$

Rate of deformation tensor: $$\boldsymbol{D} = \operatorname{sym}\left(\boldsymbol{L}\right) = \operatorname{sym}\left(\dot{\boldsymbol{F}}\boldsymbol{F}^{-1}\right) \tag{5.79}$$

Elastic rate of deformation tensor: $$\boldsymbol{D}_e = \operatorname{sym}\left(\boldsymbol{L}_e\right) = \operatorname{sym}\left(\dot{\boldsymbol{F}}_e\boldsymbol{F}_e^{-1}\right) \tag{5.80}$$

Plastic rate of deformation tensor: $$\boldsymbol{D}_p = \operatorname{sym}\left(\boldsymbol{L}_p\right) = \operatorname{sym}\left(\dot{\boldsymbol{F}}_p\boldsymbol{F}_p^{-1}\right) \tag{5.81}$$

Finite strain plasticity constitutive essentials:

Elastic strain energy: $$\Psi = \hat{\Psi}(\boldsymbol{C}_e) \tag{5.82}$$

Elastic second Piola-Kirchhoff stress: $$\boldsymbol{S}_e = 2\frac{\partial \Psi}{\partial \boldsymbol{C}_e} \tag{5.83}$$

Second Piola-Kirchhoff stress: $$\boldsymbol{S} = \boldsymbol{F}_p^{-1}\boldsymbol{S}_e\boldsymbol{F}_p^{-T} \tag{5.84}$$

Kirchhoff stress: $$\boldsymbol{\tau} = \boldsymbol{F}_e\boldsymbol{S}_e\boldsymbol{F}_e^T \tag{5.85}$$

Elastic Mandel stress: $$\boldsymbol{M}_e = \boldsymbol{F}_e^T\bar{\boldsymbol{\tau}}\boldsymbol{F}_e^{-T} \tag{5.86}$$

Evolution of plastic gradient: $$\dot{\boldsymbol{F}}_p = \boldsymbol{L}_p\boldsymbol{F}_p \tag{5.87}$$

Plastic flow rule: $$\boldsymbol{L}_p = \hat{\boldsymbol{L}}_p\left(\boldsymbol{F}, \dot{\boldsymbol{F}}, \boldsymbol{F}_p, \boldsymbol{\xi}, \dots\right) \tag{5.88}$$

Evolution of internal variables: $$\dot{\boldsymbol{\xi}} = \hat{\dot{\boldsymbol{\xi}}} \tag{5.89}$$

Implication of the reduced dissipation inequality:

$$0 \leq \mathcal{D} = \left[\boldsymbol{S}_e - \frac{1}{2}\frac{\partial \Psi}{\partial \boldsymbol{E}_e}\right] : \dot{\boldsymbol{E}}_e + \boldsymbol{M}_e : \boldsymbol{D}_p \tag{5.90}$$

Coleman-Noll procedure:

$$0 \leq \mathcal{D} = \boldsymbol{M}_e : \boldsymbol{D}_p \tag{5.91}$$

$$\boldsymbol{S}_e = \frac{\partial \hat{\Psi}(\boldsymbol{E}_e)}{\partial \boldsymbol{E}_e} \tag{5.92}$$

That is, for a constitutive model to be thermodynamically admissible, the constitutive Equations (5.88) and (5.89) must be chosen such that Equation (5.91) is satisfied for all processes.

Chapter 6

Development and Implementation of a Constitutive Model for Dislocation Density-Based, Finite-Strain, Rate-Dependent Elastoplasticity

The essential equations for isothermal, rate-dependent, finite-strain elastoplasticity are presented in Chapter 5, following which an initial value problem is posed that makes use of accumulated plastic strain as an internal state variable. In this work, accumulated plastic strain is replaced by average dislocation density as the internal state variable that governs the rate of work hardening. It has long been accepted that a relationship exists between the flow stress required to continue plastic deformation and the average dislocation density [5], [15]. It is, therefore, appropriate to cast average dislocation density as the internal state variable that governs hardening.

In this chapter, a new initial value problem is formulated from the Kocks-Mecking and Hariharan-Barlat dislocation density evolution models outlined in Chapter 4. This chapter is presented in two parts: the first part concerns the development of the elastoplasticity model, and the second part concerns a preliminary investigation of its behaviour in a simple numerical implementation. The new initial value problem upon which this work is predicated is presented in Section 6.1, and the numerical implementation of the constitutive model follows in Section 6.2 in which the behaviour of the constitutive model is elucidated by examining a single material point undergoing deformation.

6.1 A Revised Initial Value Problem

Using average dislocation density as the internal state variable that describes hardening, and given a defined deformation gradient progression $\boldsymbol{F}(t)$ at a material point, the initial

value problem is posed as follows:

Find the plastic deformation gradient, $\boldsymbol{F}_p(t)$, and the average dislocation density, $\rho(t)$, defined on the domain $t = [t_0, t_1]$ such that the following equations are satisfied

$$\dot{\boldsymbol{F}}_p = \boldsymbol{L}_p \boldsymbol{F}_p, \tag{6.1}$$

$$\dot{\rho} = \hat{\dot{\rho}}\left(\boldsymbol{F}, \boldsymbol{F}_p, \rho\right) \tag{6.2}$$

where the dislocation density evolution equation, $\dot{\rho}$, is given by either Equation (4.3) or Equation (4.9), and given the initial conditions

$$\boldsymbol{F}_p\left(t_0\right) = \boldsymbol{F}_{p\,0} \tag{6.3}$$

$$\text{and} \quad \rho\left(t_0\right) = \rho_0, \tag{6.4}$$

where

$$\boldsymbol{L}_p = \dot{\lambda}\boldsymbol{N}, \tag{6.5}$$

$$\dot{\lambda} = \frac{1}{\eta}\left[\frac{\tau_y}{\hat{\tau}_f(\rho)}\right]^{1/m}, \tag{6.6}$$

$$\boldsymbol{N} = \boldsymbol{F}_e^T \boldsymbol{T} \boldsymbol{F}_e^{-T}, \tag{6.7}$$

$$\boldsymbol{T} = \frac{\bar{\boldsymbol{\tau}}}{\|\bar{\boldsymbol{\tau}}\|}, \tag{6.8}$$

$$\boldsymbol{F}_e = \boldsymbol{F}\boldsymbol{F}_p^{-1}, \tag{6.9}$$

$$\tau_y = \sqrt{\frac{3}{2}}\|\bar{\boldsymbol{\tau}}\|, \tag{6.10}$$

and

$$\bar{\boldsymbol{\tau}} = \boldsymbol{\tau} - \frac{1}{3}\boldsymbol{I}\,\mathrm{tr}\left(\boldsymbol{\tau}\right). \tag{6.11}$$

In this constitutive model, the flow stress is given by the Taylor equation presented in Section 3.1.3,

$$\tau_f = M\alpha\mu b\sqrt{\rho}. \tag{6.12}$$

6.2 Temporal Discretization

Consider the temporal discretization

$$0 = t^{(0)} < t^{(1)} < t^{(2)} ... < t^{(\mathrm{n})} < t^{(\mathrm{n}+1)}, \tag{6.13}$$

where each time increment is defined by

$$\Delta t := t^{(\mathrm{n}+1)} - t^{(\mathrm{n})}. \tag{6.14}$$

Throughout the remainder of this work, the value of a quantity at a given time step is indicated by the quantity with the time step in parentheses as superscript: $\bullet^{(\mathrm{n})}$. The parentheses indicate that this should not be mistaken as the quantity raised to the power n. To solve the initial value problem posed in this chapter, an implicit-explicit approach is taken, where some equations are solved explicitly and others, implicitly. Average dislocation density and the magnitude of the rate of plastic deformation are solved implicitly; that is, Equations (6.2) and (6.6) are satisfied at $t^{(\mathrm{n}+1)}$. However, the plastic direction given by Equation (6.7) is satisfied at $t^{(\mathrm{n})}$ and is, therefore, solved explicitly. This approach is outlined in Section 6.2.1, followed by the directional derivatives and partial differential equations required for the use of the nonlinear solver described in Section 6.2.2.

6.2.1 Implicit-Explicit Approach

An implicit-explicit approach is used to account for the significant stiffness of the dislocation density evolution equations compared to the plastic direction equation. A fully explicit scheme would require excessively small time steps as a result of the stiff dislocation density evolution equations, while a fully implicit scheme would require including the plastic direction in the Newton-Raphson tangent, which would make each Newton-Raphson iteration slower. Therefore, in this approach, only stiff equations are treated implicitly and all others are treated explicitly.

To implement the implicit-explicit approach, Equations (6.1) to (6.11) must be temporally discretised. The discretised form of the internal state variable is derived from a first-order Taylor approximation,

$$\rho^{(\mathrm{n}+1)} = \rho^{(\mathrm{n})} + \dot{\rho}^{(\mathrm{n}+1)} \Delta t. \tag{6.15}$$

The plastic velocity gradient is approximated as a constant over a time step using,

$$\boldsymbol{L}_p^* = \boldsymbol{N}^{(\mathrm{n})} \dot{\lambda}^{(\mathrm{n}+1)}, \tag{6.16}$$

where a superscript asterix, $\bullet^*$, indicates that a value is approximated as being constant. The rate of plastic deformation is determined implicitly,

$$\hat{\dot{\lambda}}^{(\mathrm{n}+1)} = \left[\frac{1}{\eta}\left[\frac{\tau_y}{\hat{\tau}_f}\right]^{1/m}\right]^{(\mathrm{n}+1)}, \tag{6.17}$$

and the plastic direction is determined explicitly,

$$\boldsymbol{N}^{(\mathrm{n})} = \left[\boldsymbol{F}_e^T \boldsymbol{T} \boldsymbol{F}_e^{-T}\right]^{(\mathrm{n})}. \tag{6.18}$$

The plastic deformation is approximated via the substitution of Equation (6.16) into Equation (6.1),

$$\boldsymbol{F}_p(t) \approx \left[\boldsymbol{L}_p^*\right]^{-1} \dot{\boldsymbol{F}}_p(t). \tag{6.19}$$

where $\dot{\boldsymbol{F}}_p$ is approximated using

$$\dot{\boldsymbol{F}}_p \approx \frac{1}{\Delta t}\left[\boldsymbol{F}_p^{(\mathrm{n}+1)} - \boldsymbol{F}_p^{(\mathrm{n})}\right]. \tag{6.20}$$

Thus, an approximation of $\boldsymbol{F}_p^{(\mathrm{n}+1)}$ is obtained from Equations (6.19) and (6.20):

$$\boldsymbol{F}_p^{(\mathrm{n}+1)} = \left[\boldsymbol{I} - \Delta t \boldsymbol{L}_p^*\right]^{-1} \boldsymbol{F}_p^{(\mathrm{n})}. \tag{6.21}$$

6.2.2 Newton-Raphson Scheme

To avoid the conflation of steps in time and iterations of the Newton-Raphson scheme, an iteration is indicated by superscript braces, $\bullet^{\{\mathrm{n}+1\}}$, while a time step remains indicated by superscript parentheses, $\bullet^{(\mathrm{n}+1)}$. The Newton-Raphson method is a root-finding algorithm that iteratively approximates the root, $a^{\{\mathrm{n}+1\}}$, of a residual equation, r, from a prior approximation, $a^{\{\mathrm{n}\}}$, by means of a linear approximation of the residual,

$$a^{\{\mathrm{n}+1\}} = a^{\{\mathrm{n}\}} - r'\left(a^{\{\mathrm{n}\}}\right)^{-1} r\left(a^{\{\mathrm{n}\}}\right). \tag{6.22}$$

The nonlinear Equations (6.15) and (6.17) are satisfied by finding the root of the residual equations

$$r_1\left(\dot{\lambda}^{(\mathrm{n}+1)}, \rho^{(\mathrm{n}+1)}\right) = \dot{\lambda}^{(\mathrm{n}+1)} - \frac{1}{\eta}\left[\frac{\tau_y}{\hat{\tau}_f}\right]_{t=t^{(\mathrm{n}+1)}}^{1/m} \tag{6.23}$$

and

$$r_2\left(\dot{\lambda}^{(\mathrm{n}+1)}, \rho^{(\mathrm{n}+1)}\right) = \left[\rho^{(\mathrm{n}+1)} - \rho^{(\mathrm{n})}\right] - \Delta t \hat{\dot{\rho}}^{(\mathrm{n}+1)} \tag{6.24}$$

at each time step. The residual equations are linearised and composed into a linear system from which the increments to $\rho^{(\mathrm{n}+1)}$ and $\dot{\lambda}^{(\mathrm{n}+1)}$ are computed for each time step

$$\begin{bmatrix} r_1 \\ r_2 \end{bmatrix} = - \begin{bmatrix} \dfrac{\partial r_1}{\partial \dot{\lambda}^{(\mathrm{n}+1)}} & \dfrac{\partial r_1}{\partial \rho^{(\mathrm{n}+1)}} \\ \dfrac{\partial r_2}{\partial \dot{\lambda}^{(\mathrm{n}+1)}} & \dfrac{\partial r_2}{\partial \rho^{(\mathrm{n}+1)}} \end{bmatrix} \begin{bmatrix} \Delta\dot{\lambda} \\ \Delta\rho \end{bmatrix} \tag{6.25}$$

To assemble the linear system in Equation (6.25), the following directional derivatives are required:

$$\mathrm{D}r_1 \left[\Delta\dot{\lambda}\right] = \frac{\partial r_1}{\partial \dot{\lambda}^{(\mathrm{n}+1)}} \Delta\dot{\lambda}, \tag{6.26}$$

$$\mathrm{D}r_1 \left[\Delta\rho\right] = \frac{\partial r_1}{\partial \rho^{(\mathrm{n}+1)}} \Delta\rho, \tag{6.27}$$

$$\mathrm{D}r_2 \left[\Delta\dot{\lambda}\right] = \frac{\partial r_2}{\partial \dot{\lambda}^{(\mathrm{n}+1)}} \Delta\dot{\lambda}, \tag{6.28}$$

$$\mathrm{D}r_2 \left[\Delta\rho\right] = \frac{\partial r_2}{\partial \rho^{(\mathrm{n}+1)}} \Delta\rho. \tag{6.29}$$

The partial differentiation of the first residual with respect to the rate of plastic strain is given by

$$\frac{\partial r_1}{\partial \dot{\lambda}^{(\mathrm{n}+1)}} = \frac{\partial}{\partial \dot{\lambda}^{(\mathrm{n}+1)}} \left(\dot{\lambda}^{(\mathrm{n}+1)} - \frac{1}{\eta} \left[\frac{\tau_y}{\hat{\tau}_f} \right]^{1/m}_{t=t^{(\mathrm{n}+1)}} \right), \tag{6.30}$$

which, by the chain rule, results in

$$\frac{\partial r_1}{\partial \dot{\lambda}^{(\mathrm{n}+1)}} = \frac{\partial \dot{\lambda}^{(\mathrm{n}+1)}}{\partial \dot{\lambda}^{(\mathrm{n}+1)}} - \frac{\partial}{\partial \tau_y} \left(\frac{1}{\eta} \left[\frac{\tau_y}{\hat{\tau}_f} \right]^{1/m} \right) \frac{\partial \tau_y}{\partial \boldsymbol{F}_p^{(\mathrm{n}+1)}} : \frac{\partial \boldsymbol{F}_p^{(\mathrm{n}+1)}}{\partial \boldsymbol{L}_p^*} : \frac{\partial \boldsymbol{L}_p^*}{\partial \dot{\lambda}^{(\mathrm{n}+1)}}, \tag{6.31}$$

$$= 1 - \frac{\tau_y^{[1-m]/m}}{m\eta \hat{\tau}_f^{1/m}} \frac{\partial \tau_y}{\partial \boldsymbol{F}_p^{(\mathrm{n}+1)}} : \frac{\partial \boldsymbol{F}_p^{(\mathrm{n}+1)}}{\partial \boldsymbol{L}_p^*} : \boldsymbol{N}^{\mathrm{n}}. \tag{6.32}$$

Equation (6.32) requires the derivative of the plastic deformation gradient with respect to the plastic velocity gradient, which is approximated as

$$\frac{\partial \boldsymbol{F}_p^{(\mathrm{n}+1)}}{\partial \boldsymbol{L}_p^*} = \Delta t \left[\boldsymbol{I} - \Delta t \boldsymbol{L}_p^* \right]^{-1} \odot \boldsymbol{F}_p^{(\mathrm{n}+0.5)}. \tag{6.33}$$

The first residual must also be differentiated with respect to dislocation density:

$$\frac{\partial r_1}{\partial \rho^{(\mathrm{n}+1)}} = \frac{\partial}{\partial \rho^{(\mathrm{n}+1)}} \left(\dot{\lambda}^{(\mathrm{n}+1)} - \frac{1}{\eta} \left[\frac{\tau_y}{\hat{\tau}_f} \right]^{1/m} \right), \tag{6.34}$$

$$= \frac{\tau_y^{1/m}\hat{\tau}_f^{[-1-m]/m}}{\eta m}\frac{\partial\hat{\tau}_f}{\partial\rho^{(\mathrm{n+1})}}. \tag{6.35}$$

where

$$\frac{\partial\hat{\tau}_f}{\partial\rho^{(\mathrm{n+1})}} = \frac{M\alpha\mu b}{2\sqrt{\rho^{(\mathrm{n+1})}}}. \tag{6.36}$$

The partial differentiation of the second residual proceeds in the same fashion: first with respect to the rate of plastic strain,

$$\frac{\partial r_2}{\partial\dot{\lambda}^{(\mathrm{n+1})}} = \frac{\partial}{\partial\dot{\lambda}^{(\mathrm{n+1})}}\left(\left[\rho^{(\mathrm{n+1})} - \rho^{(\mathrm{n})}\right] - \Delta t\hat{\dot{\rho}}^{(\mathrm{n+1})}\right), \tag{6.37}$$

$$= -\Delta t\frac{\partial\hat{\dot{\rho}}^{(\mathrm{n+1})}}{\partial\dot{\lambda}^{(\mathrm{n+1})}},, \tag{6.38}$$

and then with respect to dislocation density,

$$\frac{\partial r_2}{\partial\rho^{(\mathrm{n+1})}} = \frac{\partial}{\partial\rho^{(\mathrm{n+1})}}\left(\left[\rho^{(\mathrm{n+1})} - \rho^{(\mathrm{n})}\right] - \Delta t\hat{\dot{\rho}}^{(\mathrm{n+1})}\right), \tag{6.39}$$

$$= 1 - \Delta t\frac{\partial\hat{\dot{\rho}}^{(\mathrm{n+1})}}{\partial\rho^{(\mathrm{n+1})}}. \tag{6.40}$$

Recall that the dislocation density evolution, $\hat{\dot{\rho}}$, is a function of dislocation density and the magnitude of the rate of plastic deformation. Therefore, the following quantities are required for Equations (6.38) and (6.40), where the particular dislocation density evolution model from which the quantity is derived is denoted by KMM for the Kocks-Mecking equation, or HBM for the Hariharan-Barlat equation:

$$\text{KMM}: \quad \frac{\partial\hat{\dot{\rho}}^{(\mathrm{n+1})}}{\partial\dot{\lambda}^{(\mathrm{n+1})}} = M\left[k_1\sqrt{\rho^{(\mathrm{n+1})}} - k_2\rho^{(\mathrm{n+1})}\right], \tag{6.41}$$

$$\text{KMM}: \quad \frac{\partial\hat{\dot{\rho}}^{(\mathrm{n+1})}}{\partial\rho^{(\mathrm{n+1})}} = M\left[\frac{k_1}{2\sqrt{\rho^{(\mathrm{n+1})}}} - k_2\right]\dot{\lambda}^{(\mathrm{n+1})}, \tag{6.42}$$

$$\text{HBM}: \quad \frac{\partial\hat{\dot{\rho}}^{(\mathrm{n+1})}}{\partial\dot{\lambda}^{(\mathrm{n+1})}} = M\left[k\left[1 - \exp\left(-\psi\sqrt{\rho^{(\mathrm{n+1})}}\right)\right] + k_2\rho^{(\mathrm{n+1})}\right], \tag{6.43}$$

$$\text{HBM}: \quad \frac{\partial\hat{\dot{\rho}}^{(\mathrm{n+1})}}{\partial\rho^{(\mathrm{n+1})}} = M\left[\frac{k\psi\exp\left(-\psi\sqrt{\rho^{(\mathrm{n+1})}}\right)}{2\sqrt{\rho^{(\mathrm{n+1})}}} - k_2\right]\dot{\lambda}^{(\mathrm{n+1})}. \tag{6.44}$$

The directional derivatives necessary for the construction of the linear system given by

Equation (6.25) are, therefore,

$$\mathrm{D}r_1\left[\Delta\dot{\lambda}\right] = \left[1 - \frac{\tau_y^{[1-m]/m}}{m\eta\hat{\tau}_f^{1/m}}\frac{\partial\tau_y}{\partial\boldsymbol{F}_p} : \frac{\partial\boldsymbol{F}_p^{(\mathrm{n}+1)}}{\partial\boldsymbol{L}_p^*} : \boldsymbol{N}^{(\mathrm{n})}\right]\Delta\dot{\lambda}, \tag{6.45}$$

$$\mathrm{D}r_1\left[\Delta\rho\right] = \left[\frac{1}{\eta m}\tau_y^{1/m}\hat{\tau}_f^{[-1-m]/m}\frac{\partial\hat{\tau}}{\partial\rho^{(\mathrm{n}+1)}}\right]\Delta\rho, \tag{6.46}$$

$$\mathrm{D}r_2\left[\Delta\dot{\lambda}\right] = \left[-\Delta t\frac{\partial\hat{\dot{\rho}}^{(\mathrm{n}+1)}}{\partial\dot{\lambda}^{(\mathrm{n}+1)}}\right]\Delta\dot{\lambda}, \tag{6.47}$$

$$\mathrm{D}r_2\left[\Delta\rho\right] = \left[1 - \Delta t\frac{\partial\hat{\dot{\rho}}^{(\mathrm{n}+1)}}{\partial\rho^{(\mathrm{n}+1)}}\right]\Delta\rho. \tag{6.48}$$

Equation (6.45) requires the computation of the evolution of the equivalent scalar stress with respect to plastic deformation, which is derived as follows:
Using the chain rule,

$$\frac{\partial\tau_y}{\partial\boldsymbol{F}_p} = \frac{\partial\tau_y}{\partial\|\bar{\boldsymbol{\tau}}\|}\frac{\partial\|\bar{\boldsymbol{\tau}}\|}{\partial\boldsymbol{\tau}}\frac{\partial\boldsymbol{\tau}}{\partial\boldsymbol{F}_p} \tag{6.49}$$

where $\bar{\boldsymbol{\tau}}$ is the isochoric Kirchhoff stress. The first two terms are derived from Equations (6.10) and (6.8), respectively,

$$\frac{\partial\tau_y}{\partial\boldsymbol{F}_p} = \sqrt{\frac{3}{2}}\frac{\bar{\boldsymbol{\tau}}}{\|\bar{\boldsymbol{\tau}}\|} : \mathbb{P} : \mathbb{c}_{e\boldsymbol{\tau}}\left[\boldsymbol{F}_e \odot \boldsymbol{F}^{-1}\right], \tag{6.50}$$

while the derivation of $\dfrac{\partial\boldsymbol{\tau}}{\partial\boldsymbol{F}_p}$ is left to Appendix C.

6.3 Material Point-Level Implementation

The behaviour of the constitutive model is elucidated by examining a single material point undergoing deformation. This is achieved by prescribing a loading path defined by the deformation gradient and stress tensors for a material point. The method of prescribing a loading path is outlined in Section 6.3.1, and the method is employed to create loading cases in Section 6.3.2.

6.3.1 Prescription of the Loading Path

In order to evaluate whether the proposed material models are formulated correctly, a methodology to assess the behaviour at a single material point is implemented numerically. This requires specifying idealised cases which may not be directly linked to experimental data, but are still required to test certain aspects of the models. In this material point-level implementation, the deformation gradient and stress tensors are used to prescribe the loading path. In many cases, only some components of the deformation gradient and stress tensors are known; typically, the unknown components of the deformation gradient correspond to the known components of the stress tensor. In these cases, which are referred to as partially-defined henceforth, an iterative scheme is used to determine the values for the unknown entries in the deformation gradient such that the known values of stress are satisfied. The remaining cases are entirely defined, which means that all components of the deformation gradient are prescribed.

6.3.2 Definition of Loading Cases

Consider the following loading cases:

Case 1: a loading case in which the deformation gradient is entirely defined and the F_{11} of the deformation gradient is increased linearly as a function of time,

$$\boldsymbol{F}_{\text{end}} = \text{diag}\begin{bmatrix} F_{11} & 1 & 1 \end{bmatrix}, \tag{6.51}$$

Case 2: a loading case in which the deformation gradient is entirely defined to prescribe symmetric shear, that is where the components $F_{12} = F_{21} = \gamma$ are increased linearly as a function of time,

$$\boldsymbol{F}_{\text{end}} = \begin{bmatrix} 1 & \gamma & 0 \\ \gamma & 1 & 0 \\ 0 & 0 & 1 \end{bmatrix}, \tag{6.52}$$

Case 3: a uniaxial loading case, in which one component of the deformation gradient, F_{11}, is defined and increased linearly as a function of time, and the remaining unknown principal stretches, λ_i, are solved such that the stress components corresponding to the unknown principal stresses are zero,

$$\boldsymbol{F}_{\text{end}} = \text{diag}\begin{bmatrix} F_{11} & \lambda_2 & \lambda_3 \end{bmatrix}, \qquad \boldsymbol{\tau} = \text{diag}\begin{bmatrix} \tau_{11} & 0 & 0 \end{bmatrix}, \tag{6.53}$$

where τ_{11} is unknown,

Case 4: and a biaxial loading case, in which component F_{11} is increased linearly as a function of time, $F_{33} = 1$, and the unknown principal stretch λ_2 is solved to enforce a zero stress state on the corresponding axis in the stress matrix,

$$\boldsymbol{F}_{\text{end}} = \text{diag}\begin{bmatrix} F_{11} & \lambda_2 & F_{33} \end{bmatrix}, \qquad \boldsymbol{\tau} = \text{diag}\begin{bmatrix} \tau_{11} & 0 & \tau_{33} \end{bmatrix}, \tag{6.54}$$

where τ_{11} and τ_{33} are unknown.

These four cases have been selected to elucidate the behaviour of the model under multiaxial loading. The partially-defined Cases 3 and 4 are formulated specifically to replicate the commonly-employed uniaxial tensile test and plane-strain compression test techniques, respectively. Two algorithms are presented in this section to demonstrate the loading procedure for an entirely-defined case, such as in Cases 1 and 2, and for a partially-defined case, such as in Cases 3 and 4.

An Entirely-Defined Loading Case

Consider the entirely-defined Case 1. All components of the deformation gradient are defined at the start and end of the loading procedure, and the computation of the deformation gradient at each time step is performed simply by incrementing the deformation gradient. The loading procedure is outlined in Algorithm 1. Following the definition of the loading case and the prescription of initial conditions, computation at each time step commences. At each time step, the quantities computed in the previous time step provide the initial conditions, the deformation gradient is incremented, and the initial value problem posed in Section 6.1 is solved to compute all the quantities for the current time step. During the computation of all quantities using $\boldsymbol{F}^{(\text{n}+1)}$, a Newton-Raphson scheme is employed to compute $\dot{\lambda}^{(\text{n}+1)}$ and $\rho^{(\text{n}+1)}$.

Algorithm 1: Case 1 and Case 2: An Entirely-Defined Loading Case

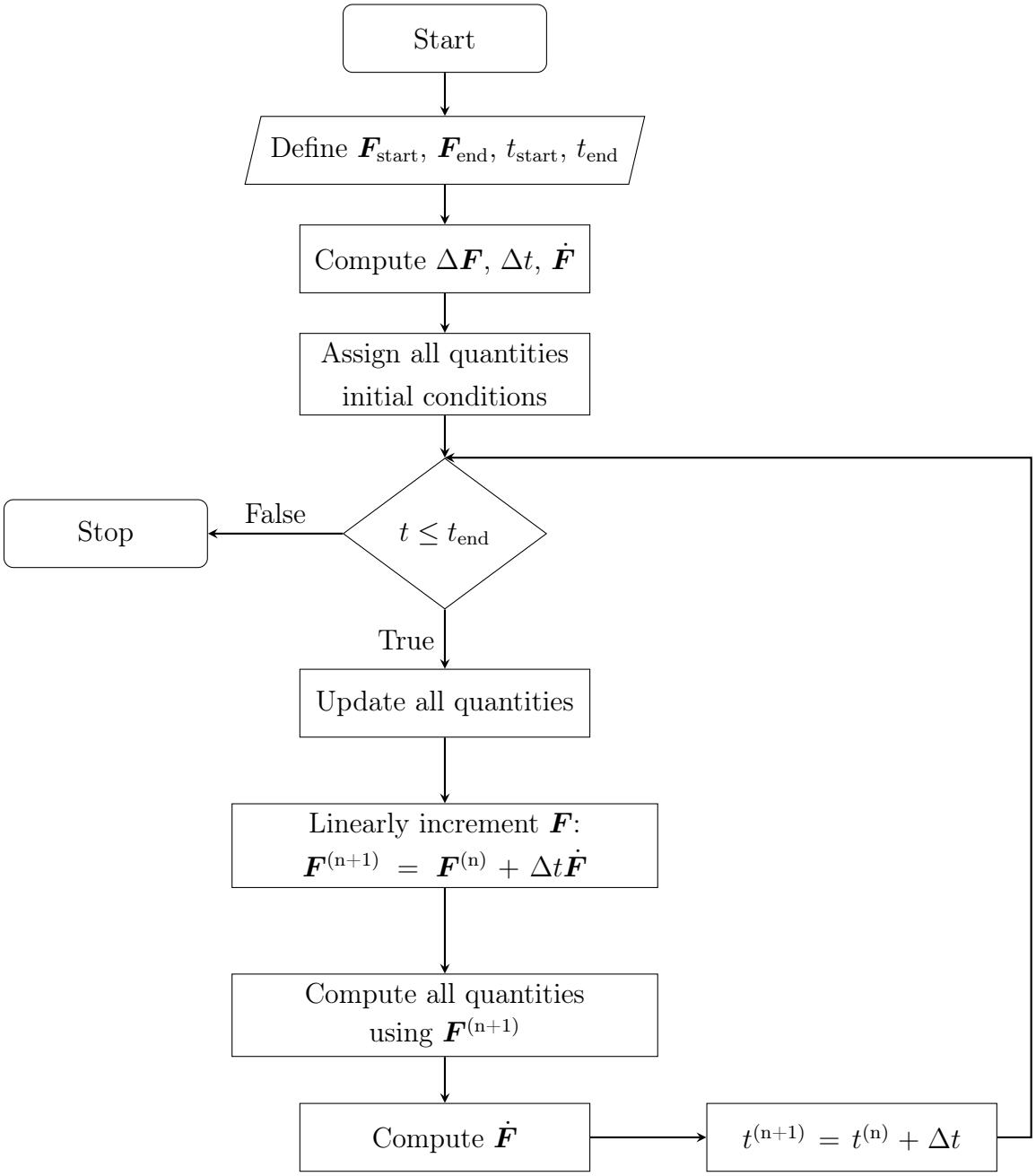

1

A Partially-Defined Loading Case

Consider the partially-defined Case 4. This case may be used to represent plane strain compression. If plane strain compression is applied to an isotropic, transversely isotropic, or orthotropic material such that the preferred directions align with the loading axes, the resulting strain tensor takes the form

$$\boldsymbol{E} = \operatorname{diag}\begin{bmatrix} E_{11} & E_{22} & 0 \end{bmatrix}, \tag{6.55}$$

and $\tau_{22} = 0$. This is implemented by prescribing two loading axes: one that drives the principal stretch in the $\boldsymbol{e}_1$-direction, and one that constrains the principal stretch in the $\boldsymbol{e}_3$-direction. Therefore, principal stretches in the first and third directions are defined; λ_1 is linearly incremented at each time step, while $\lambda_3 = 1$ to ensure that is no deformation in the $\boldsymbol{e}_3$-direction. λ_2 is solved for to ensure that $\tau_{22} = 0$. Although the partially-defined procedure detailed in Algorithm 2 requires the same inputs as the entirely-defined loading procedure in Algorithm 1, an extra computation at each time step is required to enforce the zero-stress state along the $\boldsymbol{e}_2$-axis.

After the initial conditions are inputted and the defined principal stretches are incremented, the principal stretch λ_2 is found using a root-finding algorithm that solves for λ_2 such that the Kirchhoff stress in the corresponding direction is zero, i.e. $\tau_{22} = 0$.

Algorithm 2: Case 4: A Partially-Defined Loading Case

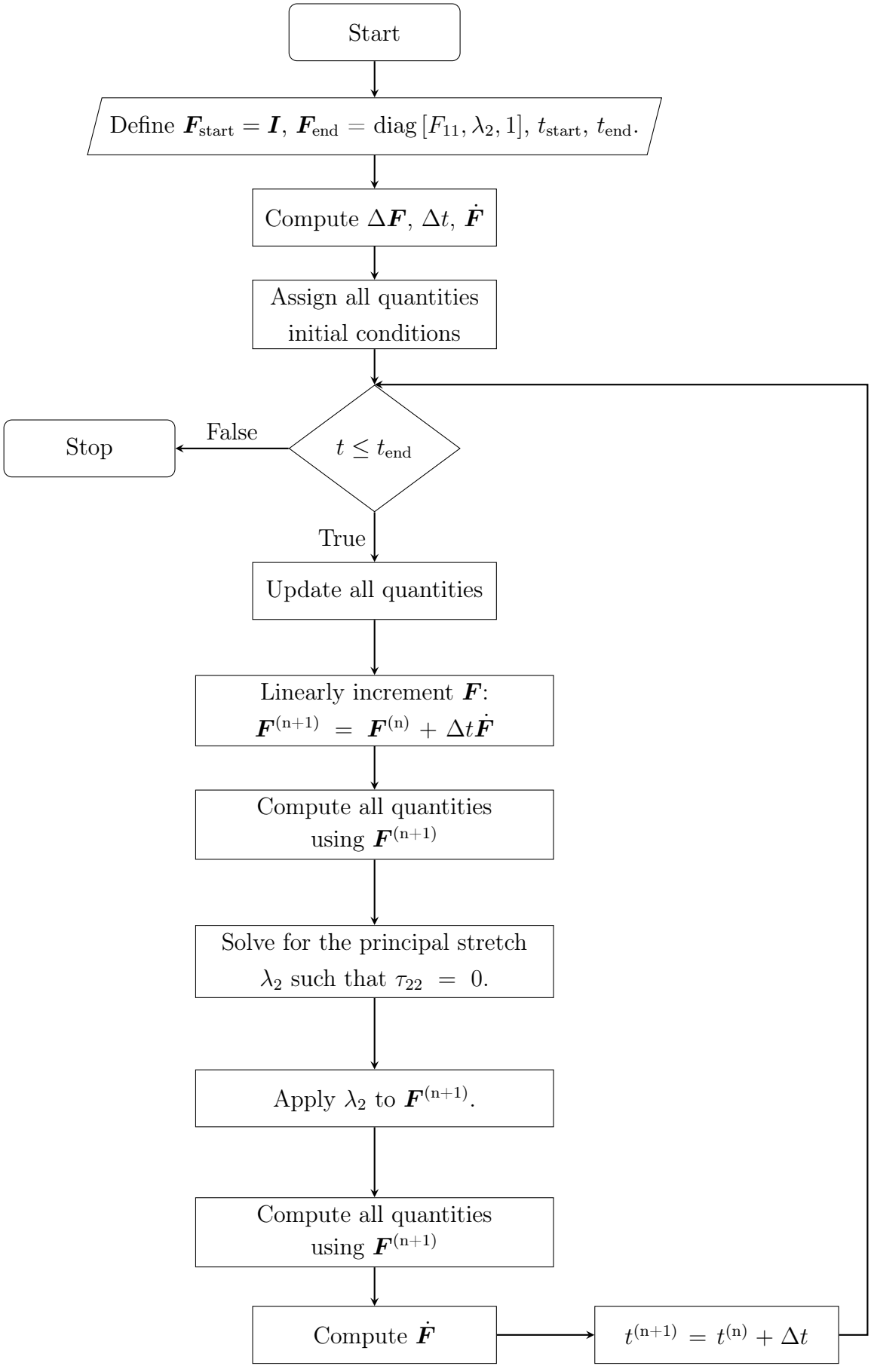

1

Chapter 7

Verification of the Numerical Solution

In this chapter, the quasi-analytical solutions for three loading cases, independent of those considered in the preceding chapter, are derived. The quasi-analytical solution for each case is derived by simplifying the set of differential equations required for a solution via analytical manipulation techniques, and then applying an appropriate numerical method to solve the simplified set of differential equations. The mechanical behaviour of an aluminium alloy [28] under each loading scenario is computed from both the quasi-analytical solution method and the numerical solution method described in Chapter 6, and the results are compared to verify that the finite-strain constitutive model has been implemented in the numerical setting correctly.

The chapter begins with the derivation of the analytically simplified equations used for the quasi-analytical solution procedure. The quasi-analytical solution for a uniaxial loading case is presented in Section 7.1.1, the quasi-analytical solution for a symmetric shear loading case is similarly presented in Section 7.1.2, and the solution for a planar loading case follows in Section 7.1.3. A comparison of the quasi-analytical solutions to the numerical solution is presented in Section 7.2, followed by a discussion in Section 7.3.

7.1 Quasi-Analytical Solutions

The quasi-analytical solutions for a uniaxial loading, a shear loading case, and a planar loading case are derived in this section.

7.1.1 Case 1: Uniaxial Loading

A uniaxial linear ramp is prescribed by the deformation gradient

$$\boldsymbol{F} = \operatorname{diag}\begin{bmatrix} F_{11} & 1 & 1 \end{bmatrix} = \boldsymbol{F}_e \boldsymbol{F}_p, \tag{7.1}$$

where

$$F_{11} = 1 + \frac{t}{t_{\text{end}}} \left[F_{11,\,\text{end}} - 1 \right] \quad \text{with} \quad t \in [0, t_{\text{end}}] \,. \tag{7.2}$$

$\boldsymbol{F}$ is decomposed into elastic and plastic components and $\boldsymbol{F}_e$ is expressed in terms of $\boldsymbol{F}_p$, which yields

$$\boldsymbol{F}_e = \text{diag} \begin{bmatrix} \dfrac{F_{11}}{F_{p11}} & \dfrac{1}{F_{p22}} & \dfrac{1}{F_{p33}} \end{bmatrix}, \tag{7.3}$$

with

$$\boldsymbol{F}_p = \text{diag} \begin{bmatrix} F_{p11} & F_{p22} & F_{p33} \end{bmatrix}. \tag{7.4}$$

This formulation results in three unknowns: F_{p11}, F_{p22}, and F_{p33}. Given that $\boldsymbol{F}_e$ is symmetric,

$$\boldsymbol{B}_e = \boldsymbol{C}_e = \text{diag} \begin{bmatrix} \left[\dfrac{F_{11}}{F_{p11}} \right]^2 & F_{p22}^{-2} & F_{p33}^{-2} \end{bmatrix}. \tag{7.5}$$

By enforcing isochoric plastic flow, as discussed in Chapter 5, such that

$$J_p = 1, \tag{7.6}$$

and, since,

$$\det(\boldsymbol{F}) = \det(\boldsymbol{F}_e) \det(\boldsymbol{F}_p), \tag{7.7}$$

the elastic Jacobian is expressed as

$$J_e = \frac{F_{11}}{J_p} = 1, \tag{7.8}$$

from which the third invariant of $\boldsymbol{B}_e$ is thus

$$I_3 = J_e^2 = F_{11}^2. \tag{7.9}$$

Using a Neo-Hookean formulation [62], the elastic Kirchhoff stress is determined by

$$\boldsymbol{\tau} = \mu \boldsymbol{B}_e + \frac{1}{2} \left[\lambda I_3 - \lambda - 2\mu \right] \boldsymbol{I}, \tag{7.10}$$

where the isochoric part is

$$\bar{\boldsymbol{\tau}} = \boldsymbol{\tau} - \frac{1}{3} \boldsymbol{I} \,\text{tr}(\boldsymbol{\tau}). \tag{7.11}$$

Since

$$\mathrm{tr}\,(\boldsymbol{\tau}) = \mu\,\mathrm{tr}\,(\boldsymbol{B}_e) + \frac{3}{2}\left[\lambda I_3 - \lambda - 2\mu\right], \tag{7.12}$$

Equation (7.11) becomes

$$\bar{\boldsymbol{\tau}} = \mu\left[\boldsymbol{B}_e - \frac{1}{3}\,\mathrm{tr}\,(\boldsymbol{B}_e)\,\boldsymbol{I}\right], \tag{7.13}$$

and the Frobenius norm of $\bar{\boldsymbol{\tau}}$ is given by

$$\|\bar{\boldsymbol{\tau}}\| = \mu\left[\mathrm{tr}\left(\boldsymbol{B}_e^2\right) - \frac{1}{3}\,\mathrm{tr}\,(\boldsymbol{B}_e)^2\right]^{\frac{1}{2}}. \tag{7.14}$$

The direction of plastic flow in the spatial domain is determined by

$$\boldsymbol{T} = \frac{\bar{\boldsymbol{\tau}}}{\|\bar{\boldsymbol{\tau}}\|} = \frac{\mu}{\|\bar{\boldsymbol{\tau}}\|}\left[\boldsymbol{B}_e - \frac{1}{3}\,\mathrm{tr}\,(\boldsymbol{B}_e)\,\boldsymbol{I}\right] \tag{7.15}$$

and, as such,

$$\boldsymbol{N} = \boldsymbol{F}_e^T\boldsymbol{T}\boldsymbol{F}_e^{-T} = \frac{\mu}{\|\bar{\boldsymbol{\tau}}\|}\left[\boldsymbol{C}_e - \frac{1}{3}\,\mathrm{tr}\,(\boldsymbol{C}_e)\,\boldsymbol{I}\right]. \tag{7.16}$$

The evolution of the plastic deformation gradient can now be computed from

$$\dot{\boldsymbol{F}}_p = \boldsymbol{L}_p\boldsymbol{F}_p = \dot{\lambda}\boldsymbol{N}\boldsymbol{F}_p, \tag{7.17}$$

$$= \frac{\mu\dot{\lambda}}{\|\bar{\boldsymbol{\tau}}\|}\left[\boldsymbol{C}_e\boldsymbol{F}_p - \frac{1}{3}\,\mathrm{tr}\,(\boldsymbol{C}_e)\,\boldsymbol{F}_p\right], \tag{7.18}$$

where

$$\boldsymbol{C}_e\boldsymbol{F}_p = \mathrm{diag}\left[\frac{F_{11}^2}{F_{p11}} \quad F_{p22}^{-1} \quad F_{p33}^{-1}\right]. \tag{7.19}$$

Accordingly, the evolution of the variable F_{p11} is

$$\dot{F}_{p11} = \frac{\mu\dot{\lambda}}{\|\bar{\boldsymbol{\tau}}\|}\left[\frac{F_{11}^2}{F_{p11}} - \frac{1}{3}\,\mathrm{tr}\,(\boldsymbol{B}_e)\,F_{p11}\right]. \tag{7.20}$$

Rotational symmetry implies that $F_{p22} = F_{p33}$ and, by enforcing isochoric plastic flow, a relationship between the three diagonal plastic deformation components is found to be

$$J_p = 1 = F_{p11}F_{p22}^2, \tag{7.21}$$

$$\therefore \quad F_{p22} = F_{p33} = F_{p11}^{-1/2}. \tag{7.22}$$

As a result, only two degrees of freedom remain: F_{p11} and ρ. A system of two nonlinear ordinary differential equations results from Equations (6.6), (7.20), and either the Kocks-Mecking or Hariharan-Barlat dislocation density evolution equation.
The first differential equation describes the plastic deformation evolution,

$$\dot{F}_{p11} = \frac{2\mu}{3\eta\|\bar{\boldsymbol{\tau}}\|}\left[\frac{\tau_y}{\hat{\tau}_f}\right]^{1/m}\left[\frac{F_{11}^2}{F_{p11}} - F_{p11}^2\right], \tag{7.23}$$

and the second, the dislocation density evolution is either

$$\text{KMM:}\quad \dot{\rho} = \frac{M}{\eta}\left[\frac{\tau_y}{\hat{\tau}_f}\right]^{1/m}\left[k_1\sqrt{\rho} - k_2\rho\right], \tag{7.24a}$$

or

$$\text{HBM:}\quad \dot{\rho} = \frac{M}{\eta}\left[\frac{\tau_y}{\hat{\tau}_f}\right]^{1/m}\left[k\left[1 - \exp\left(-\psi\sqrt{\rho}\right)\right] - k_2\rho\right]. \tag{7.24b}$$

7.1.2 Case 2: Symmetric Shear Loading

Symmetric shear loading is defined by the deformation gradient

$$\boldsymbol{F} = \begin{bmatrix} 1 & F_{12} & 0 \\ F_{21} & 1 & 0 \\ 0 & 0 & 1 \end{bmatrix}, \tag{7.25}$$

where

$$F_{12} = F_{21} = \frac{t\gamma}{t_{\text{end}}} \quad \text{with} \quad t \in [0, t_{\text{end}}]. \tag{7.26}$$

This definition of the deformation gradient is convenient as it contains shear components which are useful for testing the numerical implementation and admits a tractable analytical solution. $\boldsymbol{F}$ yields the right Cauchy-Green tensor

$$\boldsymbol{C} = \begin{bmatrix} 1+\gamma^2 & 2\gamma & 0 \\ 2\gamma & 1+\gamma^2 & 0 \\ 0 & 0 & 1 \end{bmatrix} = \boldsymbol{I} + \gamma\begin{bmatrix} \gamma & 2 & 0 \\ 2 & \gamma & 0 \\ 0 & 0 & 0 \end{bmatrix}. \tag{7.27}$$

Initially, it is assumed that $\boldsymbol{F}_p$ will have the form

$$\boldsymbol{F}_p = \begin{bmatrix} F_{p11} & F_{p12} & 0 \\ F_{p12} & F_{p11} & 0 \\ 0 & 0 & F_{p33} \end{bmatrix} \tag{7.28}$$

throughout loading. This results in three independent components: F_{p11}, F_{p12}, and F_{p33}. The determinant of the deformation gradient during loading results in the relation

$$\det(\boldsymbol{F}_p) = 1 = F_{p11}^2 F_{p33} - F_{p12}^2 F_{p33}, \tag{7.29}$$

$$\therefore \quad F_{p33} = \left[F_{p11}^2 - F_{p12}^2\right]^{-1}, \tag{7.30}$$

and the inverse of the plastic deformation gradient becomes

$$\boldsymbol{F}_p^{-1} = F_{p33} \begin{bmatrix} F_{p11} & -F_{p12} & 0 \\ -F_{p12} & F_{p11} & 0 \\ 0 & 0 & F_{p33}^{-2} \end{bmatrix}. \tag{7.31}$$

Substitution of Equation (7.31) back into Equation (7.17), noting that $\boldsymbol{C} = \boldsymbol{F}_p^T \boldsymbol{C}_e \boldsymbol{F}_p$, results in

$$\dot{\boldsymbol{F}}_p = \frac{\dot{\lambda}\mu}{\|\bar{\boldsymbol{\tau}}\|} \left[\boldsymbol{F}_p^{-T} \boldsymbol{C} - \frac{1}{3} \boldsymbol{F}_p \operatorname{tr}(\boldsymbol{C}_e)\right], \tag{7.32}$$

$$= \frac{\dot{\lambda}\mu}{\|\bar{\boldsymbol{\tau}}\|} \left[F_{p33} \begin{bmatrix} F_{p11} & -F_{p12} & 0 \\ -F_{p12} & F_{p11} & 0 \\ 0 & 0 & F_{p33}^{-2} \end{bmatrix} \boldsymbol{C} - \frac{1}{3} \boldsymbol{F}_p \operatorname{tr}(\boldsymbol{C}_e)\right], \tag{7.33}$$

which reveals that $\dot{F}_{p11} = \dot{F}_{p22}$ and that $\dot{F}_{p12} = \dot{F}_{p21}$. As F_{p33} can be related to F_{p11} and F_{p12} by Equation (7.30), the problem is reduced to two independent variables, for which the evolution equations are derived from Equation (7.32) where

$$\operatorname{tr}(\boldsymbol{C}_e) = \boldsymbol{C} : \boldsymbol{C}_p^{-1} \tag{7.34}$$

and

$$\boldsymbol{C}_p^{-1} = \boldsymbol{F}_p^{-1} \boldsymbol{F}_p^{-T} = F_{p33}^2 \begin{bmatrix} F_{p11}^2 + F_{p12}^2 & -2F_{p11}F_{p12} & 0 \\ -2F_{p11}F_{p12} & F_{p11}^2 + F_{p12}^2 & 0 \\ 0 & 0 & \left[F_{p11}^2 - F_{p12}^2\right]^{-4} \end{bmatrix}, \tag{7.35}$$

and

$$\operatorname{tr}(\boldsymbol{C}_e) = \frac{2\left[1+\gamma^2\right]\left[F_{p11}^2 + F_{p12}^2\right] - 8\gamma F_{p11}F_{p12}}{\left[F_{p11}^2 - F_{p12}^2\right]^2} + \left[F_{p11}^2 - F_{p12}^2\right]^2. \tag{7.36}$$

Thus, a system of three nonlinear ordinary differential equations results from Equations (6.6), (7.32), and either the Kocks-Mecking or Hariharan-Barlat dislocation density evolution equation:

The evolution equations of two components of the plastic deformation gradient are

$$\dot{F}_{p11} = \frac{\mu}{\eta \|\bar{\boldsymbol{\tau}}\|} \left[\frac{\tau_y}{\hat{\tau}_f}\right]^{1/m} \left[F_{p33}\left[F_{p11}\left[1+\gamma^2\right] - 2\gamma F_{p12}\right] - \frac{1}{3}\operatorname{tr}\left(\boldsymbol{C}_e\right) F_{p11}\right], \tag{7.37}$$

and

$$\dot{F}_{p12} = \frac{\mu}{\eta \|\bar{\boldsymbol{\tau}}\|} \left[\frac{\tau_y}{\hat{\tau}_f}\right]^{1/m} \left[F_{p33}\left[2\gamma F_{p11} - F_{p12}\left[1+\gamma^2\right]\right] - \frac{1}{3}\operatorname{tr}\left(\boldsymbol{C}_e\right) F_{p12}\right] \tag{7.38}$$

and dislocation density evolution, which is given by either

$$\text{KMM:} \quad \dot{\rho} = \frac{M}{\eta} \left[\frac{\tau_y}{\hat{\tau}_f}\right]^{1/m} \left[k_1\sqrt{\rho} - k_2\rho\right], \tag{7.39a}$$

or

$$\text{HBM:} \quad \dot{\rho} = \frac{M}{\eta} \left[\frac{\tau_y}{\hat{\tau}_f}\right]^{1/m} \left[k\left[1 - \exp\left(-\psi\sqrt{\rho}\right)\right] - k_2\rho\right]. \tag{7.39b}$$

7.1.3 Case 3: Planar Loading

A deformation gradient of the following form is used to test a special case of combined equi-biaxial and symmetric shear loading:

$$\boldsymbol{F} = \begin{bmatrix} F_{11} & F_{12} & 0 \\ F_{21} & F_{22} & 0 \\ 0 & 0 & 1 \end{bmatrix}, \tag{7.40}$$

where

$$F_{11} = F_{22} = 1 + \frac{t}{t_{\text{end}}}\left[\omega - 1\right] \tag{7.41}$$

and

$$F_{12} = F_{21} = \frac{t\gamma}{t_{\text{end}}} \quad \text{where} \quad t \in [0, t_{\text{end}}] \tag{7.42}$$

The deformation gradient yields the right Cauchy-Green tensor

$$\boldsymbol{C} = \begin{bmatrix} \gamma^2+\omega^2 & 2\gamma\omega & 0 \\ 2\gamma\omega & \gamma^2+\omega^2 & 0 \\ 0 & 0 & 1 \end{bmatrix}. \tag{7.43}$$

The uniaxial component ω and the shear component γ are functions of time such that

$$\hat{\omega}(t) = \dot{\omega}t, \quad \text{and} \quad \hat{\gamma}(t) = \dot{\gamma}t. \tag{7.44}$$

The plastic deformation gradient is assumed to have the form

$$\boldsymbol{F}_p = \begin{bmatrix} F_{p11} & F_{p12} & 0 \\ F_{p12} & F_{p11} & 0 \\ 0 & 0 & F_{p33} \end{bmatrix}, \quad \boldsymbol{F}_p^{-1} = F_{p33} \begin{bmatrix} F_{p11} & -F_{p12} & 0 \\ -F_{p12} & F_{p11} & 0 \\ 0 & 0 & F_{p33}^{-2} \end{bmatrix} \tag{7.45}$$

where

$$F_{p33} = \left[F_{p11}^2 - F_{p12}^2\right]^{-1}. \tag{7.46}$$

From Equations (7.34), (7.43), and (7.45),

$$\operatorname{tr}(\boldsymbol{C}_e) = \frac{2\left[\left[F_{p11}^2 + F_{p12}^2\right]\left[\gamma^2+\omega^2\right] - 4\gamma\omega F_{p11}F_{p12}\right]}{\left[F_{p11}^2 - F_{p12}^2\right]^2} + \left[F_{p11}^2 - F_{p12}^2\right]^2. \tag{7.47}$$

Equations (7.45), (7.43), (7.47) are substituted into the general form of the rate of plastic deformation given by Equation (7.32) to arrive at the evolution equations for the independent plastic deformation components

$$\dot{F}_{p11} = \frac{\mu}{\eta\|\bar{\boldsymbol{\tau}}\|}\left[\frac{\tau_y}{\hat{\tau}_f}\right]^{1/m}\left[F_{p33}\left[F_{p11}\left[\gamma^2+\omega^2\right] - 2\gamma\omega F_{p12}\right] - \frac{1}{3}\operatorname{tr}(\boldsymbol{C}_e)\,F_{p11}\right], \tag{7.48}$$

$$\dot{F}_{p12} = \frac{\mu}{\eta\|\bar{\boldsymbol{\tau}}\|}\left[\frac{\tau_y}{\hat{\tau}_f}\right]^{1/m}\left[F_{p33}\left[2\gamma\omega F_{p11} - F_{p12}\left[\gamma^2+\omega^2\right]\right] - \frac{1}{3}\operatorname{tr}(\boldsymbol{C}_e)\,F_{p12}\right], \tag{7.49}$$

which are combined with an evolution equation for dislocation density to complete the nonlinear system of equations,

$$\text{KMM:} \quad \dot{\rho} = \frac{M}{\eta}\left[\frac{\tau_y}{\hat{\tau}_f}\right]^{1/m}\left[k_1\sqrt{\rho} - k_2\rho\right], \tag{7.50a}$$

or

$$\text{HBM:} \quad \dot{\rho} = \frac{M}{\eta}\left[\frac{\tau_y}{\hat{\tau}_f}\right]^{1/m}\left[k\left[1-\exp\left(-\psi\sqrt{\rho}\right)\right] - k_2\rho\right]. \tag{7.50b}$$

7.2 Results

In this section, the results from the quasi-analytical solutions based on the reduced analytical equations derived in the Section 7.1 are compared with the results from the numerical solution method presented in Chapter 6. The results are prefaced with an explanation of the quantification of the difference between the quasi-analytical and numerical solution methods in Section 7.2.1. The exploration of the results is structured in two parts: A comparison of the quasi-analytical solution and numerical solutions for

(i) the uniaxial linear ramp loading case, with independent variables F_{p11} and ρ, and

(ii) the shear and planar loading cases, with independent variables F_{p11}, F_{p12}, and ρ.

For each loading case, a table of the maximum and mean average normalised differences between the quasi-analytical solution and numerical solution methods for each dislocation density evolution model is provided. The independent variable evolution and normalised differences over time for each case are presented in several figures. The figures that concern the normalised differences include results from employing the solution methods at 10^4 time steps, 10^5 time steps, and 10^6 time steps. Although a formal convergence study is outside the scope of this work and, therefore, is not presented, these results provide an indication of the sensitivity of the solution methods to the time step size. Numerical convergence is not guaranteed for larger time step sizes. The results for planar loading at 10^4 are omitted as convergence of the root-finding method was not achieved.

The Kocks-Mecking and Hariharan-Barlat parameters used in these simulations are derived from experimental data for AA5032-T4 found in the literature [27]. These are documented in Table 7.1.

Table 7.1: Parameter values used in this work, as determined by least-squares analysis

Kocks-Mecking		Hariharan-Barlat		
k_1	k_2	k	k_2	ψ
3.0373×10^8	3.9213	6.7938×10^{15}	1.0633	0.0668

7.2.1 Quantification of Difference

To quantify the difference between the quasi-analytical solution and numerical solution methods, a normalised difference metric is used. This difference measure is computed at each time step i as follows,

$$\text{Norm. Diff.}^{(\text{i})} = \frac{|r_{\text{diff}}^{(\text{i})}|}{\max |\hat{\tau}_{f,\,\text{a}}^{(\text{i})}|} \tag{7.51}$$

where

$$r_{\text{diff}}^{(\text{i})} = \hat{\tau}_{f,\,\text{a}}^{(\text{i})} - \hat{\tau}_{f,\,\text{n}}^{(\text{i})} \tag{7.52}$$

The subscript $\bullet_{\text{a}}$ indicates the quasi-analytical result, and the subscript $\bullet_{\text{n}}$ indicates the numerical result. The mean average normalised differences are computed from the absolute values of the normalised differences at each time step.

7.2.2 Case 1: Uniaxial Loading

The uniaxial linear ramp is defined by the deformation gradient

$$\boldsymbol{F} = \operatorname{diag}\begin{bmatrix} F_{11} & 1 & 1 \end{bmatrix} \tag{7.53}$$

where

$$F_{11} = 1 + \frac{t}{5}\left[1.05 - 1\right] \quad \text{with} \quad t \in [0, 5]\,. \tag{7.54}$$

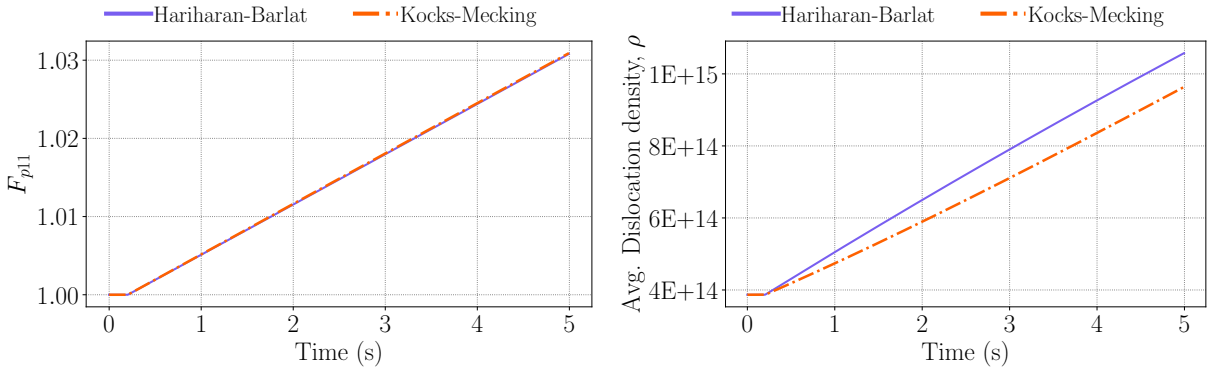

Figure 7.1: Evolution of the independent variables for uniaxial loading: (a) F_{p11} and (b) ρ.

To best match the conditions under which the experimental data was generated, a strain rate of approximately 5 s^{-1} is supposed. A five-second test time is used throughout this chapter to ensure that the each test case includes the finite-strain regime under the given strain rate. The evolutions of the independent plastic deformation component and average dislocation density over time are shown in Figure 7.1. An examination of the independent variables plotted against time shows an imperceptible difference between the quasi-analytical and numerical solution methods at any of the three time step sizes.

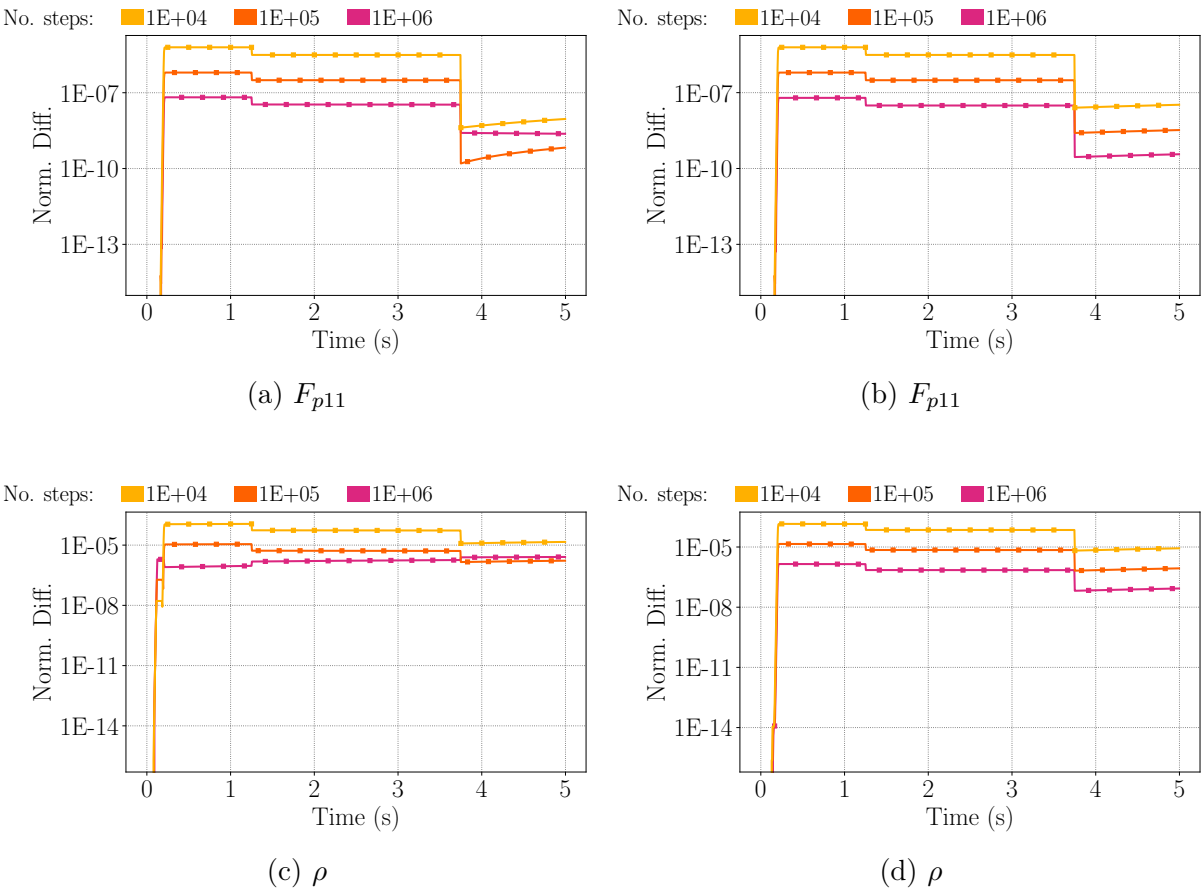

(a) F_{p11} (b) F_{p11}

(c) ρ (d) ρ

Figure 7.2: The normalised differences between the quasi-analytical and numerical solution methods for the independent variables for uniaxial loading are presented for the Kocks-Mecking model in the left column (a, c), and the Hariharan-Barlat model in the right column (b, d). The deformation occurs over 5 seconds in either 10^4, 10^5, or 10^6 steps.

The normalised differences between the quasi-analytical and numerical solution methods for each dislocation density evolution model are shown in Figure 7.2, and the mean average and maximum normalised differences for each time step size and dislocation density evolution model are recorded in Table 7.2. The maximum normalised differences occur for both independent variables during the first quarter of the simulation using either dislocation density evolution models, after which the differences between the two solution methods decrease significantly.

Table 7.2: Maximum and mean average normalised differences between the quasi-analytical and numerical solution method results for the independent variables for uniaxial linear ramp loading.

	Kocks-Mecking			Hariharan-Barlat		
No. time steps	10^4	10^5	10^6	10^4	10^5	10^6
Norm. Diff.	F_{p11}					
Mean avg.	2.88×10^{-6}	2.88×10^{-7}	3.14×10^{-8}	2.86×10^{-6}	2.86×10^{-7}	2.86×10^{-8}
Max.	6.28×10^{-6}	6.29×10^{-7}	6.59×10^{-8}	6.22×10^{-6}	6.22×10^{-7}	6.22×10^{-8}
Time at max.	0.23 s	0.23 s	0.23 s	1.25 s	1.25 s	1.25 s
	ρ					
Mean avg.	5.38×10^{-5}	5.30×10^{-6}	1.68×10^{-6}	6.68×10^{-5}	6.68×10^{-6}	6.68×10^{-7}
Max.	1.14×10^{-4}	1.12×10^{-5}	2.57×10^{-6}	1.42×10^{-4}	1.42×10^{-5}	1.42×10^{-6}
Time at max.	1.25 s	1.25 s	5 s	0.23 s	0.23 s	0.23 s

7.2.3 Cases 2 & 3: Symmetric Shear & Planar Loading

The shear and planar loading cases yield similar trends in the normalised differences between the quasi-analytical and numerical solution methods, and will therefore be presented in a single section. Symmetric shear loading is defined by the deformation gradient

$$\boldsymbol{F} = \begin{bmatrix} 1 & F_{12} & 0 \\ F_{21} & 1 & 0 \\ 0 & 0 & 1 \end{bmatrix}, \tag{7.55}$$

where

$$F_{12} = F_{21} = \frac{0.1t}{5} \quad \text{with} \quad t \in [0, 5], \tag{7.56}$$

and planar loading is defined by the deformation gradient

$$F_{11} = F_{22} = 1 + \frac{t}{5}\left[1.05 - 1\right] \tag{7.57}$$

and

$$F_{12} = F_{21} = \frac{\sqrt{0.1025}t}{5} \quad \text{where} \quad t \in [0, 5]\,. \tag{7.58}$$

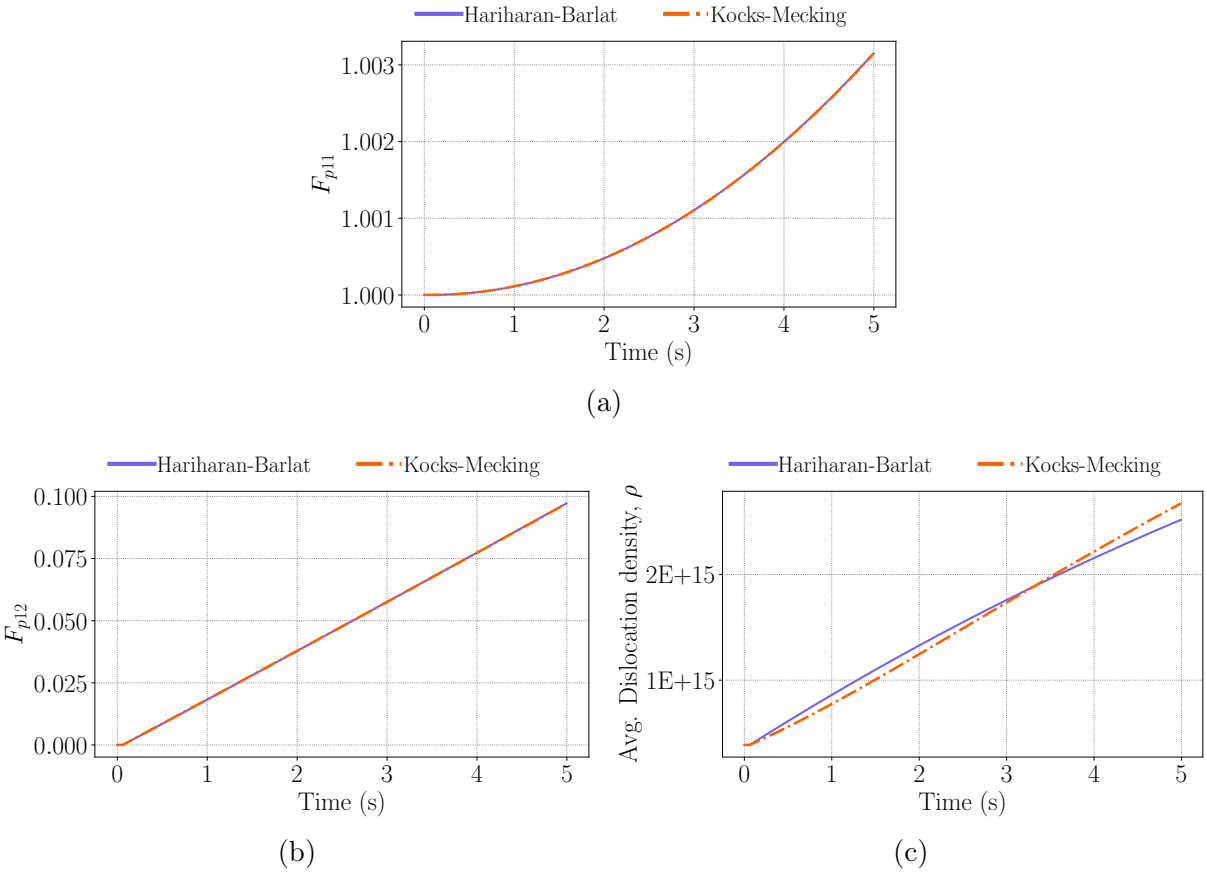

Figure 7.3: Evolution of the independent variables for shear loading: (a) F_{p11}, (b) F_{p12}, and (c) ρ.

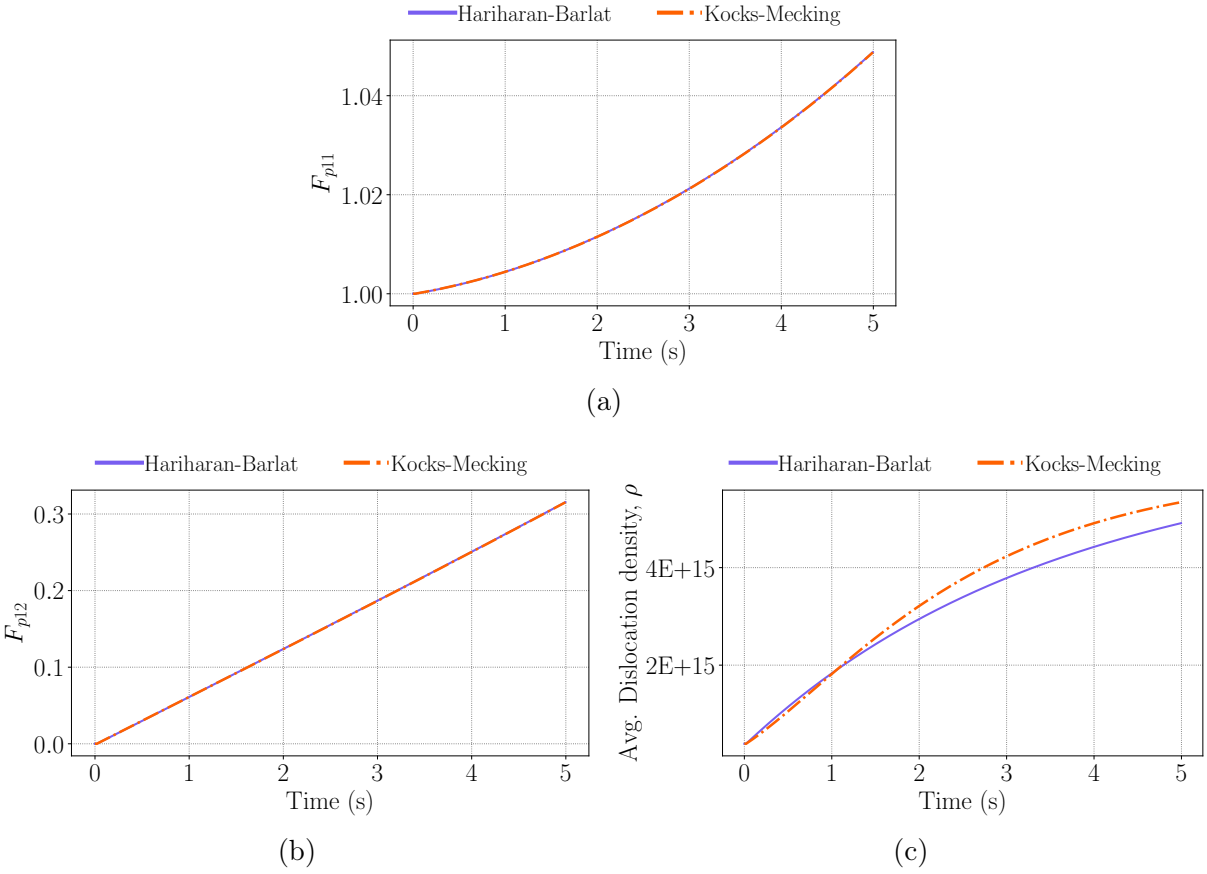

Figure 7.4: Evolution of the independent variables for planar loading: (a) F_{p11}, (b) F_{p12}, and (c) ρ.

The evolution of independent plastic deformation components and average dislocation density over time for shear loading are shown in Figure 7.3 and in Figure 7.4 for planar loading. As with the case for uniaxial loading, an examination of the independent variables, F_{p11}, F_{p12}, and ρ, plotted against time shows an imperceptible difference between the quasi-analytical and numerical solution methods at the chosen time step size. Note that the evolution of F_{p12} appears to be linear, while the evolution of F_{p11} is noticeably nonlinear.

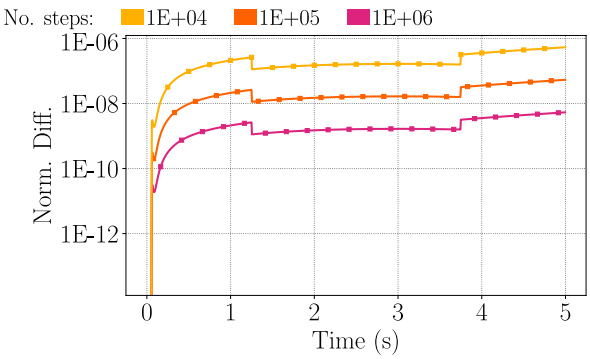

(a) F_{p11}

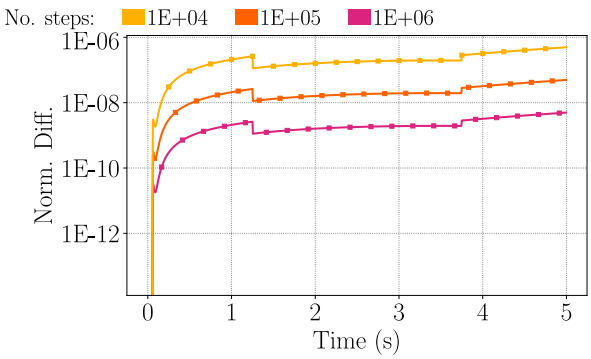

(b) F_{p11}

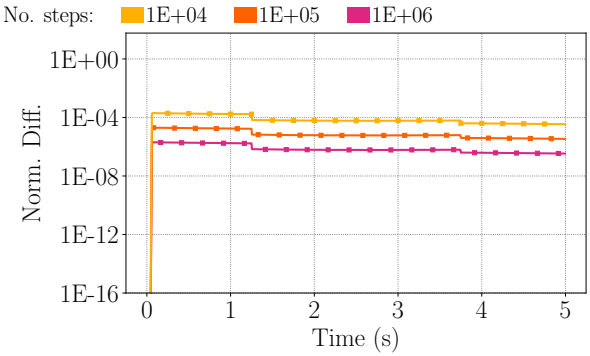

(c) F_{p12}

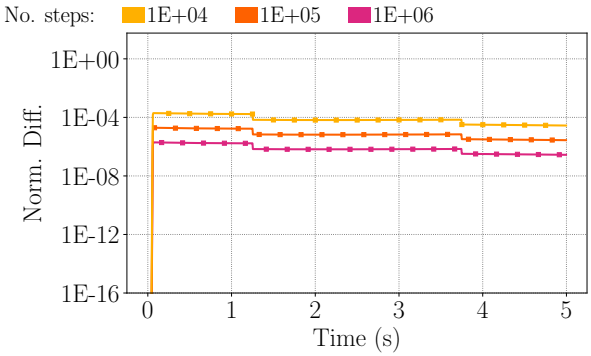

(d) F_{p12}

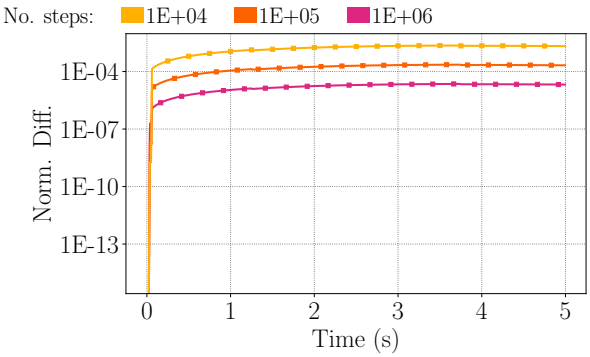

(e) ρ

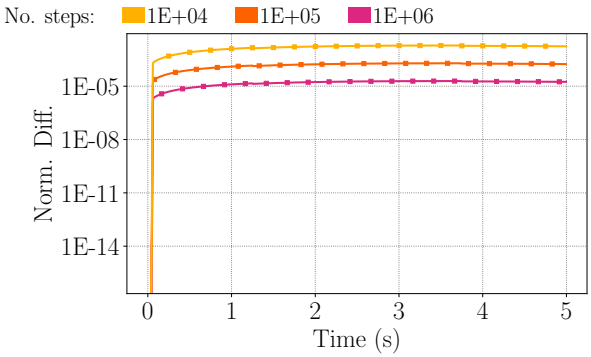

(f) ρ

Figure 7.5: The normalised differences between the quasi-analytical and numerical solution method results for the independent variables for shear loading are presented for the Kocks-Mecking model in the left column (a, c, e) and the Hariharan-Barlat model in the right column (b, d, f). The deformation occurs over 5 seconds in either 10^4, 10^5, or 10^6 steps.

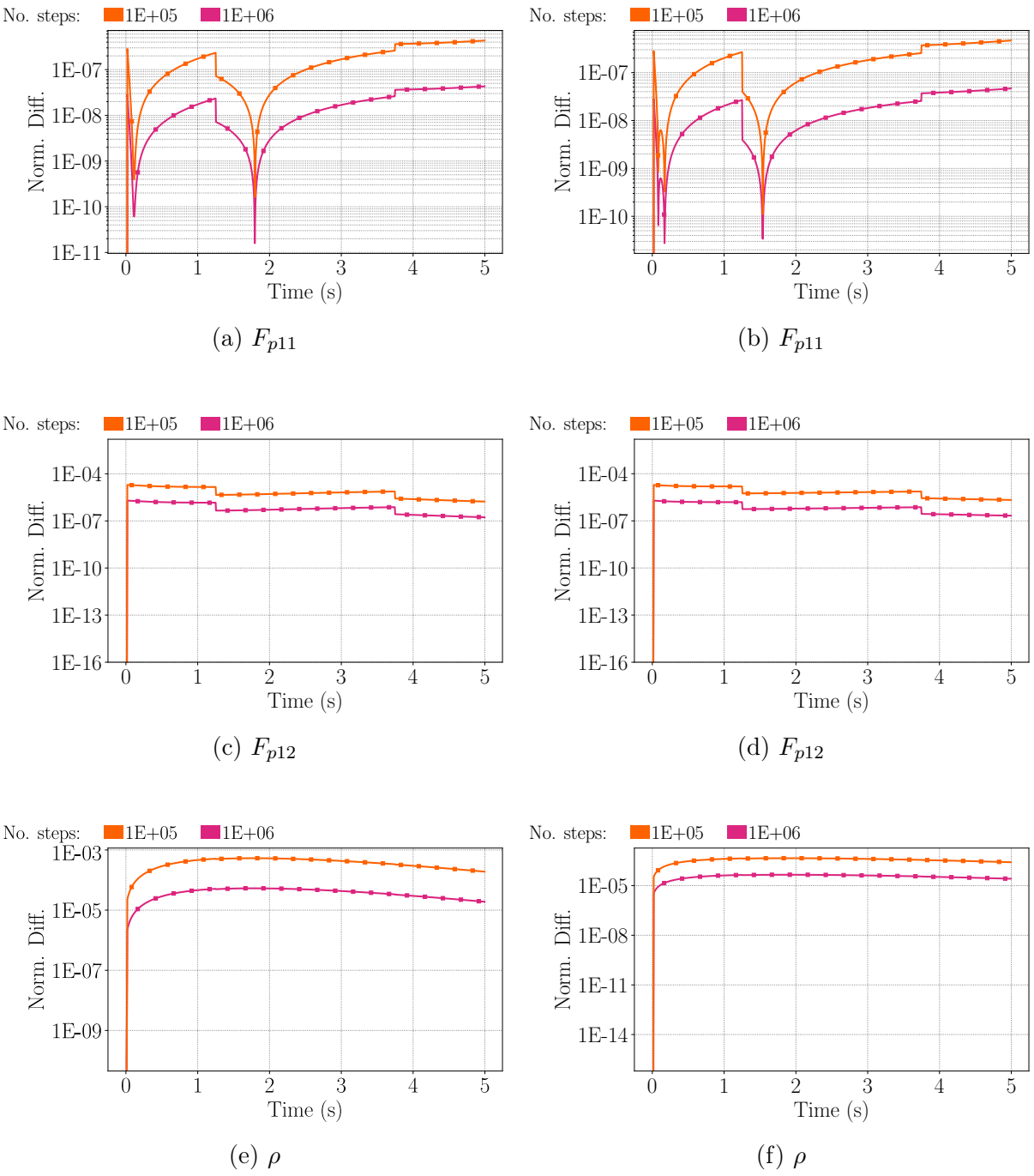

Figure 7.6: The normalised differences between the quasi-analytical and numerical solution method results for the independent variables for planar loading are presented for the Kocks-Mecking model in the left column (a, c, e) and the Hariharan-Barlat model in the right column (b, d, f). The deformation occurs over 5 seconds in either 10^5 or 10^6 steps.

The normalised differences between the quasi-analytical and numerical solution methods for each dislocation density evolution model are shown in Figure 7.5 for shear loading and in Figure 7.6 for planar loading. The mean average and maximum normalised differences for each time step size and dislocation density evolution model are recorded in Tables 7.3 and 7.4 for shear and planar loading at the end of this section, respectively. The differences between the two solution methods decrease over the course of loading for ρ and

F_{p12}. However, the normalised differences for F_{p11} increase over the course of loading with the maximum difference occurring at the end of the simulation. A thorough investigation into the cause of this difference is precluded by time constraints. An oscillation of the normalised differences for F_{p11} for all time step sizes is evident in Figures 7.5a-b and 7.6a-b; however, both the maximum and mean average values of the normalised differences are significantly smaller than those for F_{p12} and ρ.

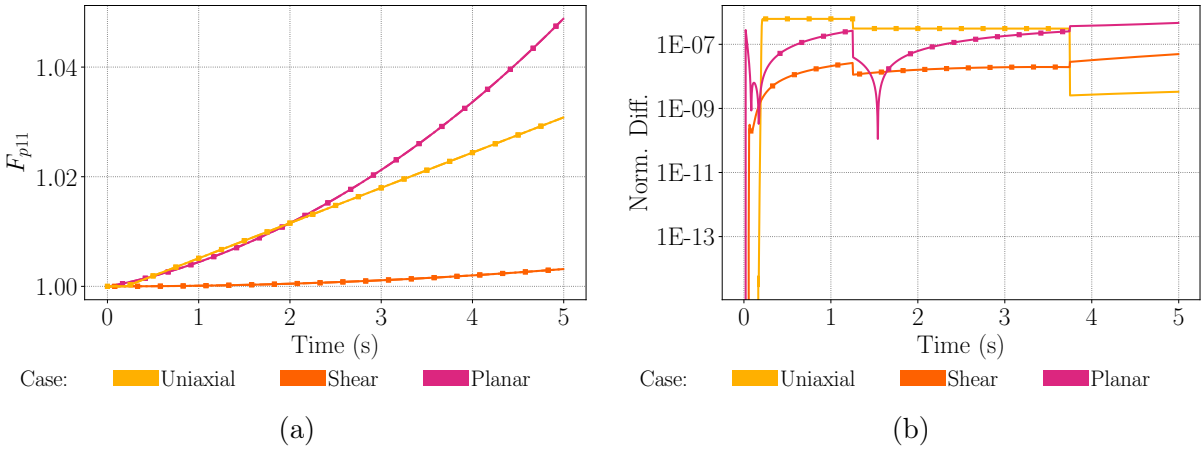

Figure 7.7: A comparison the evolution of F_{p11} for each loading case and the associated normalised differences: (a) F_{p11}, (b) normalised differences.

Comparisons of the evolution of F_{p11} and the normalised differences between the two methods are presented in Figure 7.7. Of the three loading cases, only the normalised differences for uniaxial loading decrease over time in Figure 7.7b. The noticeable difference between the uniaxial case and the shear and planar cases is that F_{p11} appears to evolve more linearly in Figures 7.1a and 7.7a, while the shear loading case results in a low magnitude, nonlinear increase, and the planar loading case results in a high magnitude, nonlinear increase. The maximum normalised differences between the quasi-analytical and numerical solution methods appears to increase with the magnitude and nonlinearity of the evolution of F_{p11}.

Table 7.3: Maximum and mean average normalised differences between the quasi-analytical and numerical solution method results for the independent variables for shear loading.

	Kocks-Mecking			Hariharan-Barlat		
No. time steps	10^4	10^5	10^6	10^4	10^5	10^6
Norm. Diff.			F_{p11}			
Mean avg.	2.13×10^{-7}	2.13×10^{-8}	2.13×10^{-9}	2.13×10^{-7}	2.12×10^{-8}	2.12×10^{-9}
Max.	5.35×10^{-7}	5.34×10^{-8}	5.34×10^{-9}	4.95×10^{-7}	4.94×10^{-8}	4.96×10^{-9}
Time at max.	5.0 s	5.0 s	5.0 s	5.0 s	5.0 s	5.0 s
			F_{p12}			
Mean avg.	8.29×10^{-5}	8.29×10^{-6}	8.33×10^{-7}	8.35×10^{-5}	8.35×10^{-6}	8.35×10^{-7}
Max.	1.99×10^{-4}	1.99×10^{-5}	2.00×10^{-6}	1.96×10^{-4}	1.96×10^{-5}	1.96×10^{-6}
Time at max.	0.007 s	0.007 s	0.007 s	0.007 s	0.007 s	0.007 s
			ρ			
Mean avg.	1.69×10^{-3}	1.69×10^{-4}	1.67×10^{-5}	1.57×10^{-3}	1.56×10^{-4}	1.56×10^{-5}
Max.	2.28×10^{-3}	2.28×10^{-4}	2.25×10^{-5}	1.94×10^{-3}	1.94×10^{-4}	1.94×10^{-5}
Time at max.	3.75 s	3.75 s	3.75 s	3.57 s	3.58 s	3.58 s

Table 7.4: Maximum and mean average normalised differences between the quasi-analytical and numerical solution method results for the independent variables for planar loading.

	Kocks-Mecking		Hariharan-Barlat	
No. time steps	1×10^5	1×10^6	1×10^5	1×10^6
Norm. Diff.	F_{p11}			
Mean avg.	1.80×10^{-7}	1.80×10^{-8}	1.93×10^{-7}	1.93×10^{-8}
Max.	4.33×10^{-7}	4.32×10^{-8}	4.66×10^{-7}	4.65×10^{-8}
Time at max.	5.0 s	5.0 s	5.0 s	5.0 s
	F_{p12}			
Mean avg.	7.35×10^{-6}	7.35×10^{-7}	7.80×10^{-6}	7.80×10^{-7}
Max.	1.96×10^{-5}	1.96×10^{-6}	1.93×10^{-5}	1.93×10^{-6}
Time at max.	0.003 s	0.003 s	0.002 s	0.003 s
	ρ			
Mean avg.	3.76×10^{-4}	3.75×10^{-5}	3.65×10^{-4}	3.65×10^{-5}
Max.	5.32×10^{-4}	5.32×10^{-5}	4.55×10^{-4}	4.55×10^{-5}
Time at max	1.78 s	1.78 s	1.89 s	1.89 s

7.3 Discussion

The overall normalised differences between the quasi-analytical and numerical solution methods are negligible for all the loading cases and time step sizes presented in Section 7.2. While the quasi-analytical solution method is used to verify the numerical solution method, the quasi-analytical method itself employs some numerical approximation with associated approximation errors. This is most evident in the increasing normalised differences between the two solution methods for the nonlinear evolution of F_{p11}. In these cases, the errors are small enough that it is reasonable to attribute these differences to differences in the numerical approximation rather than a fundamental error in the implementation of either solution method.

The differences between the quasi-analytical and numerical solution methods are negligibly small; therefore, it is assumed that the results computed at similar time step sizes that follow in Chapter 8 are sufficiently accurate.

Chapter 8

Dislocation Density-Based Constitutive Model Behaviour

The ability of the finite-strain constitutive model to capture work hardening behaviour under multiaxial loading conditions is explored in this chapter. The quasi-static loading results are presented in two sections: the first concerns the determination of the dislocation density evolution equation parameters and the degree to which varying these parameters affects the solutions, and the second section concerns the extensibility of the finite-strain constitutive model to various forms of loading within a multiaxial framework. As a distinct aspect of the model's behaviour is addressed in each section, the discussion for each section will follow at the end of the section, rather than in a combined discussion at the end of the chapter.

In the first section, Section 8.1, the results of material parameter determination are structured as follows: the methodologies used to determine and then vary the dislocation density evolution equation parameters are outlined in Section 8.1.1 and Section 8.1.2, respectively, followed by a summary of their results in Section 8.1.3 and a discussion in Section 8.1.4

The parameters determined in Section 8.1 are used in obtaining the quasi-static loading results presented in the second section, Section 8.2. Three quasi-static loading cases are examined: uniaxial loading in Section 8.2.2, plane-strain compression loading in Section 8.2.3, and shear loading in Section 8.2.4. A discussion of the quasi-static loading results follows in Section 8.2.5.

8.1 Material Parameters

The material parameters for two aluminium alloys are determined in this section, followed by a brief qualitative investigation of the effect their variation has on the predicted work hardening behaviour. Two aluminium alloys are used to demonstrate the behaviour of

the constitutive model in this work. Experimental data for AA5032-T4 [27], [28] and AA5052-O [65] is used to determine the dislocation storage and dislocation annihilation parameters for the Hariharan-Barlat and Kocks-Mecking dislocation density evolution equations, which are presented in Section 8.1.1. This experimental data is used to verify the implementation of the dislocation density evolution equations as the suitability of these equations for modelling these experiments has been demonstrated in the literature from which the data is sourced. A short examination of the variation of these parameters follows in Section 8.1.2.

8.1.1 Parameter Determination

From Chapter 4, recall that the hardening rates, Θ, for the Kocks-Mecking and Hariharan-Barlat dislocation density evolution equations are given by Equations (8.1) and (8.2), respectively:

$$\text{KMM:} \qquad \Theta = \theta_0 - \beta_0 \tau_f, \tag{8.1}$$

$$\text{HBM:} \qquad \Theta = \frac{Mk\gamma_0^2}{2\tau_f}\left[1 - \exp\left(-\psi\frac{\tau_f}{\gamma_0}\right)\right] - \frac{Mk_2\tau_f}{2}, \tag{8.2}$$

where $\theta_0 = \alpha\mu b M^2 k_1/2$, $\beta_0 = Mk_2/2$, and $\gamma_0 = M\alpha\mu b$. In both equations, k_2 is assumed to be constant throughout plastic deformation. The parameters for each dislocation density evolution equation are found by fitting the appropriate hardening rate equation to hardening rate-flow stress experimental data using a least-squares approach.

8.1.2 Parameter Variation

There are several sophisticated statistical methods that may be employed for the design of experiments and variance analysis [66], but the intention of this computational experiment is neither to optimize the parameters nor provide a detailed sensitivity analysis. Rather, this experiment is conducted to

(i) verify that each parameter affects the hardening rate in a manner that is consistent with the microstructural mechanisms that ostensibly inform the parameter, and

(ii) to ensure that the dislocation density evolution equations are not so sensitive to parameter perturbations that small errors in their determination from experimental data will render the equation useless.

Therefore, the parameter variation experiment is designed to facilitate a qualitative analysis.

To elucidate the effect of each parameter on the hardening rate, the parameters are varied according to a Taguchi orthogonal array. Briefly, Taguchi orthogonal arrays are

used to limit the number of experiments required to observe the effect of parameter variation. The arrays are constructed based on the mathematical theory of difference sets and factorial designs, and a thorough explanation on these theories can be found in [67].

Table 8.1: Taguchi orthogonal arrays to assess the effect of variation of the Kocks-Mecking and Hariharan-Barlat parameters.

	Kocks-Mecking		Hariharan-Barlat		
Test	k_1	k_2	k	k_2	ψ
1	N	N	N	N	N
2	N	L	N	L	L
3	N	H	N	H	H
4	L	N	L	N	L
5	L	L	L	L	H
6	L	H	L	H	N
7	H	N	H	N	H
8	H	L	H	L	N
9	H	H	H	H	L

The variation of each parameter is denoted in Table 8.1 by N (neutral), L (low), or H (high), where N indicates that the parameter is not varied from the value determined in Section 8.1.1, L indicates that the parameter is decreased by 5%, and H indicates that the parameter is increased by 5%. The maximum hardening rate and the maximum flow stress is recorded for each test to provide metrics for comparison of the predicted material behaviour.

8.1.3 Results

First, the material parameters for the dislocation density evolution equations are determined, and then the effect of their variation is examined.

Parameter Determination

Using AA5032-T4 [27] and AA5052-O [65] experimental data, the hardening rate equation for each dislocation density evolution equation is fitted to the experimental data for each alloy. The fitted hardening rate curves are plotted against the experimental data in Figure 8.1. The parameters determined during this procedure are listed in Table 8.2.

Table 8.2: Parameter values used in this work, as determined by least-squares analysis

	Kocks-Mecking		Hariharan-Barlat		
Alloy	k_1	k_2	k	k_2	ψ
AA5032-T4	3.0373×10^8	3.9213	6.7938×10^{15}	1.0633	0.0668
AA5052-O	3.9120×10^8	9.1372	5.2102×10^{15}	2.2504	0.6000

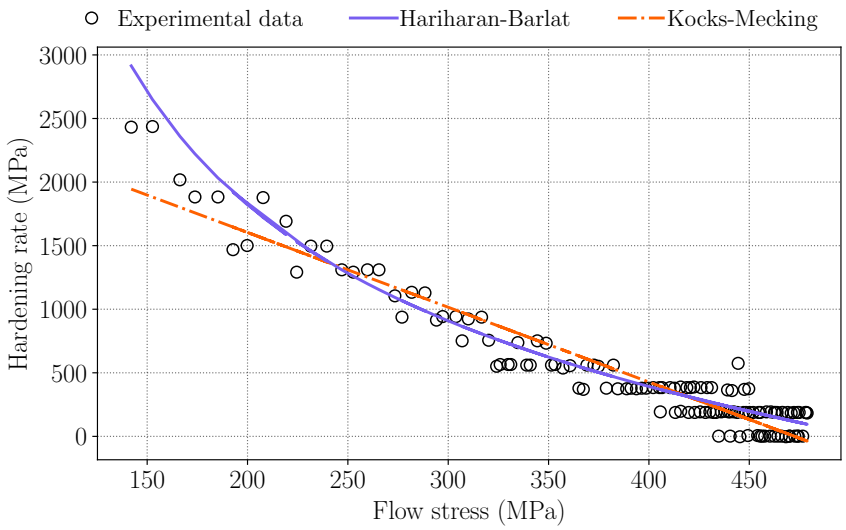

(a)

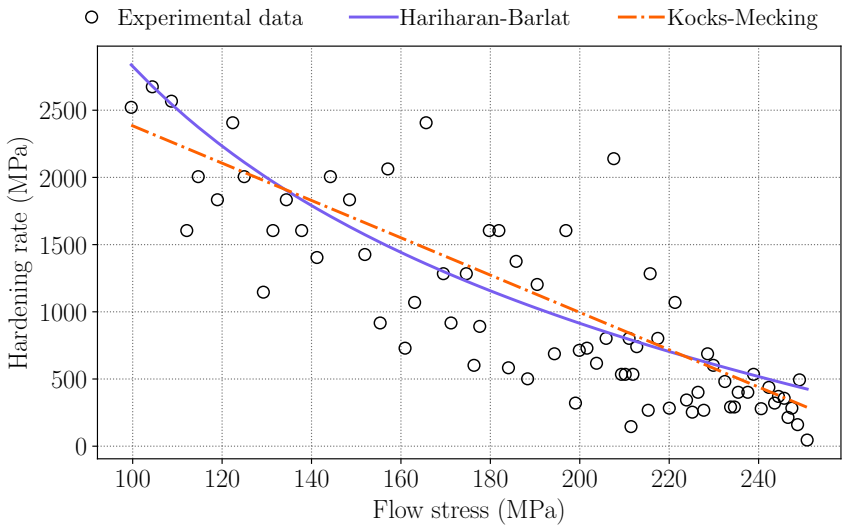

(b)

Figure 8.1: The hardening rate equation for each dislocation density evolution equation is plotted against the experimental data for (a) AA5032-T4 [27] and (b) AA5052-O [65]. A hardening rate-flow stress plot provides the clearest demonstration of the key difference between the Hariharan-Barlat and Kocks-Mecking dislocation density evolution equations; note the nonlinearity of the Hariharan-Barlat hardening rate.

Parameter Variation

Recall from Chapter 4 that the dislocation density evolution equation parameters represent the underlying mechanisms that drive the competing processes of

(i) dislocation storage, which increases the rate of work hardening, is captured by k_1 (KMM) and k (HBM),

(ii) and dislocation annihilation, which leads to dynamic recovery and a decrease in the rate of work hardening, is captured by k_2 in both models.

Table 8.3: Summary of parameter variation results for AA5032-T4

Kocks-Mecking Parameters				
	k_1	k_2		Value
Baseline hardening rate	N	N		2453 MPa
Lowest maximum hardening rate	L	H		2253 MPa
Highest maximum hardening rate	H	L		2652 MPa
Baseline flow stress	N	N		470 MPa
Lowest maximum flow stress	L	H		426 MPa
Highest maximum flow stress	H	L		519 MPa
Hariharan-Barlat Parameters				
	k	k_2	ψ	Value
Baseline hardening rate	N	N	N	3443 MPa
Lowest maximum hardening rate	L	H	N	3258 MPa
Highest maximum hardening rate	H	L	N	3626 MPa
Baseline flow stress	N	N	N	472 MPa
Lowest maximum flow stress	L	H	N	450 MPa
Highest maximum flow stress	H	L	N	493 MPa

Therefore, the parameter variation combinations that result in the highest and lowest work hardening rates are of most interest. The parameter variation combination that yields the highest and lowest values are summarised in Table 8.3. The results for AA5032-T4 alone are sufficient for the demonstrative purposes of this variation experiment as the effect of parameter variation on AA5052-O is similar.

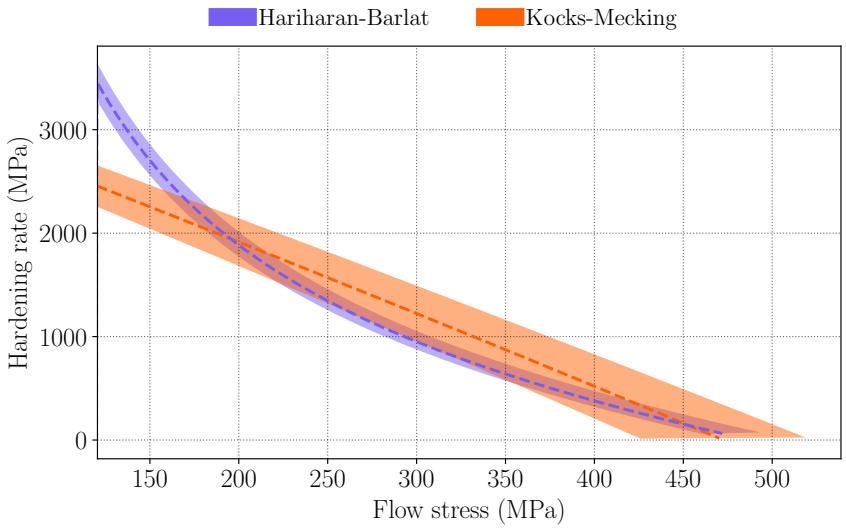

(a)

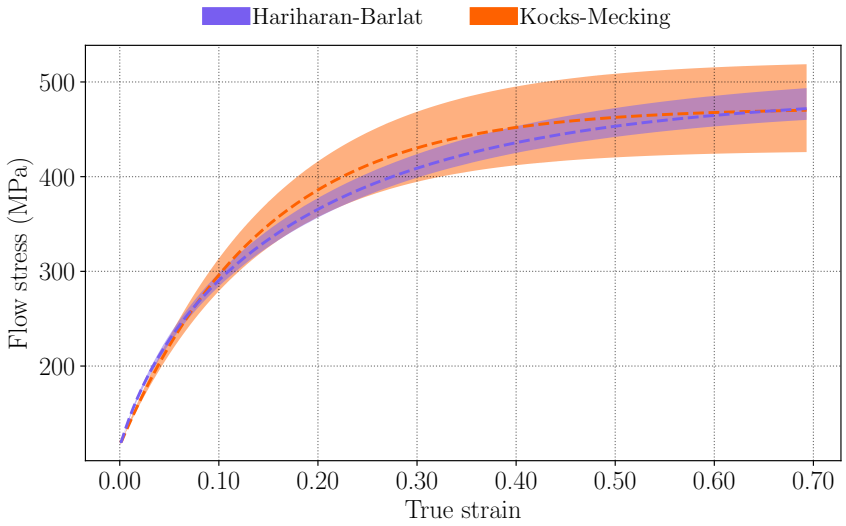

(b)

Figure 8.2: The range of work hardening behaviour of AA5032-T4 possible from a ±5% parameter variation is demonstrated in (a) a hardening rate vs flow stress plot and (b) a stress-strain curve. A dashed line at the centre of each curve indicates the material behaviour predicted by the model when using the parameter values determined in Section 8.1.1. The upper and lower bound of the shaded area are informed by the combination of the parameters that yield the maximum and minimum values, respectively, for (a) work hardening rate and (b) flow stress.

The range of all possible work hardening behaviour of AA5032-T4 from a ±5% parameter variation is demonstrated in Figure 8.2.

8.1.4 Discussion

It is evident from the results summarised in Table 8.3 that an increase in the k_1 and k parameters has an overall effect of increasing the hardening rate. The highest maximum hardening rate is achieved by increasing the dislocation storage parameters, and decreasing the dislocation annihilation parameters. Conversely, the lowest hardening rates and flow stresses are achieved by weighting the dislocation density evolution equations in favour of the dislocation annihilation parameter. The effects of these parameters are confirmed by their isolated variations, although these results are omitted for brevity. Thus, it is confirmed that the material parameters affect the work hardening behaviour as intended.

Importantly, it is demonstrated that small variations in the material parameters do not result in drastically different material behaviour that would limit the constitutive model's utility. This is an important finding as parameters that are fit to noisy or sparse data are susceptible to some degree of inaccuracy. It is, therefore, beneficial to employ a constitutive model that is not extremely sensitive to outliers or the sparsity of the dataset to which the parameters are fit.

8.2 Quasi-Static Loading Cases

In this section, the dislocation density evolution equation parameters determined in Section 8.1 are applied to the finite-strain constitutive model presented in Chapter 6, and the behaviour of the model is examined in three loading scenarios: uniaxial loading in Section 8.2.2, plane-strain compression loading in Section 8.2.3, and shear loading in Section 8.2.4. While the models developed can capture rate-dependence, a single rate is used for these scenarios so that rate effects do not obscure those stemming from the scenario under consideration. A discussion of the quasi-static loading results follows in Section 8.2.

8.2.1 Scalar Strain Measures

Several figures are used to demonstrate the mechanical behaviour of a material in the sections that follow. The abscissa of these figures is typically either *true strain*, which is calculated from the deformation gradient

$$\text{true strain} := \ln\left(F_{11}\right), \tag{8.3}$$

or *shear strain*, which is defined as the reduction in the angle between two line elements that were orthogonal in the material domain,

$$\text{shear strain} := \arcsin\left(\frac{C_{12}}{\lambda_1\lambda_2}\right). \tag{8.4}$$

In the loading cases that follow, all uniaxial extension occurs in the $\boldsymbol{e}_1$ direction, and all shear occurs between the $\boldsymbol{e}_1$ and $\boldsymbol{e}_2$ directions. Therefore, the strain abscissa always reflects the true strain in the $\boldsymbol{e}_1$ direction, or the shear strain between the $\boldsymbol{e}_1$ and $\boldsymbol{e}_2$ directions, accordingly.

8.2.2 Uniaxial Loading

Uniaxial loading is defined as an applied load along a single axis such that resulting stress tensor has the form

$$\boldsymbol{\tau} = \text{diag}\begin{bmatrix}\tau_{11} & 0 & 0\end{bmatrix}. \tag{8.5}$$

For an isotropic material, the associated deformation gradient is given by

$$\boldsymbol{F} = \text{diag}\begin{bmatrix}\lambda_1 & \lambda_2 & \lambda_3\end{bmatrix} \tag{8.6}$$

where

$$\lambda_1 = 1 + \frac{t}{5}\left[1.05 - 1\right] \quad \text{with} \quad t \in [0, 5]. \tag{8.7}$$

where $\lambda_2 \neq 1$, $\lambda_3 \neq 1$ where $t > 0$, and $\lambda_2 = \lambda_3$ for an isotropic material.

Monotonic Loading

Monotonic uniaxial loading describes either tensile or compressive loading that occurs in one direction, i.e loading that is not reversed. The parameters for the Hariharan-Barlat and Kocks-Mecking material parameters for AA5052-O and AA5032-T4 determined in Section 8.1.3 are used in the material point-level numerical implementation of the elasto-plasticity constitutive model in an attempt to replicate the uniaxial loading conditions in [27] and [65].

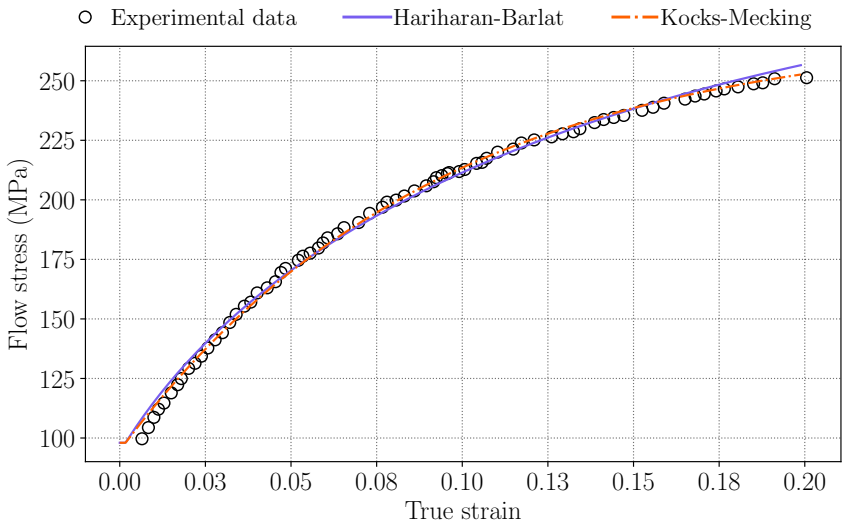

(a)

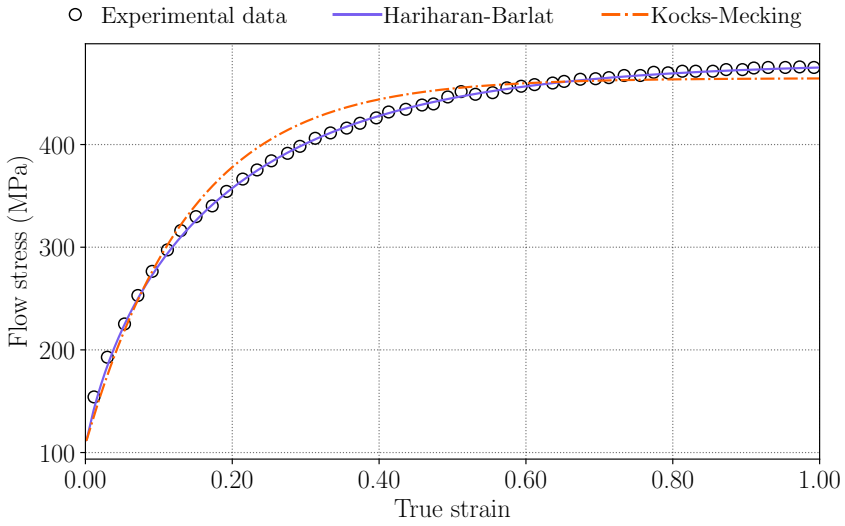

(b)

Figure 8.3: Uniaxial tensile loading at a strain rate of 0.05 s^{-1} of (a) AA5052-O [65] (b) AA5032-T4. [27]

The results of this simulation are presented in Figure 8.3. Although the intention of this work is not to provide a comparative analysis of the Hariharan-Barlat and Kocks-Mecking dislocation density evolution equations, the advantage of the nonlinear Hariharan-Barlat equation is evident in Figure 8.3b, where the Hariharan-Barlat-based constitutive model follows the experimental data more closely than the Kocks-Mecking-based model. This difference is less evident in Figure 8.3a, where the final strain is only at 20% of the total strain in Figure 8.3b.

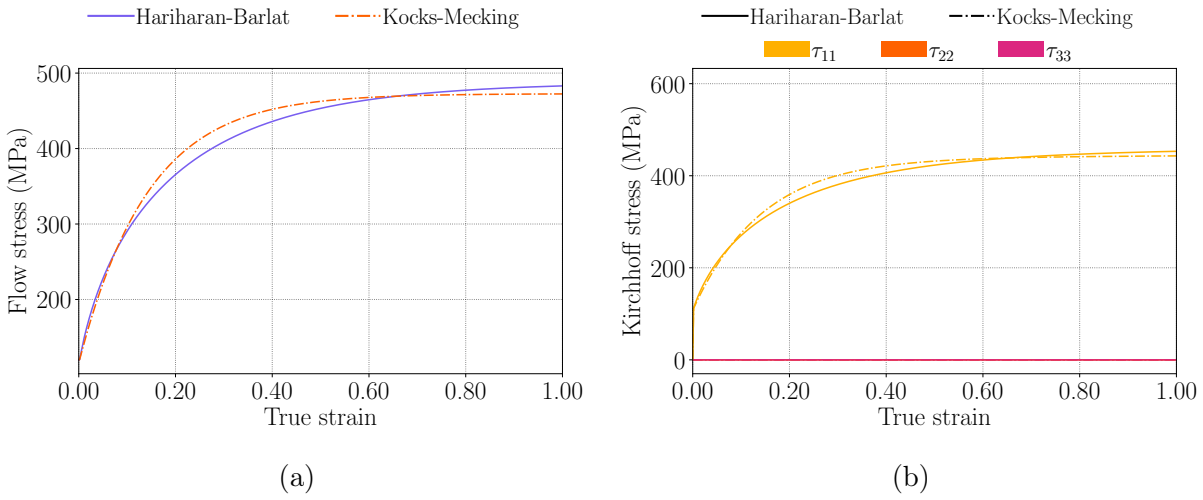

Figure 8.4: (a) Flow stress-true strain and (b) Kirchhoff stress-true strain curves for uniaxial tensile loading at strain rate of 0.05 s^{-1} of AA5032-T4 [27] from the finite-strain elastoplasticity model.

As the elastoplasticity model is multiaxial, it is possible to examine the Kirchhoff stress in three directions. The diagonal components of the Kirchhoff stress are plotted against true strain alongside in Figure 8.4b. Given that loading occurs in the $\boldsymbol{e}_1$ direction, τ_{11} is the only non-zero stress component.

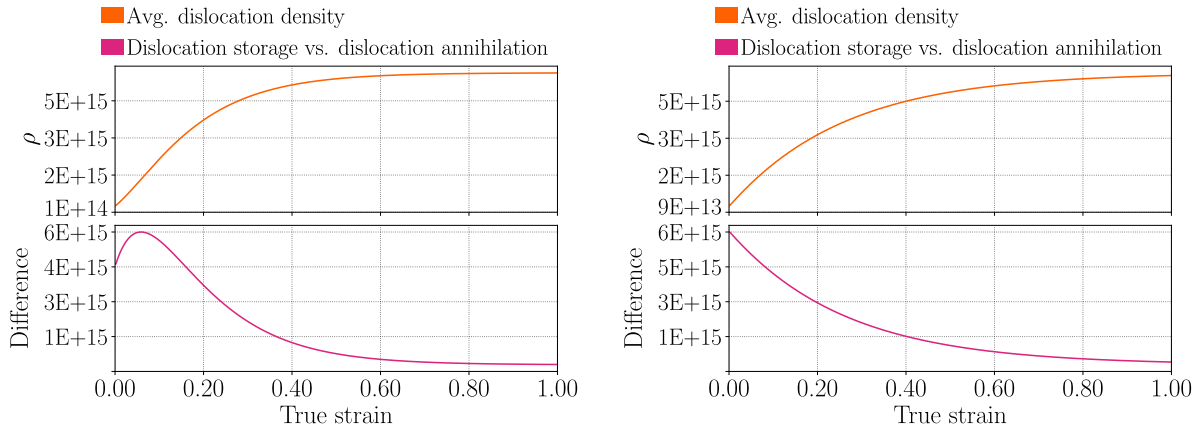

Figure 8.5: The average dislocation density and the difference between the dislocation storage and annihilation terms as determined by the (a) Kocks-Mecking model and (b) Hariharan-Barlat model for uniaxial tensile loading at strain rate of 0.05 s^{-1} of AA5032-T4 [27]. The difference between the dislocation and annihilation terms is determined according to Equation (8.8).

The evolution of average dislocation density and the difference between the dislocation storage and annihilation terms in Equations (4.3) and (4.9) is given in Figure 8.5 for the loading case in Figure 8.4a. The difference is calculated accordingly:

$$\text{Difference} = \begin{cases} k_1\sqrt{\rho} - k_2\rho & \text{(KMM)} \\ k\left[1 - \exp\left(-\psi\sqrt{\rho}\right)\right] - k_2\rho & \text{(HBM).} \end{cases} \tag{8.8}$$

Therefore, a large, positive difference indicates that dislocation storage is the dominating process, while a negative difference indicates that the dominating process is dislocation annihilation. Both the Hariharan-Barlat and Kocks-Mecking models yield a monotonic increase of average dislocation density in Figure 8.5 which concurs with the work hardening behaviour seen in Figure 8.4a. However, a continuously decreasing difference between the dislocation processes is reflected by the Hariharan-Barlat model in Figure 8.5b, while the Kocks-Mecking model reflects an initial increase in the dominance of dislocation storage in Figure 8.5a. The decreasing difference between the dislocation storage and annihilation terms indicates the onset of Stage III work hardening, also known as dynamic recovery, which is expected for aluminium in this strain regime. The later onset of the dynamic recovery in Figure 8.5a is observed in the flow stress-strain curve in Figure 8.4a as the flow stress computed via the Kocks-Mecking model overshoots the experimental data.

Cyclical loading

A cyclical uniaxial loading test is defined by cycling through two stages of deformation that are defined by a prescribed $\boldsymbol{F}_{\text{end}}$ where

$$\boldsymbol{F}_{\text{end}} = \text{diag}\begin{bmatrix}\lambda_1 & \lambda_2 & \lambda_3\end{bmatrix} \tag{8.9}$$

and, for the case that follows, where

$$\lambda_1 = \begin{cases} 1 + \frac{t}{5}\left[1.05 - 1\right] & \text{for } 0 < t < 1 \\ 1.05 + \frac{t}{5}\left[0.95 - 1\right] & \text{for } 1 < t < 2, \end{cases} \tag{8.10}$$

and $\lambda_2 \neq 1$, $\lambda_3 \neq 1$ where $t > 0$, and $\lambda_2 = \lambda_3$.

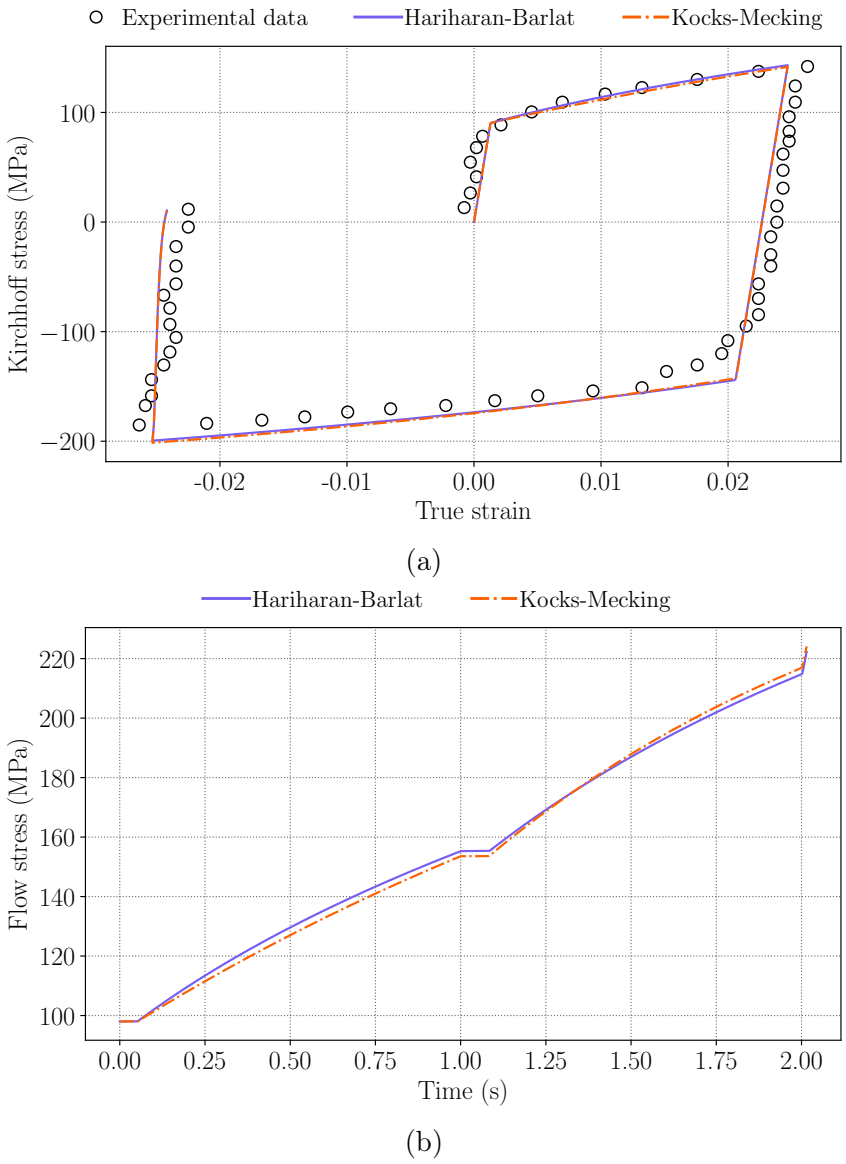

Figure 8.6: A single cycle of tension to compression of AA5052-O [65] is used to demonstrate the current ability of the constitutive model to capture cyclical loading in (a) a Kirchhoff stress-true strain curve, and (b) a plot of the flow stress over time.

A preliminary attempt to capture the mechanical behaviour of AA5052-O [65] under cyclical loading is shown in Figure 8.6. The hardening behaviour seen in the experimental data appears to be largely isotropic in Figure 8.6a; however, the Kirchhoff stress computed with the constitutive model exceeds the experimental data in compression. The computed flow stress maintains a relatively equal rate of increase over time in both tension and compression in Figure 8.6b.

8.2.3 Plane-Strain Compression

Plane-strain compression loading is prescribed by a deformation gradient that has the form

$$\boldsymbol{F} = \mathrm{diag}\begin{bmatrix}\lambda_1 & \lambda_2 & 1\end{bmatrix}, \tag{8.11}$$

and a stress tensor that has the form

$$\boldsymbol{\tau} = \mathrm{diag}\begin{bmatrix}\tau_{11} & 0 & \tau_{33}\end{bmatrix}. \tag{8.12}$$

The stretches λ_1 and $\lambda_3 = 1$ are controlled, and λ_2 is found by enforcing $\tau_{22} = 0$.

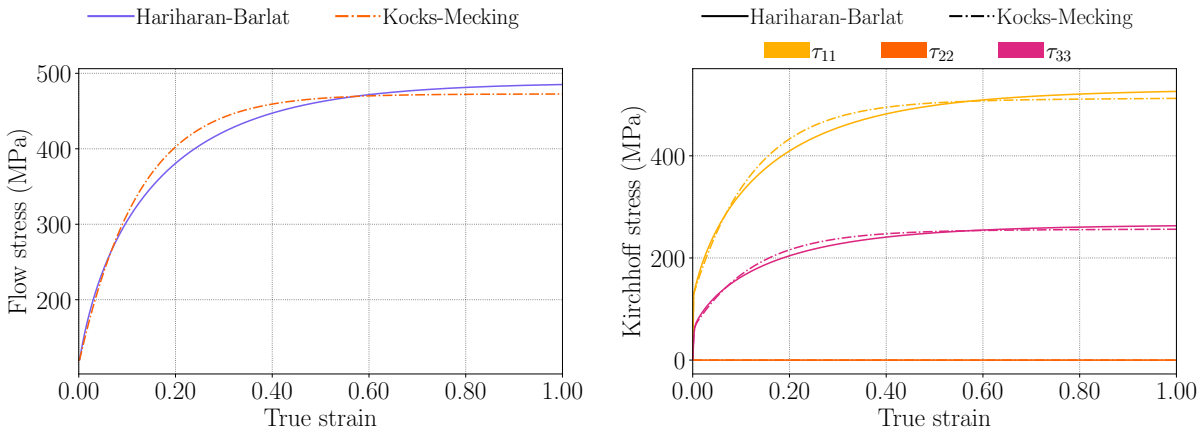

Figure 8.7: Plane-strain compression of AA5032-T4 [27] at a strain rate of 0.05 s^{-1} represented in (a) a flow stress-true strain and (b) Kirchhoff stress-true strain curves.

A flow stress-strain curve is presented for plane-strain compression in Figure 8.7a, but of more significance is the multiaxial Kirchhoff stress-strain curve in Figure 8.7b. Both τ_{11} and τ_{33} are nonzero, and $\tau_{22} = 0$ in line with the definition of this loading case.

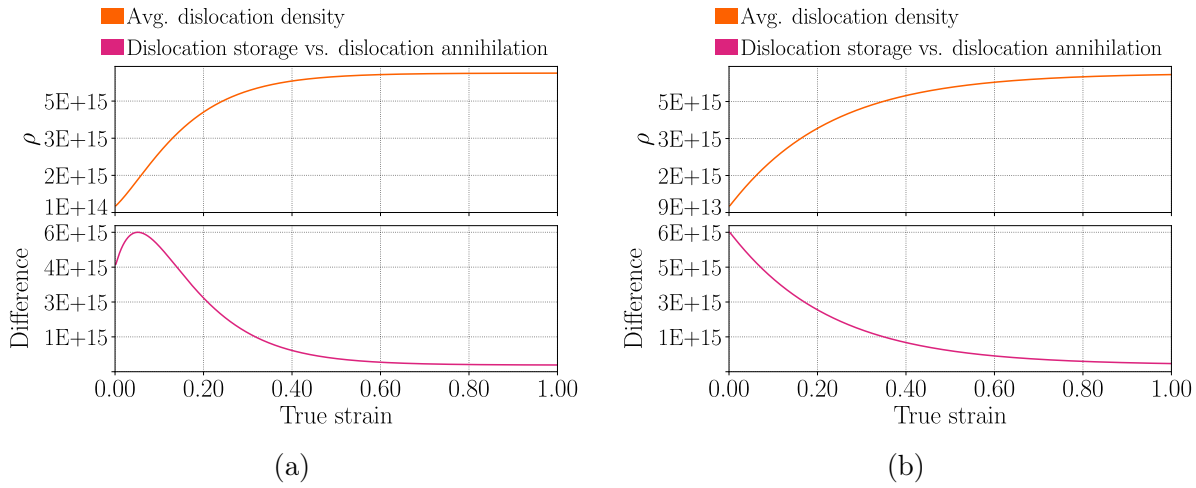

Figure 8.8: The average dislocation density and the difference between the dislocation storage and annihilation terms as determined by the (a) Kocks-Mecking model and (b) Hariharan-Barlat model for plane-strain compression at strain rate of 0.05 s^{-1} of AA5032-T4 [27]. The difference between the dislocation and annihilation terms is determined according to Equation (8.8).

The average dislocation density evolution for plane-strain compression progresses similarly to the uniaxial loading case in Figure 8.5, which is to be expected as the flow stress-true strain curve in Figure 8.7a closely matches the uniaxial curve in Figure 8.4a.

8.2.4 Shear Loading

Consideration of shear effects is required to demonstrate the suitability of the models in a multiaxial setting. While appropriate comparison data were not identified, these effects are most directly assessed by considering idealised simple shear. Simple shear loading is defined as an applied displacement parallel to the $\boldsymbol{e}_1$ axis that linearly increases with distance from that axis. In an isotropic material, such a deformation can be caused by a surface traction on a surface parallel to the the $\boldsymbol{e}_1$ axis of the material point. The resulting deformation is defined by the deformation gradient

$$\boldsymbol{F} = \begin{bmatrix} 1 & \gamma & 0 \\ 0 & 1 & 0 \\ 0 & 0 & 1 \end{bmatrix}, \tag{8.13}$$

where

$$\gamma = \frac{0.05t}{5} \quad \text{where } t \in [0, 20]. \tag{8.14}$$

The resulting Kirchhoff stress tensor takes the form

$$\boldsymbol{\tau} = \begin{bmatrix} \tau_{11} & \tau_{12} & 0 \\ \tau_{21} & 0 & 0 \\ 0 & 0 & 0 \end{bmatrix}. \tag{8.15}$$

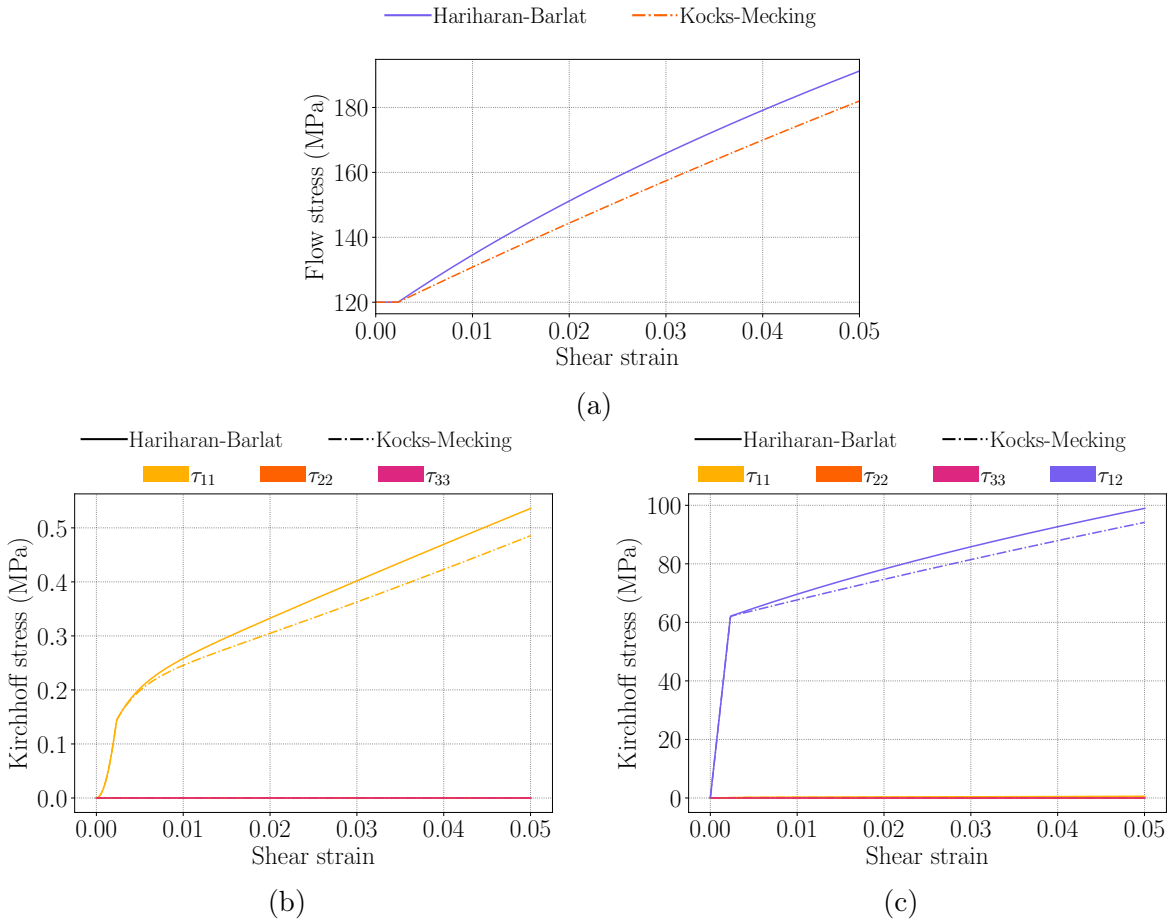

Figure 8.9: Simple shear loading of AA5032-T4 [27] at a strain rate of 0.05 s^{-1} represented in (b) a flow stress-true strain and (c, b) Kirchhoff stress-true strain curves.

Neither the Kocks-Mecking nor Hariharan-Barlat dislocation density evolution models were developed for shear loading, but the overall trends in Figure 8.9c concur with trends seen in the literature for other aluminium alloys [68], [69] where the strain hardening rates observed in shear stress-shear strain curves are generally positive in this strain regime.

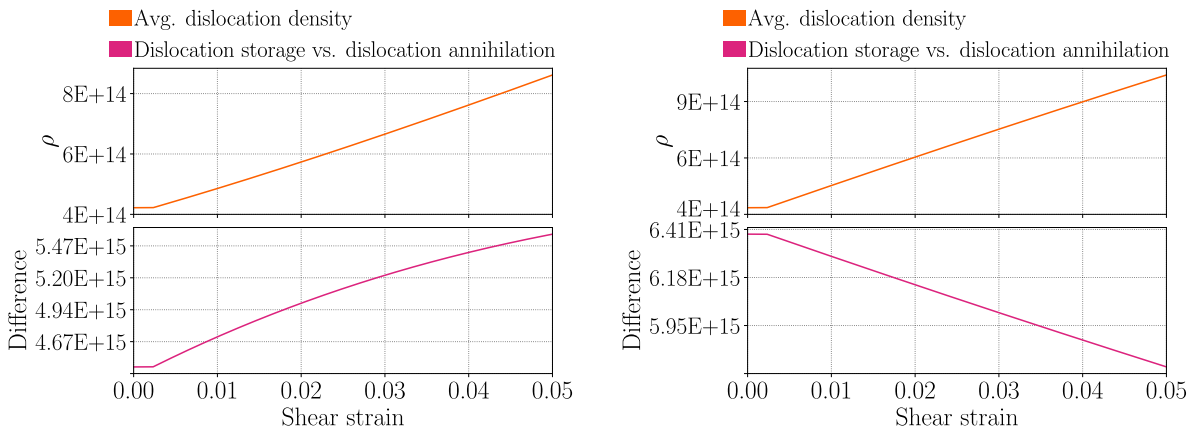

Figure 8.10: The average dislocation density and the difference between the dislocation storage and annihilation terms as determined by the (a) Kocks-Mecking model and (b) Hariharan-Barlat model for simple shear at strain rate of 0.05 s^{-1} of AA5032-T4 [27]. The difference between the dislocation and annihilation terms is determined according to Equation (8.8).

Although the evolution of average dislocation density and the difference between the annihilation and storage processes appear to differ from the previous loading cases, the trends in Figure 8.10 match the trends in the early stages of deformation in Figures 8.5 and 8.8. This simple shear loading case is performed over a smaller strain range than the uniaxial and plane-strain compression cases, and, therefore, the dislocation density evolution does not progress as far. Although the difference between the two dislocation processes reflected by both models decreases to zero in Figures 8.5 and 8.8, the decrease is proceeded by an increase in the Kocks-Mecking example. This increase is reflected in Figure 8.10a. Although it cannot be stated from this example that the difference between the processes will go to zero at some point, it can be said that this case does not differ significantly from the prior two cases.

8.2.5 Discussion

The results obtained from the finite-strain, multiaxial dislocation density-based elasto-plasticity constitutive model developed in this work demonstrate the model's ability to capture the work hardening behaviour of aluminium at large deformations well. This is evidenced by the large-deformation uniaxial loading presented in Figure 8.3b, where the Hariharan-Barlat model matches the finite-strain experimental data sufficiently. However, the constitutive model is limited in its ability to capture cyclical loading; although the aluminium typically demonstrates near-isotropic hardening under cyclical loading conditions, the constitutive model fails to capture the reduced yield stress in the reversed direction as it is not taken into account in the model's formulation that only precipitates contribute to work hardening in the reversed direction. This is discussed in Section

4.4.2 on the Bauschinger effect. Moreover, the precise testing conditions and material parameters are not known; therefore, there is likely to be some mismatch as a result.

A key feature of the proposed constitutive model is demonstrated in Section 8.2.3 on plane-strain compression where the multiaxial stress state computed by the model is presented in Figure 8.7b. The ability to capture multiaxial stress states is demonstrated again in Section 8.2.4, although the extensibilty of the dislocation density evolution equations to shear loading is unclear.

Although plane-strain compression and shear loading experimental data would be required to fully confirm the degree to which the model captures work hardening behaviour in these specific cases, the ability of the model to capture finite-strain, multiaxial hardening is sufficiently supported by comparisons with uniaxial experimental data and comparisons with trends in the literature.

Chapter 9

Conclusion

A preliminary material point-level numerical implementation of a dislocation density-based, finite-strain, rate-dependent elastoplasticity constitutive model has been presented in this work that has extended the use of dislocation density-based plasticity models to a multiaxial, finite-strain framework. Average dislocation density is used as an internal state variable, where the Kocks-Mecking and Hariharan-Barlat models have been used to capture the evolution thereof. The numerical implementation of the constitutive model has been verified against solutions to ordinary differential equations (ODE's) representing analytically simplified test cases that make use of standard numerical ODE solvers. These are referred to as quasi-analytical solutions in this work and comparisons between the numerical model and these solutions were made for uniaxial, symmetric shear, and planar loading conditions. Experimental data from the literature was used to validate the model for monotonic and cyclical uniaxial loading, with the model fitting the former well and capturing many of the features of the latter, albeit with an under-prediction of the magnitude of the stress for the compressive portion of the loading that followed initial extension. The model fitted to the experimental data was also used to examine the behaviour of the model for plane-strain compression, and simple shear loading conditions.

9.1 Key Findings

The dislocation density model material parameters should not be overly sensitive to small errors introduced during the parameter determination process. Investigation showed that the largest change in predicted flow stress caused by varying any combination of parameters by 5% was approximately 10% for a uniaxial test case. It was determined that this was an appropriate sensitivity to the value of the parameters.

Moreover, a brief analysis of the effect of the variation of individual parameters confirmed that the dislocation storage and dislocation annihilation terms influenced the work hardening rate in a manner consistent with their formulation.

Under quasi-static loading conditions, the results from a uniaxial loading case showed agreement with results from the literature. This finding confirms the ability of the model to capture flow stress under finite-strain uniaxial conditions for the alloys used in the experiments to which this work was compared. A prominent feature of the model is its capacity to make reasonable predictions for cases beyond the fitted data. When fitted to uniaxial experimental data, the model could be used to make reasonable predictions for several multiaxial test cases. These predictions were not directly compared to experiments, but suggest the model may be suitable for future investigations which are briefly discussed in the following section.

9.2 Recommendations for Further Work

Comparison to experimental data for a range of multiaxial loading cases would be required to fully validate the model for such use cases. However, two key changes to the formulation of the model would make it more likely to match the behaviour of real-world materials for these significantly more complex stress states:

(i) The model should be recast into a combined isotropic-kinematic hardening framework to better capture unloading and cyclical loading, and

(ii) to more accurately capture the Bauschinger effect during cyclical loading, the dislocation density evolution equation should be extended to account for the additional glide obstacles introduced by precipitates.

Lastly, this model should be implemented in a finite element solver which would allow consideration of the behaviour of a domain instead of a single material point. This would enable a more in-depth validation programme that considers a variety of multiaxial loading cases to be conducted. This would likely require an extensive experimental campaign well beyond the scope of this study. Once complete, this would allow the model to be used predictively in multiaxial settings.

Bibliography

[1] E. Lee and D. Liu, "Finite-strain elastic-plastic theory with application to plane-wave analysis," *Journal of Applied Physics*, vol. 38, pp. 19–27, 1967.

[2] B. D. Coleman and M. E. Gurtin, "Thermodynamics with internal state variables," *The Journal of Chemical Physics*, vol. 47, pp. 597–613, 1967.

[3] J.-L. Chaboche, "A review of some plasticity and viscoplasticity constitutive theories," *International Journal of Plasticity*, vol. 24, pp. 1642–1693, 2008.

[4] M. Baig, J. Owusu-Danquah, A. A. Campbell, and S. F. Duffy, "Inelastic constitutive modeling: Polycrystalline materials," *Materials*, vol. 16, p. 3564, 2023.

[5] G. I. Taylor, "The mechanism of plastic deformation of crystals: Part I - theoretical," *Proceedings of the Royal Society of London. Series A, Containing Papers of a Mathematical and Physical Character*, vol. 145, pp. 362–387, 1934.

[6] H. Mughrabi, "Dislocation wall and cell structures and long-range internal stresses in deformed metal crystals," *Acta Metallurgica*, vol. 31, pp. 1367–1379, 1983.

[7] E. Nes, "Modelling of work hardening and stress saturation in FCC metals," *Progress in Materials Science*, vol. 41, pp. 129–193, 1997.

[8] F. Roters, D. Raabe, and G. Gottstein, "Work hardening in heterogeneous alloysâăťa microstructural approach based on three internal state variables," *Acta Materialia*, vol. 48, pp. 4181–4189, 2000.

[9] K. Marthinsen and E. Nes, "Modelling strain hardening and steady state deformation of al–mg alloys," *Materials Science and Technology*, vol. 17, pp. 376–388, 2001.

[10] M. Goerdeler and G. Gottstein, "A microstructural work hardening model based on three internal state variables," *Materials Science and Engineering: A*, vol. 309, pp. 377–381, 2001.

[11] M. Goerdeler, M. Crumbach, M. Schneider, G. Gottstein, L. Neumann, H. Aretz, and R. Kopp, "Dislocation density based modeling of work hardening in the context of integrative modeling of aluminum processing," *Materials Science and Engineering: A*, vol. 387-389, pp. 266–271, 2004, 13th International Conference on the Strength of Materials.

[12] B. Holmedal, K. Marthinsen, and E. Nes, "A unified microstructural metal plasticity model applied in testing, processing, and forming of aluminium alloys," *International Journal of Materials Research*, vol. 96, pp. 532–545, 2005.

[13] A. Hunter and D. L. Preston, "Analytic model of dislocation density evolution in FCC polycrystals accounting for dislocation generation, storage, and dynamic recovery mechanisms," *International Journal of Plasticity*, vol. 151, p. 103 178, 2022.

[14] W. Poole, J. Embury, and D. Lloyd, "Work hardening in aluminium alloys," *Fundamentals of Aluminium Metallurgy*, Elsevier, 2011, pp. 307–344.

[15] U. Kocks and H. Mecking, "Physics and phenomenology of strain hardening: The FCC case," *Progress in Materials Science*, vol. 48, pp. 171–273, 2003.

[16] U. Kocks, "A statistical theory of flow stress and work-hardening," *Philosophical Magazine*, vol. 13, pp. 541–566, 1966.

[17] U. Kocks, A. Argon, and M. Ashby, "Thermodynamics and kinetics of slip," *Progress in Materials Science*, vol. 19, 1975.

[18] H. Mecking and U. Kocks, "Kinetics of flow and strain-hardening," *Acta Metallurgica*, vol. 29, pp. 1865–1875, 1981.

[19] Y. Estrin and H. Mecking, "A unified phenomenological description of work hardening and creep based on one-parameter models," *Acta Metallurgica*, vol. 32, pp. 57–70, 1984.

[20] U. Kocks, "Constitutive behavior based on crystal plasticity," *Unified Constitutive Equations for Creep and Plasticity*, Springer, 1987, pp. 1–88.

[21] O. Bouaziz, "Revisited storage and dynamic recovery of dislocation density evolution law: Toward a generalized Kocks-Mecking model of strain-hardening," *Advanced Engineering Materials*, vol. 14, pp. 759–761, 2012.

[22] R. A. Barrett, P. E. OâĂŹDonoghue, and S. B. Leen, "A dislocation-based model for high temperature cyclic viscoplasticity of 9-12Cr steels," *Computational Materials Science*, vol. 92, pp. 286–297, 2014.

[23] H. Al-Abedy, I. Jones, and W. Sun, "Small punch creep property evaluation by finite element of Kocks-Mecking-Estrin model for P91 at elevated temperature," *Theoretical and Applied Fracture Mechanics*, vol. 98, pp. 244–254, 2018.

[24] G. Fribourg, Y. Bréchet, A. Deschamps, and A. Simar, "Microstructure-based modelling of isotropic and kinematic strain hardening in a precipitation-hardened aluminium alloy," *Acta Materialia*, vol. 59, pp. 3621–3635, 2011.

[25] O. Bouaziz, D. Barbier, J. Embury, and G. Badinier, "An extension of the kocks–mecking model of work hardening to include kinematic hardening and its application to solutes in ferrite," *Philosophical Magazine*, vol. 93, pp. 247–255, 2013.

[26] R. Guo and J. Wu, "Dislocation density based model for al-cu-mg alloy during quenching with considering the quench-induced precipitates," *Journal of Alloys and Compounds*, vol. 741, pp. 432–441, 2018.

[27] K. Hariharan and F. Barlat, "Modified Kocks-Mecking-Estrin model to account nonlinear strain hardening," *Metallurgical and Materials Transactions A*, vol. 50, pp. 513–517, 2019.

[28] F. Barlat, M. Glazov, J. Brem, and D. Lege, "A simple model for dislocation behavior, strain and strain rate hardening evolution in deforming aluminum alloys," *International Journal of Plasticity*, vol. 18, pp. 919–939, 2002.

[29] M. E. Gurtin, E. Fried, and L. Anand, *The Mechanics and Thermodynamics of Continua*. Cambridge University Press, 2010.

[30] S. Govindjee and L. Anand, *Continuum Mechanics of Solids*. Oxford Graduate Texts, 2020.

[31] W. Han and B. D. Reddy, *Plasticity: Mathematical Theory and Numerical Analysis*. Springer Science & Business Media, 2012, vol. 9.

[32] K. Hutter and K. Jöhnk, *Continuum Methods of Physical Modeling: Continuum Mechanics, Dimensional Analysis, Turbulence*. Springer Science & Business Media, 2013.

[33] G. A. Holzapfel, *Nonlinear Solid Mechanics: A Continuum Approach for Engineering Science*. Kluwer Academic Publishers Dordrecht, 2002.

[34] D. Hull and D. J. Bacon, *Introduction to Dislocations*. Elsevier, 2011, vol. 37.

[35] P. O. Kettunen and V.-T. Kuokkala, *Plastic deformation and strain hardening*. Trans Tech Switzerland, 2003, vol. 16.

[36] D. Kuhlmann-Wilsdorf, "Theory of work hardening 1934-1948," *Metallurgical Transactions A*, vol. 16, pp. 2091–2108, 1985.

[37] M. F. Horstemeyer and D. J. Bammann, "Historical review of internal state variable theory for inelasticity," *International Journal of Plasticity*, vol. 26, pp. 1310–1334, 2010.

[38] J. Diehl, "Zugverformung von kupfer-einkristallen: I. Verfestigungskurven und oberflächenerscheinungen," *International Journal of Materials Research*, vol. 47, pp. 331–343, 1956.

[39] A. D. Rollett and U. Kocks, "A review of the stages of work hardening," *Solid State Phenomena*, vol. 35, pp. 1–18, 1993.

[40] G. Schoeck and A. Seeger, "Report of the conference on âăijdefects in solidsâăi," *Physical Society, London*, p. 340, 1955.

[41] P. Haasen, "Plastic deformation of nickel single crystals at low temperatures," *Philosophical Magazine*, vol. 3, pp. 384–418, 1958.

[42] A. A. Kohnert and L. Capolungo, "The kinetics of static recovery by dislocation climb," *npj Computational Materials*, vol. 8, p. 104, 2022.

[43] Z. Basinski, "Thermally activated glide in face-centred cubic metals and its application to the theory of strain hardening," *Philosophical Magazine*, vol. 4, pp. 393–432, 1959.

[44] Z. S. Basinski and S. J. Basinski, "Dislocation distributions in deformed copper single crystals," *The Philosophical Magazine: A Journal of Theoretical Experimental and Applied Physics*, vol. 9, pp. 51–80, 1964.

[45] D. Kuhlmann-Wilsdorf, "A new theory of work hardening in crystals," *Trans. Met. Soc. AIME*, vol. 218, p. 962, 1962.

[46] J. Gil Sevillano, P. van Houtte, and E. Aernoudt, "Large strain work hardening and textures," *Progress in Materials Science*, vol. 25, pp. 69–134, 1980.

[47] Z. Jasieński and A. Piakowski, "Shear bands formation in copper single crystals during plane-strain compression," *Strength of Metals and Alloys (ICSMA 8)*, Elsevier, 1989, pp. 367–372.

[48] N. Koneva, D. Lychagin, L. Teplyakova, and E. Kozlov, "Parameters of dislocation structures and factors determining flow stress at stages III and IV," *Strength of Metals and Alloys (ICSMA 8)*, Elsevier, 1989, pp. 385–390.

[49] P. Haasen, "Modelling stage IV work hardening of metals," *Strength of Metals and Alloys (ICSMA 8)*, P. Kettunen, T. Lepistö, and M. Lehtonen, Eds., Oxford: Pergamon, 1989, pp. 343–348.

[50] A. Argon and P. Haasen, "A new mechanism of work hardening in the late stages of large strain plastic flow in F.C.C. and diamond cubic crystals," *Acta Metallurgica et Materialia*, vol. 41, pp. 3289–3306, 1993.

[51] P. Follansbee and U. Kocks, "A constitutive description of the deformation of copper based on the use of the mechanical threshold stress as an internal state variable," *Acta Metallurgica*, vol. 36, pp. 81–93, 1988.

[52] E. Nes and K. Marthinsen, "Modeling the evolution in microstructure and properties during plastic deformation of FCC-metals and alloys–an approach towards a unified model," *Materials Science and Engineering: A*, vol. 322, pp. 176–193, 2002.

[53] Y. Estrin, L. Tóth, A. Molinari, and Y. Bréchet, "A dislocation-based model for all hardening stages in large strain deformation," *Acta Materialia*, vol. 46, pp. 5509–5522, 1998.

[54] A. Soni and A. Alankar, "Analyses of constitutive behavior of as-cast aluminum alloys AA3104, AA5182, and AA6111 during direct chill casting using physically based models," *Journal of Engineering Materials and Technology*, vol. 141, 2019.

[55] E. Galindo-Nava, J. Sietsma, and P. Rivera-Díaz-del Castillo, "Dislocation annihilation in plastic deformation: II. Kocks-Mecking analysis," *Acta Materialia*, vol. 60, pp. 2615–2624, 2012.

[56] B. Choudhary and J. Christopher, "Tensile work hardening behavior of thin-section plate and thick-section tubeplate forging of 9cr-1mo steel in the framework of one-internal-variable Kocks-Mecking approach," *Metallurgical and Materials Transactions A*, vol. 44, pp. 4968–4978, 2013.

[57] N. Tsuchida, Y. Tomota, H. Moriya, O. Umezawa, and K. Nagai, "Application of the Kocks-Mecking model to tensile deformation of an austenitic 25Cr-19Ni steel," *Acta Materialia*, vol. 49, pp. 3029–3038, 2001.

[58] A. Simar, Y. Bréchet, B. De Meester, A. Denquin, and T. Pardoen, "Sequential modeling of local precipitation, strength and strain hardening in friction stir welds of an aluminum alloy 6005A-T6," *Acta Materialia*, vol. 55, pp. 6133–6143, 2007.

[59] L. Cheng, W. Poole, J. Embury, and D. Lloyd, "The influence of precipitation on the work-hardening behavior of the aluminum alloys AA6111 and AA7030," *Metallurgical and Materials Transactions A*, vol. 34, pp. 2473–2481, 2003.

[60] W. Poole and D. Lloyd, "Modelling the stress-strain behaviour for aluminum alloy AA6111," *Materials Forum*, vol. 28, 2004, pp. 939–944.

[61] O. Bouaziz, H. S. Kim, J. Lee, and Y. Estrin, "Bauschinger effect or kinematic hardening: Bridging microstructure and continuum mechanics," *Metals and Materials International*, vol. 29, pp. 280–292, 2023.

[62] J. Schröder, T. Wick, S. Reese, P. Wriggers, R. Müller, S. Kollmannsberger, M. Kästner, A. Schwarz, M. Igelbüscher, N. Viebahn, *et al.*, "A selection of benchmark problems in solid mechanics and applied mathematics," *Archives of Computational Methods in Engineering*, vol. 28, pp. 713–751, 2021.

[63] J. E. Marsden and T. J. Hughes, *Mathematical Foundations of Elasticity*. Courier Corporation, 1994.

[64] D. J. Luscher, M. A. Buechler, D. J. Walters, C. Bolme, and K. J. Ramos, "On computing the evolution of temperature for materials under dynamic loading," *International Journal of Plasticity*, vol. 111, pp. 188–210, 2018.

[65] S. Tamura, S. Sumikawa, T. Uemori, H. Hamasaki, and F. Yoshida, "Experimental observation of elasto-plasticity behavior of type 5000 and 6000 aluminum alloy sheets," *Materials Transactions*, vol. 52, pp. 868–875, 2011.

[66] P. D. O'Connor and A. T. Kleyner, "Statistical design of experiments and analysis of variance." John Wiley & Sons, 2012, ch. Practical Reliability Engineering (5th Edition), pp. 284–302.

[67] R. N. Kacker, E. S. Lagergren, and J. J. Filliben, "Taguchiâăźs orthogonal arrays are classical designs of experiments," *Journal of research of the National Institute of Standards and Technology*, vol. 96, p. 577, 1991.

[68] W. Ramberg and J. A. Miller, "Stress-strain relation in shear from twisting test of annulus," *Journal of Research of the National Bureau of Standards*, vol. 50, pp. 125–130, 1953.

[69] B. Jia, A. Rusinek, X. Xiao, and P. Wood, "Simple shear behavior of 2024-t351 aluminum alloy over a wide range of strain rates and temperatures: Experiments and constitutive modeling," *International Journal of Impact Engineering*, vol. 156, 2021.

[70] F. Nabarro, Z. Basinski, and D. Holt, "The plasticity of single crystals," *Advances in Physics*, vol. 13, pp. 193–323, Apr. 1964.

[71] D. Kuhlmann-Wilsdorf, "Theory of plastic deformation:-properties of low energy dislocation structures," *Materials Science and Engineering: A*, vol. 113, pp. 1–41, 1989.

Appendix A

The Laws of Thermodynamics

A body is constrained by two thermodynamic laws, namely

i) the balance of energy, and

ii) the imbalance of entropy.

A more detailed discussion on thermodynamics can be found in [29]–[31].

A.1 The First Law of Thermodynamics: Balance of Energy

The first law of thermodynamics states that the rate of change of the internal energy and kinetic energy within a region must be equal to the sum of the rate of heat transferred to the region and the external mechanical power expended on the region [29]–[31]. With the internal energy of spatial region $\mathcal{B}_t$ represented as $\mathcal{U}(\mathcal{B}_t)$, kinetic energy as $\mathcal{K}(\mathcal{B}_t)$, heat flow as $\mathcal{Q}(\mathcal{B}_t)$, and external power as $\mathcal{W}_{\text{ext}}(\mathcal{B}_t)$, the energy balance can be shown in mathematical form:

$$\frac{\partial}{\partial t}\Big(\mathcal{U}(\mathcal{B}_t) + \mathcal{K}(\mathcal{B}_t)\Big) = \mathcal{Q}(\mathcal{B}_t) + \mathcal{W}_{\text{ext}}(\mathcal{B}_t). \tag{A.1}$$

The four quantities in Equation (A.1) are defined as follows:

i) The net internal energy $\mathcal{U}(\mathcal{B}_t)$ is

$$\mathcal{U}(\mathcal{B}_t) := \int_{\mathcal{B}_t} \rho_m u_{\text{int}} \, \mathrm{d}v \tag{A.2}$$

where the scalar field $u_{\text{int}}(\boldsymbol{x}, t)$ represents the internal energy measured per unit mass, i.e. the specific internal energy, and ρ_m represents the specific mass density.

ii) The kinetic energy $\mathcal{K}(\mathcal{B}_t)$ is

$$\mathcal{K}(\mathcal{B}_t) := \int_{\mathcal{B}_t} \frac{1}{2}\rho_m |\dot{\boldsymbol{u}}|^2 \, \mathrm{d}v. \tag{A.3}$$

iii) The rate of heat flow into $\mathcal{B}_t$ $\mathcal{Q}(\mathcal{B}_t)$, is

$$\mathcal{Q}(\mathcal{B}_t) = -\int_{\partial\mathcal{B}_t} \boldsymbol{q}\cdot\boldsymbol{n} \, \mathrm{d}a + \int_{\mathcal{B}_t} r \, \mathrm{d}v, \tag{A.4}$$

where the first term describes the rate at which heat is transferred into $\mathcal{B}_t$ across $\partial\mathcal{B}_t$, and the second term describes the rate at which heat is transferred into $\mathcal{B}_t$ by a heat source.

iv) The external power is

$$\mathcal{W}_{\text{ext}}(\mathcal{B}_t) = \int_{\partial\mathcal{B}_t} \boldsymbol{\sigma}\boldsymbol{n}\cdot\dot{\boldsymbol{u}} \, \mathrm{d}a + \int_{\mathcal{B}_t} \boldsymbol{b}\cdot\dot{\boldsymbol{u}} \, \mathrm{d}v, \tag{A.5}$$

where $\boldsymbol{b}$ are the external forces acting on $\mathcal{B}_t$ by unit volume.

By substituting these four definitions into the energy balance in Equation (A.1), the first law of thermodynamics can be expressed in the form

$$\frac{\partial}{\partial t}\left(\int_{\mathcal{B}_t} \rho_m u_{\text{int}} + \frac{1}{2}\rho_m |\dot{\boldsymbol{u}}|^2 \, \mathrm{d}v \right) = -\int_{\partial\mathcal{B}_t} \boldsymbol{q}\cdot\boldsymbol{n} \, \mathrm{d}a + \int_{\mathcal{B}_t} r \, \mathrm{d}v + \int_{\partial\mathcal{B}_t} \boldsymbol{\sigma}\boldsymbol{n}\cdot\dot{\boldsymbol{u}} \, \mathrm{d}a + \int_{\mathcal{B}_t} \boldsymbol{b}\cdot\dot{\boldsymbol{u}} \, \mathrm{d}v \tag{A.6}$$

Note that $J\mathrm{d}V = \mathrm{d}v$, $J\rho_m = \rho_R$, where ρ_R is the density in the material domain and is, therefore, independent of time,

$$\frac{\partial}{\partial t}\left(\int_{\mathcal{B}_t} \rho_m u_{\text{int}} + \frac{1}{2}\rho_m |\dot{\boldsymbol{u}}|^2 \, \mathrm{d}v \right) = \int_{\mathcal{B}} \rho_R \dot{u}_{\text{int}} + \rho_R \dot{\boldsymbol{u}}\cdot\ddot{\boldsymbol{u}} \, \mathrm{d}V = \int_{\mathcal{B}_t} \rho_m \dot{u}_{\text{int}} + \rho_m \dot{\boldsymbol{u}}\cdot\ddot{\boldsymbol{u}} \, \mathrm{d}v. \tag{A.7}$$

Applying the divergence theorem to Equation (A.6) while noting the symmetry of the Cauchy stress gives

$$\int_{\mathcal{B}_t} \rho_m \dot{\varepsilon} + \operatorname{div}(\mathbf{q}) - r - \boldsymbol{\sigma} : \boldsymbol{D} - [\operatorname{div}(\boldsymbol{\sigma}) + \boldsymbol{b} - \rho_m \ddot{\boldsymbol{u}}] \cdot \dot{\boldsymbol{u}} \, \mathrm{d}v = 0. \tag{A.8}$$

From the balance of linear momentum, $\operatorname{div}(\boldsymbol{\sigma}) + \boldsymbol{b} - \rho_m \ddot{\boldsymbol{u}} = 0$ [29]–[31]. Using the localization theorem and the point-wise balance of momentum [29]–[31], the local spatial form of the energy balance equation is obtained:

$$\rho_m \dot{u}_{\text{int}} = \boldsymbol{\sigma} : \boldsymbol{D} - \operatorname{div}(\mathbf{q}) + r. \tag{A.9}$$

A.2 The Second Law of Thermodynamics: Imbalance of Entropy

The second law of thermodynamics states that the total production of entropy within a body is always positive [29]–[31]. Entropy may be produced within the domain, and may be transferred across and out of it into the external environment. The net entropy of a spatial region $\mathcal{B}_t$ is

$$\mathcal{S}(\mathcal{B}_t) = \int_{\mathcal{B}_t} \rho_m \, \eta \, \mathrm{d}v, \tag{A.10}$$

where $\eta\,(\boldsymbol{x}, t)$ is the specific entropy. The flow of entropy into the region $\mathcal{P}_t$ is

$$\mathcal{J}(\mathcal{B}_t) = -\int_{\partial\mathcal{B}_t} \boldsymbol{j} \cdot \boldsymbol{n} \, \mathrm{d}a + \int_{\mathcal{B}_t} j \, \mathrm{d}v, \tag{A.11}$$

where $\boldsymbol{j}$ is the entropy flux, and j is the entropy supply. A tenet of thermodynamics is that entropy tends to increase, and so it is required that the rate of change of entropy of $\mathcal{B}_t$ is greater than or equal to the flow of entropy into $\mathcal{B}_t$, i.e.

$$\frac{\partial}{\partial t}\Big(\mathcal{S}(\mathcal{B}_t)\Big) \geq \mathcal{J}(\mathcal{B}_t). \tag{A.12}$$

Thus, the spatial formulation of entropy imbalance is obtained

$$\frac{\partial}{\partial t}\bigg(\int_{\mathcal{B}_t} \rho_m \, \eta \, \mathrm{d}v\bigg) \geq -\int_{\partial\mathcal{B}_t} \boldsymbol{j} \cdot \boldsymbol{n} \, \mathrm{d}a + \int_{\mathcal{B}_t} j \, \mathrm{d}v. \tag{A.13}$$

A.2.1 The Clausius-Duhem Inequality

A tacit assumption in thermodynamic theory is that there is some scalar field representing the absolute temperature,

$$\vartheta > 0, \tag{A.14}$$

which takes positive values and only vanishes at absolute zero such that

$$\boldsymbol{j} = \frac{\boldsymbol{q}}{\vartheta}, \quad j = \frac{q}{\vartheta}. \tag{A.15}$$

The entropy supply is defined as the energy supply divided by the absolute temperature, and constrains entropy and heat flow to the same direction. Heat flows from high temperatures to low temperatures; this fact combined with Equations (A.13) and (A.15) form the Clausius-Duhem inequality

$$\frac{\partial}{\partial t}\bigg(\int_{\mathcal{B}_t} \rho_m \, \eta \, \mathrm{d}v\bigg) \geq -\int_{\partial\mathcal{B}_t} \frac{\boldsymbol{q}}{\vartheta} \cdot \boldsymbol{n} \, \mathrm{d}a + \int_{\mathcal{B}_t} \frac{q}{\vartheta} \, \mathrm{d}v. \tag{A.16}$$

Note that

$$\frac{\partial}{\partial t}\left(\int_{\mathcal{B}_t} \rho_m \, \eta \, \mathrm{d}v \right) = \int_{\mathcal{B}_t} \rho_m \dot{\eta} \, \mathrm{d}v, \tag{A.17}$$

and, from the divergence theorem,

$$-\int_{\partial\mathcal{B}_t} \frac{\boldsymbol{q}}{\vartheta} \cdot \boldsymbol{n} \, \mathrm{d}a + \int_{\mathcal{B}_t} \frac{q}{\vartheta} \, \mathrm{d}v = -\int_{\partial\mathcal{B}_t} \operatorname{div}\left(\frac{\boldsymbol{q}}{\vartheta}\right) \, \mathrm{d}v + \int_{\mathcal{B}_t} \frac{q}{\vartheta} \, \mathrm{d}v. \tag{A.18}$$

The localization theorem is applied to arrive at the local spatial form of the second law of thermodynamics,

$$\rho_m \dot{\eta} \geq -\operatorname{div}\left(\frac{\boldsymbol{q}}{\vartheta}\right) + \frac{q}{\vartheta}. \tag{A.19}$$

A.3 Helmholtz Free Energy

The thermodynamic potential that describes the work obtainable from a closed, isothermal thermodynamic system is termed the Helmholtz free energy, which is minimized at equilibrium. Free energy is measured as the difference between the internal energy of the system and the energy supply,

$$\mathcal{F}(\mathcal{B}_t) := \mathcal{U}(\mathcal{B}_t) - \mathcal{T}(\mathcal{B}_t)\mathcal{S}(\mathcal{B}_t), \tag{A.20}$$

where $\mathcal{T}(\mathcal{B}_t)$ is the absolute temperature. The specific, local Helmholtz free energy of a spatial region is expressed as

$$\Psi := u_{\mathrm{int}} - \vartheta\eta. \tag{A.21}$$

Appendix B

Review of Work Hardening Phenomena in Face-Centred Cubic Metals

B.1 Similitude

The principle of similitude was first proposed as a feature of Kuhlmann-Wilsdorf's mesh theory [45], which is discussed as a theory of work hardening in Section B.2. A brief description of this principle is provided in this section, but its relevance is left to be seen in Section B.2. Broadly, the principle concerns the relation between the geometry of a dislocation network and the stress required to overcome the resistance to dislocation motion. It is supposed that the length l of a free section in a dislocation in a network is inversely proportional to the instantaneous glide resistance τ such that the relation

$$l \propto \frac{l}{\tau} \tag{B.1}$$

holds. The notable outcome of this definition of similitude is a constant strain-hardening rate. Although this principle is used to describe the proportionality between the mean free path of dislocations and their spacing, not all microstructural parameters scale accordingly [15]. Cell wall thickness is an example of microstructural parameter that does not conform to this proportionality.

B.2 Work Hardening Phenomena

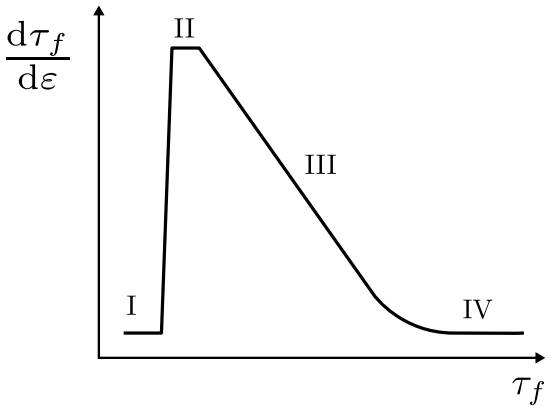

Figure B.1: Four stages are evident when the hardening rate, which is calculated as a change in flow stress over change in strain, is examined against against flow stress. Stage I and Stage II are classified by their near-constant linear hardening rates, Stage III is delineated by a linearly decreasing hardening rate, and Stage IV is marked by a nonlinear transition to near-constant hardening.

Rollett et al. [39] demonstrate the delineation of the work hardening stages with reference to the rate of hardening in a diagram like that shown in Figure B.1. Although work hardening stages are not characterised solely by their hardening rate, diagrams like Figure B.1 provide a means of identifying the stages present without the need to observe the microstructural phenomena throughout loading.

Stage I

Stage I is characterised by *easy glide*, which refers to single crystal deformation on a single slip system that accumulates significant strain with relatively low strain hardening. This description is only relevant to the deformation of single crystals in certain crystallographic orientations, but it supposes that the observed low work hardening rate is a consequence of a dislocation debris accumulation mechanism. This mechanism features in most Stage I theories, in which the glide resistance, or yield strength, is attributed to dislocation motion being impeded by the influence of opposing dislocations on a parallel plane. In forest dislocation theory [43], [44], Basinski proposes that the yield strength of Stage I is strongly attributed to the accumulation of secondary dislocations impeding the motion of mobile dislocations in the crystal structure. The weakness of this theory and other prominent Stage I theories is that hardening as a result of interactions between primary dislocations is unexplained. The transition from Stage I to Stage II cannot be well attributed to a particular mechanism, as the transition is sensitive to stress raisers from surface defects, material purity, and the wear of the material [70].

Stage II

Stage II is characterised by *athermal linear hardening* controlled by an increase in latent hardening. The hardening rate in Stage II is similarly orientation dependent, but temperature independent. Mecking et al. [18] determined that Taylor's equation (3.2) holds well over the Stage II range, even though the equation only considers the stress required to overcome the impediment to dislocation movement caused by other dislocations, and not the stresses required to overcome plastic resistance due to solution hardening or grain size effects.

Forest theory is extended to Stage II under the assumption that the dislocation arrangement remains similar throughout Stage II, as only its dimensions change inversely with the applied shear stress, in accordance with the principle of similitude. Similarly, in mesh theory [45] it is proposed that the dislocation network structure will assume a geometry that minimizes the stored energy per unit length of dislocation line such that a low energy dislocation structure (LEDS) is achieved, and that once this LEDS is formed, similitude is observed. It is assumed that the yield stress is determined by the lattice friction and the self-stress of a bowing dislocation segment [71].

Kocks provides a statistical theory [16] of slip and strain hardening, which differs from other Stage II theories as slip is distinctly separated from strain hardening. Briefly, Kocks assumes that there is variation in obstacle strength and distribution, and that the probability of obstacle penetration is related to the ratio of the applied shear stress to the effective average glide resistance on the glide plane. This addresses slip. The stress ratio is further manipulated and combined with a hardening and a yield parameter to arrive at an equation which encompasses strain hardening. This formulation extends the study of work hardening from pure strain hardening to hardening as a result of solutes, dispersoids, and precipitates.

Appendix C

Derivations Related to the Development of a Finite-Strain Elastoplasticity Constitutive Model

Equation (6.50) requires the computation of the derivative of the elastic Kirchhoff stress with respect to the plastic deformation gradient. Using the relationship between the elastic Kirchhoff stress and the elastic second Piola-Kirchhoff stress given by Equation (2.71), the derivative of the Kirchhoff stress with respect to the plastic deformation is derived as follows:

$$\frac{\partial \boldsymbol{\tau}}{\partial \boldsymbol{F}_p} = \frac{\partial}{\partial \boldsymbol{F}_p}\left(\boldsymbol{F}\boldsymbol{F}_p^{-1}\boldsymbol{S}_e\boldsymbol{F}_p^{-T}\boldsymbol{F}^T\right), \tag{C.1}$$

using the product rule and noting that $\boldsymbol{F}$ is fixed for a given Newton-Raphson iteration,

$$\frac{\partial \boldsymbol{\tau}}{\partial \boldsymbol{F}_p} = \boldsymbol{F}\left[\boldsymbol{F}_p^{-1}\frac{\partial \boldsymbol{S}_e}{\partial \boldsymbol{F}_p}\boldsymbol{F}_p^{-T} + \frac{\partial \boldsymbol{F}_p^{-1}}{\partial \boldsymbol{F}_p}\boldsymbol{S}_e\boldsymbol{F}_p^{-T} + \boldsymbol{F}_p^{-1}\boldsymbol{S}_e\frac{\partial \boldsymbol{F}_p^{-T}}{\partial \boldsymbol{F}_p}\right]\boldsymbol{F}^T. \tag{C.2}$$

Via the chain rule and applying the known identities for the derivatives of inverses given by Equation (2.11), Equation (C.2) becomes

$$\frac{\partial \boldsymbol{\tau}}{\partial \boldsymbol{F}_p} = \boldsymbol{F}\left[\boldsymbol{F}_p^{-1}\frac{\partial \boldsymbol{S}_e}{\partial \boldsymbol{C}_e}\frac{\partial \boldsymbol{C}_e}{\partial \boldsymbol{F}_p}\boldsymbol{F}_p^{-T} + \left[-\boldsymbol{F}_p^{-1}\odot\boldsymbol{F}_p^{-1}\right]\boldsymbol{S}_e\boldsymbol{F}_p^{-T} + \boldsymbol{F}_p^{-1}\boldsymbol{S}_e\left[-\boldsymbol{F}_p^{-T}\odot\boldsymbol{F}_p^{-T}\right]\right]\boldsymbol{F}^T, \tag{C.3}$$

$$= \boldsymbol{F}_e\frac{\partial \boldsymbol{S}_e}{\partial \boldsymbol{C}_e}\frac{\partial \boldsymbol{C}_e}{\partial \boldsymbol{F}_p}\boldsymbol{F}_e - \left[\boldsymbol{F}_e\odot\boldsymbol{F}^{-1}\right]\boldsymbol{\tau} - \boldsymbol{\tau}\left[\boldsymbol{F}^{-T}\odot\boldsymbol{F}_e^T\right]. \tag{C.4}$$

At this juncture, it is convenient to introduce the material elasticity tensor as

$$\mathbb{C}_e = 2\frac{\partial \boldsymbol{S}_e}{\partial \boldsymbol{C}_e}, \tag{C.5}$$

which is related to the spatial elasticity tensor via the transformation

$$\mathbb{c}_e = \left[\boldsymbol{F}_e \odot \boldsymbol{F}_e^T\right] : \mathbb{C} : \left[\boldsymbol{F}_e^T \odot \boldsymbol{F}_e\right]. \tag{C.6}$$

The derivative of the elastic right Cauchy-Green tensor with respect to the plastic deformation gradient is also required. The derivation proceeds as such:

$$\frac{\partial \boldsymbol{C}_e}{\partial \boldsymbol{F}_p} = \frac{\partial}{\partial \boldsymbol{F}_p}\left(\boldsymbol{F}_e^T \boldsymbol{F}_e\right), \tag{C.7}$$

via the product rule and noting that $\dfrac{\partial \boldsymbol{F}_e}{\partial \boldsymbol{F}_p} = -\boldsymbol{F}_e \odot \boldsymbol{F}_p^{-1}$,

$$\begin{aligned}
\frac{\partial \boldsymbol{C}_e}{\partial \boldsymbol{F}_p} &= -\left[\boldsymbol{F}_e^{-T} \odot \boldsymbol{F}_e^{-T}\right] \boldsymbol{F}_e - \boldsymbol{F}_e^T \left[\boldsymbol{F}_e \odot \boldsymbol{F}_p^{-1}\right], && \text{(C.8)}\\
&= -\boldsymbol{F}_e^{-T} \boldsymbol{F}_e \boldsymbol{F}_e^{-T} - \boldsymbol{F}_e \boldsymbol{F}_e^T \boldsymbol{F}_p^{-1}, && \text{(C.9)}\\
&= -2\,\mathrm{sym}\left(\boldsymbol{F}_e \boldsymbol{F}_e^T \boldsymbol{F}_p^{-1}\right), && \text{(C.10)}\\
&= -2\,\mathrm{sym}\left(\boldsymbol{F}_e \boldsymbol{F}_e^T \boldsymbol{F}^{-1} \boldsymbol{F}_e\right), && \text{(C.11)}\\
&= -\boldsymbol{F}_e^T\,\mathrm{sym}\left(\boldsymbol{F}_e \odot \boldsymbol{F}^{-1}\right) \boldsymbol{F}_e. && \text{(C.12)}
\end{aligned}$$

Thus, from Equations (C.5), (C.6), and (C.12), Equation (C.4) becomes

$$\begin{aligned}
\frac{\partial \boldsymbol{\tau}}{\partial \boldsymbol{F}_p} &= -\mathbb{c}_e\,\mathrm{sym}\left(\boldsymbol{F}_e \odot \boldsymbol{F}^{-1}\right) - \left[\boldsymbol{F}_e \odot \boldsymbol{F}^{-1}\right] \boldsymbol{\tau} - \boldsymbol{\tau} \left[\boldsymbol{F}^{-T} \odot \boldsymbol{F}_e^T\right], && \text{(C.13)}\\
&= -\left[\mathbb{c}_e + \boldsymbol{I} \odot \boldsymbol{\tau} + \boldsymbol{\tau} \odot^T \boldsymbol{I}\right] \left[\boldsymbol{F}_e \odot \boldsymbol{F}^{-1}\right]. && \text{(C.14)}
\end{aligned}$$

It is convenient to define the special tensor,

$$\mathbb{c}_{e\boldsymbol{\tau}} = \left[\mathbb{c}_e + \boldsymbol{I} \odot \boldsymbol{\tau} + \boldsymbol{\tau} \odot^T \boldsymbol{I}\right], \tag{C.15}$$

such that the derivative becomes

$$\frac{\partial \boldsymbol{\tau}}{\partial \boldsymbol{F}_p} = -\mathbb{c}_{e\boldsymbol{\tau}} \left[\boldsymbol{F}_e \odot \boldsymbol{F}^{-1}\right]. \tag{C.16}$$